

Aeronautical Research and Development

2

"Georgi Benkovski"
Bulgarian Air Force Academy

Aeronautical Research and Development

2

"Georgi Benkovski"
Bulgarian Air Force Academy

Aeronautical Research and Development Volume 2, 2023

AERONAUTICAL RESEARCH AND DEVELOPMENT
Volume 2 ▪ Dolna Mitropolia ▪ 2023

"Georgi Benkovski" Bulgarian Air Force Academy

EDITORIAL BOARD

Assoc. Prof. Dr. Asen Angelov Marinov – Editor in Chief

Assoc. Prof. Dr. Martin Milenov Kambushev, Assoc. Prof. Dr. Georgi Valentinov Stanchev, Assoc. Prof. Dr. Milen Atanasov Atanasov, Assoc. Prof. Dr. Lubomir Vasilev Mitov, Assoc. Prof. Dr. Stoyko Ognyanov Stoykov, Prof. Dr. Manush Petkov Hristov, Assoc. Prof. Dr. Toshko Marinov Marinov.

Address

AERONAUTICAL RESEARCH AND DEVELOPMENT

Dolna Mitropolia, 5855

"St. St. Cyril and Methodius" №1, St.

asen_aerodynamics@abv.bg

Language Editor

Yavor Varbanov

"Georgi Benkovski"

Bulgarian Air Force Academy, 2023

Aeronautical Research and Development

2

Dolna Mitropolia, 2023

Contents

Nikolay Kanchev	5
Numerical method for optimal design of the skin stiffeners configuration in a fixed wing structural layout	
Milen Simeonov	14
Discoveries of New Asteroids in The International Astronomical Search Collaboration Science Program	
Radostina Calovska	24
Synthesizing and investigating the performance of Intelligent fuzzy logic controller for mechatronic system control	
Milen Atanasov, Kolyo Kolev, Danyo Lalov	28
Computer Modeling Investigation of the Penetration of an Aircraft Munition (Bomb) Depending on Target Structure	
Milen Atanasov, Kolyo Kolev, Danyo Lalov	33
Calculation of the Deformation of the Fairing of an Aviation Munition (Bomb), When Penetrating a Target With a Multi-Layer Structure	
Stefan Biliderov, Radoslav Chalakov	37
Analysis of the possibilities for the applicability of different types of unmanned aerial vehicles in the crisis management process - building a functional framework for the application of different unmanned aerial vehicles	
Assen Angelov Marinov	46
Hohmann Orbit Transfer Analysis	
Assen Angelov Marinov	52
Hohmann transfer in polar orbits	
Konstantin Metodiev	59
Tracking a Low Earth Orbit Satellite	
Nikolay Kanchev	68
Fixed wing topology optimization: a numerical procedure for computational design model generation	
Radoslav Chalakov, Stefan Biliderov	77
Analysis of possibilities for applicability of different types of unmanned aerial vehicles in the crisis management process - the signs and criteria for classifying of crises	

Numerical method for optimal design of the skin stiffeners configuration in a fixed wing structural layout

Nikolay Kanchev

Bulgarian Air Force Academy, Aviation Faculty, Dolna Mitropolia, Bulgaria, nikolaikanchev@yahoo.com

Abstract: The skin of the fixed wing aircraft is generally made up of panels supported by load-bearing components. The number and location of those elements affect not just the fixed wing's mass, stiffness and stability, but also the aerodynamics of its surface in flight. The paper proposes a numerical method for optimizing the configuration of the supporting structural components while constraining the maximum permitted deformation for monolithic or dismountable skin panels and aiming for the lowest possible mass of the load-bearing structure. The method is illustrated by solving a numerical problem for the optimal design of the load-bearing components configuration supporting the skin panels of the fixed wing for a medium-altitude long endurance ISTAR UAV.

Keywords: *fixed wing, skin stiffeners, structural layout optimization, UAV design.*

1. Introduction

The airframe is made up of several structural components that resist, distribute, and transmit external aerodynamic and inertial loads. The skin, for example, defines the aerodynamic shape of the surface and contributes to the resistance of torsional loads in the cross sections of a fixed wing structure. Traditionally, while designing an airframe for a fixed wing, the requirements for greatest stiffness with minimal mass, as well as giving sufficient tolerance against local buckling, are taken into account. The optimal configuration of the supporting structural components is defined by the number and location at which a feasible design solution is achieved.

The optimization of a fixed spar wing's structural topology for maximum stiffness and minimal mass results in a concentration of structural material at the wing's root due to the presence of the largest structural strains there [2]. In fact, topology optimization algorithms seek for optimal material distribution with minimal overall mass and the least amount of elastic deformation based on the nodal displacements field in the finite element model. As a result, accounting for all of the strains in the structure, both large, at the root of the wing, and small, at the wing tip panels, requires tremendous computational power [1].

The optimization of the rib spacing along the wing span for maximum stiffness and maximum margin against local buckling results in concentration of the structural components at the root of the wing [7]. This is explained by the fact that the critical force is most quickly achieved near the base of the wing, where the panels of the upper skin lose stability under compression (Fig. 1).

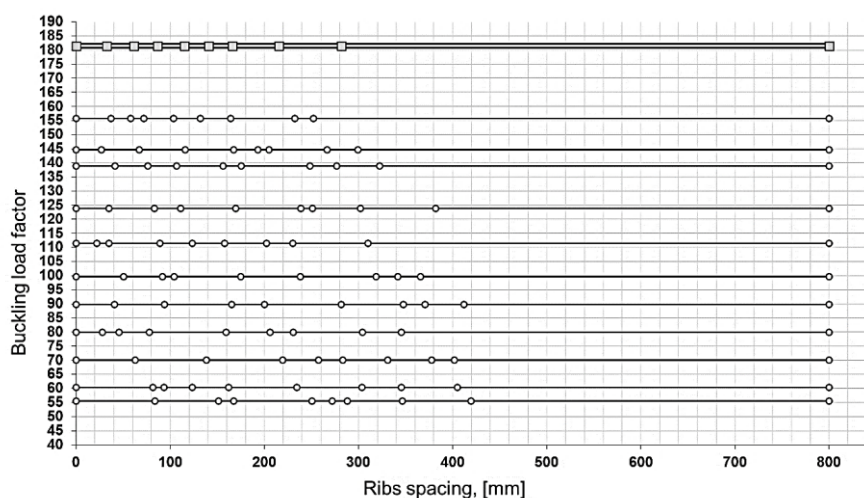


Fig. 1. Influence of the wing ribs spacing on the buckling load factor λ_{min} .

A substantial part of the skin at the outer half of the wing is weakened as a result of the accumulation of structural components at the root of the wing. In fact, this area of the skin is unsupported, which means that in flight, it will be susceptible to the variable aerodynamic loads. The aerodynamic characteristics of the wing's outer surface alter as a result of the skin's deflections caused by the air pressure. In order to maximize the skin stiffness, the arrangement of the structural components must be designed optimally while taking into consideration a tolerance for the maximum permitted corrugation of the panels.

The mass of the wing will certainly increase due to the skin being divided into several separate panels, but this will also benefit the wing's stiffness and stability against buckling. The quantity and placement of the stringers and the ribs determine the shape and the area of the panels. The stringers assist in supporting the skin, transfer the aerodynamic load to the ribs, and contribute to preventing the wing from bending. The ribs also act as a support for the skin and transmit the shear flows that develop in their planes to the longitudinal webs. Additionally, they prevent compression between the upper and lower skin panels as the wing bends during flight thus maintaining the aerodynamic shape of the cross-sections [6].

Due to the fact that the rib in the spar wing weighs more than the stringer, an optimization problem aimed at establishing the optimal number and position of the stringers and ribs must be solved in order to achieve the minimal mass of the structure. The optimal solution should have minimal mass, maximum stiffness, stability against buckling and relative panel deflections that remain within a specified tolerance.

2. Methodology

The required aerodynamic characteristics of the wing surface introduce an additional constraint in the optimization problem. It is necessary to develop a numerical procedure for the optimal design of the ribs and stringers configuration while taking into account a previously specified tolerance for the relative deflection of the panels [6,9].

Based on a previously obtained distribution of the pressure coefficients at the control points of the discrete aerodynamic model of the wing surface using the vortex panel method, an algorithm is developed for determining the required number and location of the stringers and ribs supporting the skin (Fig. 2).

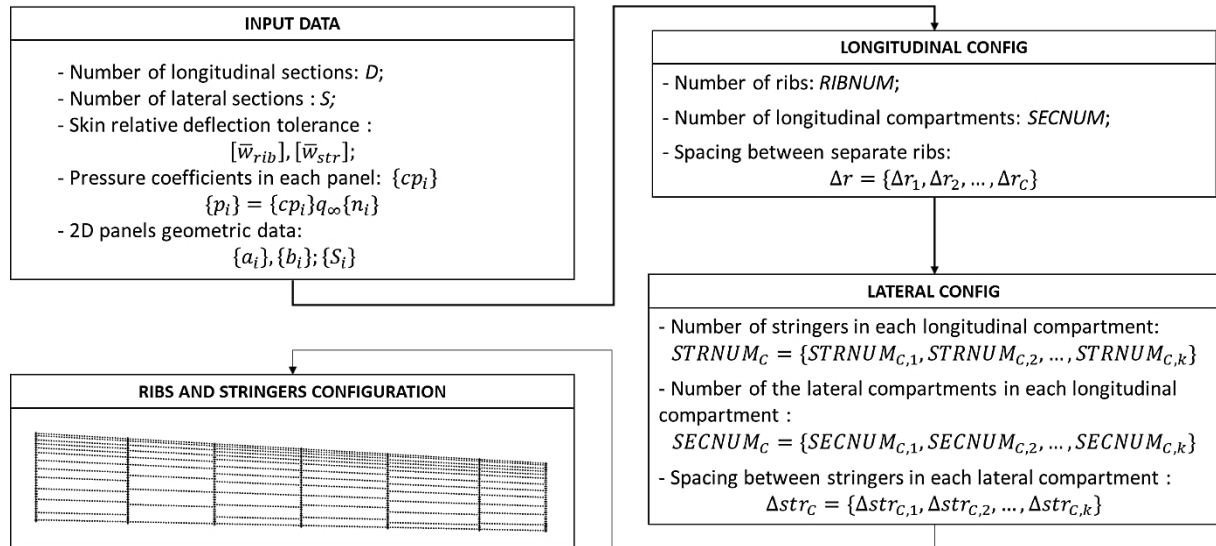


Fig. 2. Flowchart of a numerical procedure for determining the necessary number and position of the stringers and ribs in the structural layout of a fixed wing subjected to an aerodynamic load with known pressure coefficients distribution

The numerical procedure implements a sequential scanning of the control points with subsequent merging of panels of the discrete aerodynamic model until a deflection greater than or equal to the specified tolerance is reached. In this context, it is appropriate to divide the algorithm into two stages: longitudinal and lateral configuring.

The **longitudinal configuring** is defined as a subprocedure aimed at determining the number of ribs along the span of the wing through successive merging of panels along the whole chords in the sections of the discrete aerodynamic model. As a result, at each iteration the algorithm forms separate longitudinal compartments, the length of which defines the spacing between the ribs. A flowchart of the numerical procedure for the longitudinal configuring of the load-bearing structure of a fixed wing is presented in Fig. 3.

The **lateral configuring** is implemented as a subprocedure scanning chordwise each of the longitudinal compartments generated as a result of the longitudinal configuring algorithm. By merging panels along the entire length of each of the compartments, the aim is to determine the number of stringers, as well as the spacing between them. A flowchart of the numerical procedure for the lateral configuring of the load-bearing structure of a fixed wing is presented in Fig. 4.

The relative deflection \bar{w} of a panel with side lengths a and b ($a > b$) under an uniformly distributed pressure p is defined as follows [9]:

$$\bar{w} = 11 \cdot \frac{p}{E} b \xi \left(\frac{b}{\delta_{skin}} \right)^3,$$

where the coefficient ξ takes into account the type of panel fastening as for fixed panels:

$$\xi = \xi_f = \frac{0,0026}{1 + 1,056(b/a)^5},$$

and for hinged panels:

$$\xi = \xi_h = \frac{0,013}{1 + 2,21(b/a)^3}$$

The tolerances for the relative deflection of the aerodynamic surfaces are categorized within the following intervals [6,9]:

- for smooth surface: $\bar{w} \leq 0,0001$;
- for slightly corrugated surface: $0,0004 \leq \bar{w} \leq 0,001$;
- for significantly corrugated surface: $0,001 \leq \bar{w} \leq 0,01$;
- for highly corrugated surface: $0,01 < \bar{w}$.

The numerical method for optimal design of the ribs and stringers configuration consists of looping over all the vortex panels of the discrete aerodynamic model and subsequently merging them until the tolerance for the smooth surface has been satisfied. In addition to the pressure coefficients distribution, it is necessary for the algorithm to set the thickness δ_{skin} of the skin in advance, as well as the mechanical properties of the material from which it is made. The area and dimensions of the i -th panel as well as the uniformly distributed pressure p_i are obtained directly from the discrete aerodynamic model. The accuracy of the proposed numerical method depends explicitly on the level of discretization of the aerodynamic model of the surface.

The optimal design of an aircraft fixed wing must comply with the requirements for maximum stiffness and minimal mass while maintaining the stability against buckling and the aerodynamic properties of the outer surface. The suggested numerical method for preliminary design of the ribs and stringers configuration provides a structure that satisfies the relative deflection tolerance at the stage of longitudinal configuring. The generated load-bearing structure is characterized by a larger number of ribs and a significantly smaller number of stringers. To overcome this drawback, the relative deflection tolerance of the panels in the longitudinal configuring subprocedure is converted to free parameter subject to a parameterization study, for example, with the additional objective for minimal mass. This modification actually implements a relaxation of the relative deflection tolerance \bar{w}_{rib} . The relaxation removes the parameter's physical meaning turning it into a purely mathematical parameter but, nevertheless, allows the use of a parametric study often in compliance with an additional objective criteria in order to achieve the optimal result.

This approach allows for the tightest relative deflection tolerance to be applied in the lateral configuring subprocedure. As a result of the introduced modification, the number and spacings of the ribs and stringers are determined with simultaneous consideration of two objectives: for the minimal structural mass and for the permissible corrugation of the panels under the action of the distributed aerodynamic load for the specific flight case.

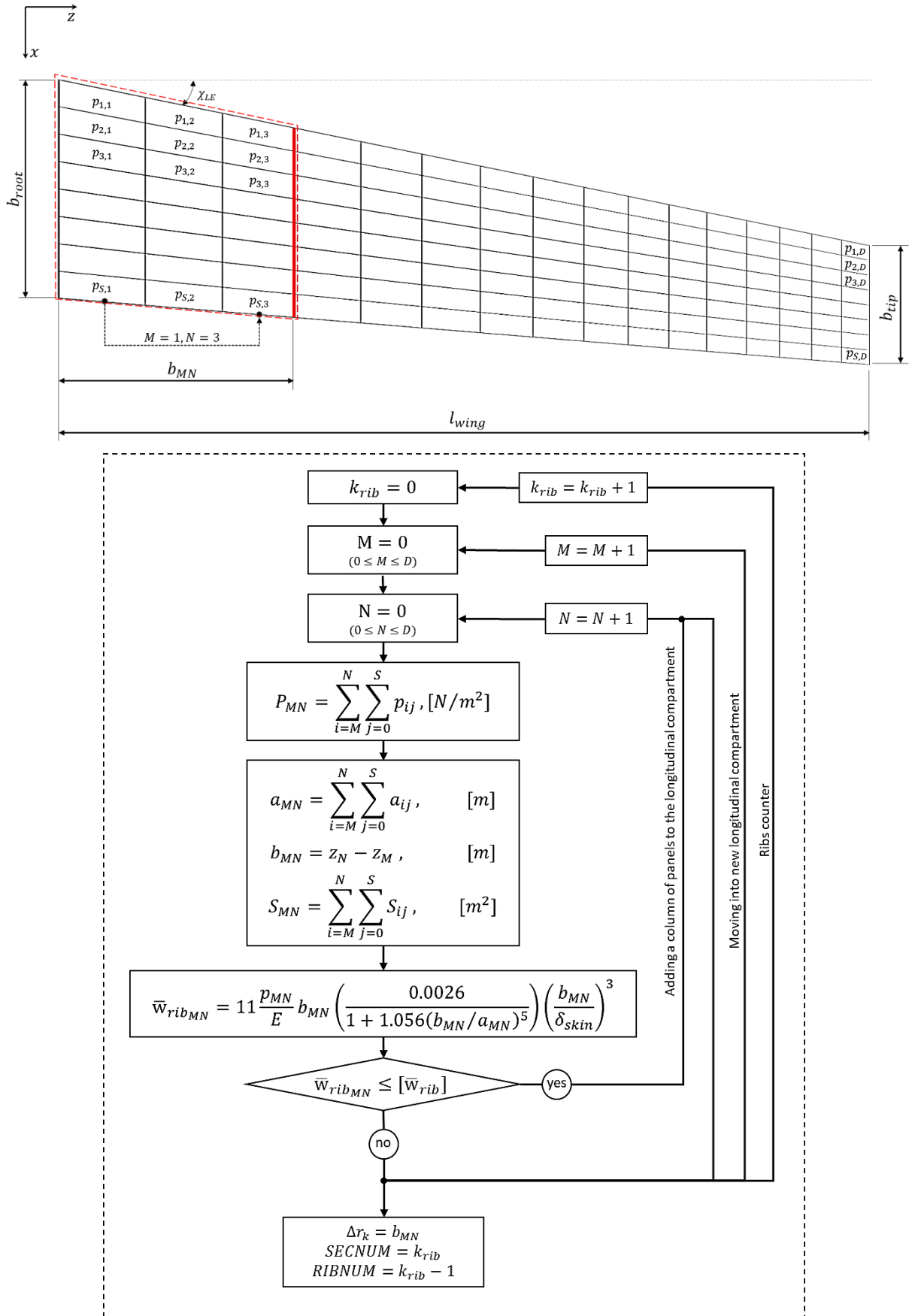


Fig. 3. Flowchart of the algorithm for optimal design of the fixed wing structural components longitudinal configuration for a known pressure coefficients distribution

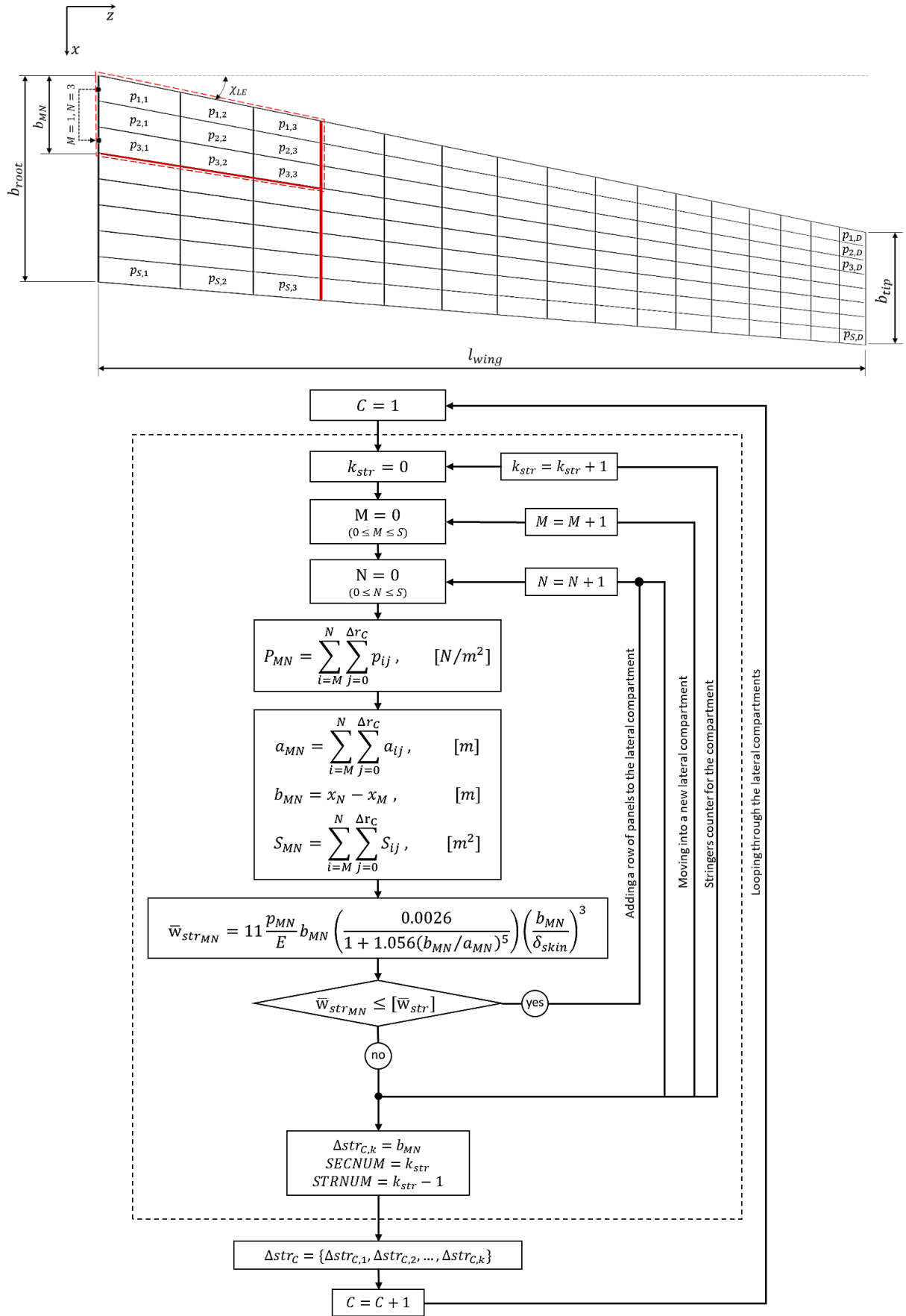


Fig. 4. Flowchart of the algorithm for optimal design of the fixed wing structural components lateral configuration for a known pressure coefficients distribution

3. Numerical experiment

The proposed numerical method is studied through optimal design of the ribs and stringers configuration of the fixed wing for a medium-altitude long-endurance intelligence- surveillance- targeting- aquisition- and- reconnaissance unmanned aerial vehicle (*ISTAR MALE UAV*). The requested general flight and technical characteristics of the aircraft as well as the specified mission profile allow estimating the maximum take-off mass by the method of successive approximations. A constraint diagram is created to determine the required power and wing area. V-n diagrams are created for flights at sea level and at cruising altitude taking vertical wind gust probabilities into account. [3,4,5].

After setting the airfoils in the wing sections, it is necessary to conduct an aerodynamic analysis to obtain the distribution of the pressure coefficients on the wing surface. Based on the distribution of the pressure coefficients derived by the vortex panel method for the flight case with never exceeded speed according to the V-n diagram, a distribution of the relative deflections in each of the panels of the discrete aerodynamic model is obtained (Fig. 5).

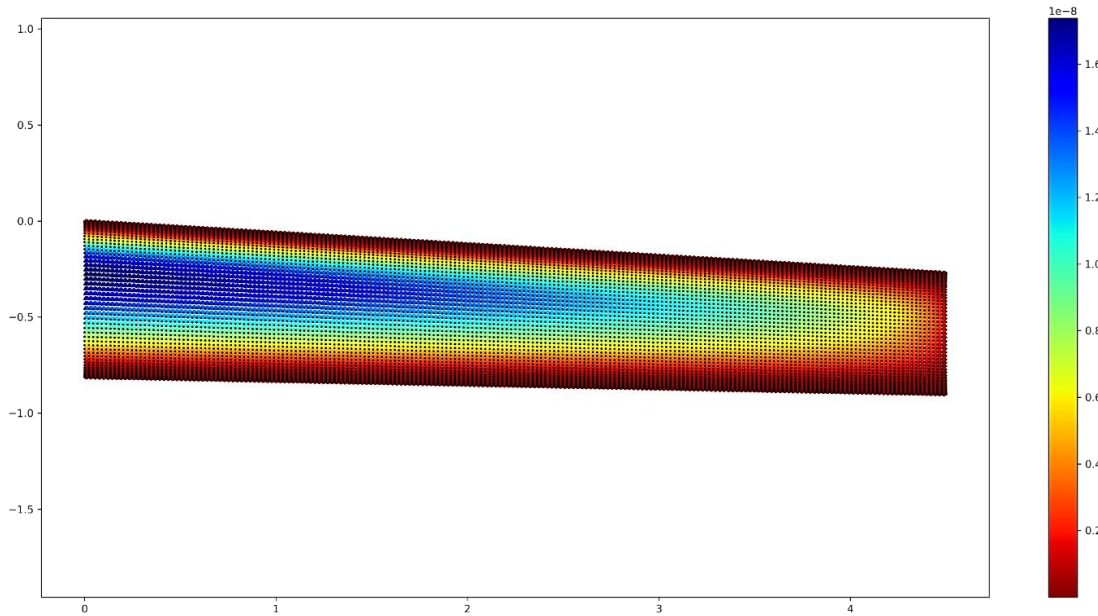


Fig. 5. Relative deflections \bar{w} at each of the panels of the aerodynamic computational model

The obtained distribution allows the identification of areas with maximum and minimum relative deflection in the panels for the considered flight case. The resulting values for the deflections form a data structure that will serve to optimally design the configuration of ribs and stringers in accordance with the proposed method.

In order to determine the number and spacing of the ribs in the load-bearing structure of the fixed wing in the longitudinal configuring subprocedure a parametric criterion is set for the relative deflection of the panels in the longitudinal compartments: $\bar{w}_{pe6} \in [1 \cdot 10^{-4}; 5 \cdot 10^4]$. For each individual configuration of the ribs, a subprocedure for lateral configuring is executed, through which the number and spacing of the stringers are determined in each of the longitudinal compartments (Fig. 6). Each of the obtained configurations satisfies the constraint for the permissible relative deflection of the panels and is feasible in the design space of the problem. In the context of classical structural optimization, the optimal configuration will be the one which corresponds to the suggested optimality criteria, i.e. has the minimum mass (Fig. 7).

The proposed numerical method for optimal design of the structural components configuration is also applicable to problems for the optimal design of dismountable hinge connected aircraft structures, where the relative deflections \bar{w} are determined by the coefficient for hinged plates ξ_h . An additional constraint is introduced for the spanwise continuity of the stringers which ensures a uninterrupted force flows between the structural components of the load-bearing structure [8]. The optimal configurations for a dismountable load-bearing structure of the designed fixed wing are presented in Fig. 8, Fig. 9 and Fig. 10.

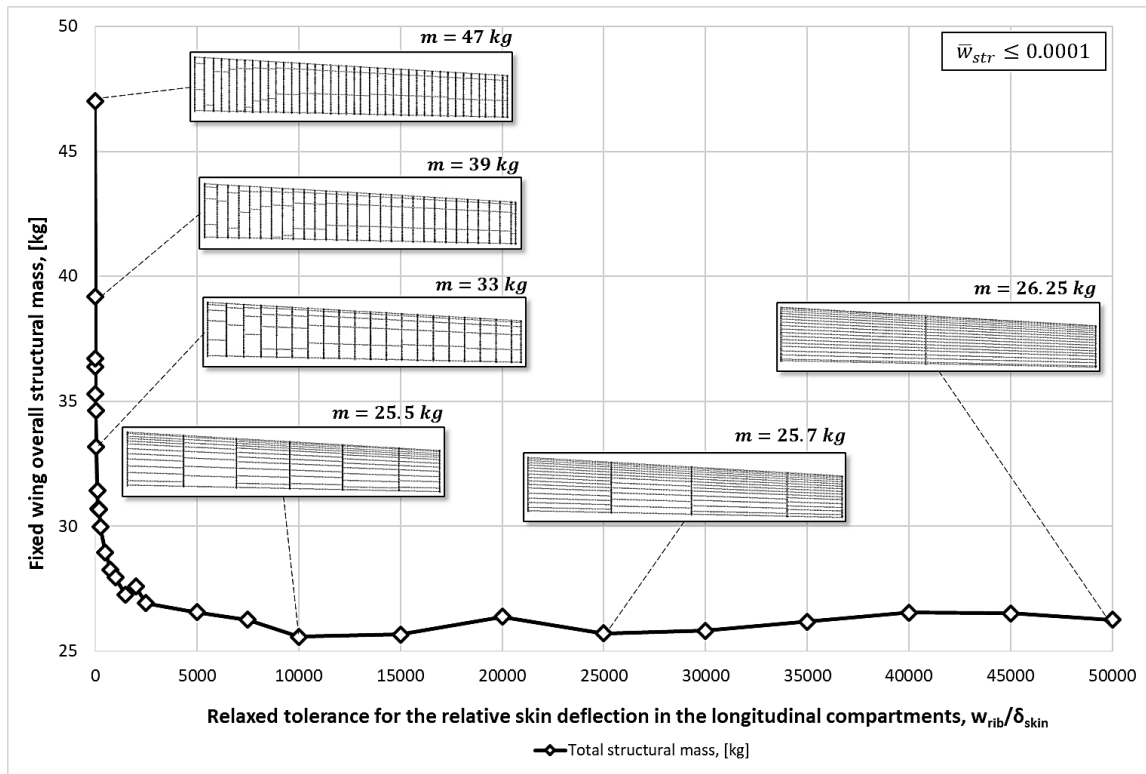


Fig. 6. Optimal design of the skin supporting structural components configuration for a MALE ISTAR UAV with relaxation of the relative deflection tolerance at the compartments between the ribs and a fixed relative deflection tolerance for the panels between the stringers

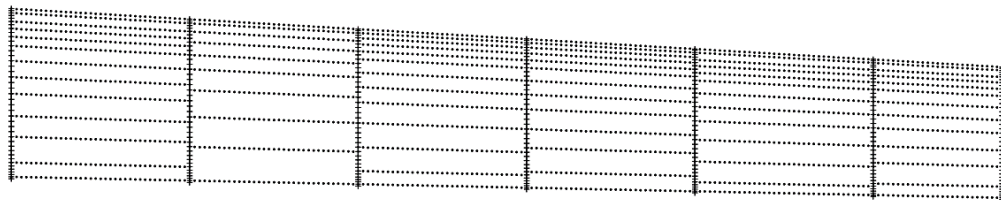


Fig. 7. Optimal ribs and stringers configuration for monolithic skin panels with the objective for minimal mass while preserving aerodynamic surface shape within the permissible deflection tolerance

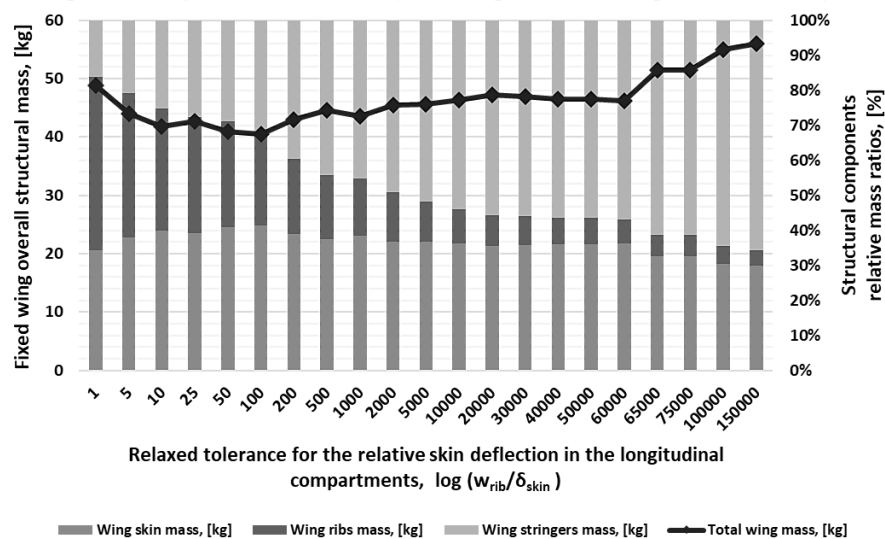


Fig. 8. Total fixed wing and skin stiffeners structural mass variation for each particular configuration depending on the relative deflection tolerance of the skin panels in the longitudinal compartments

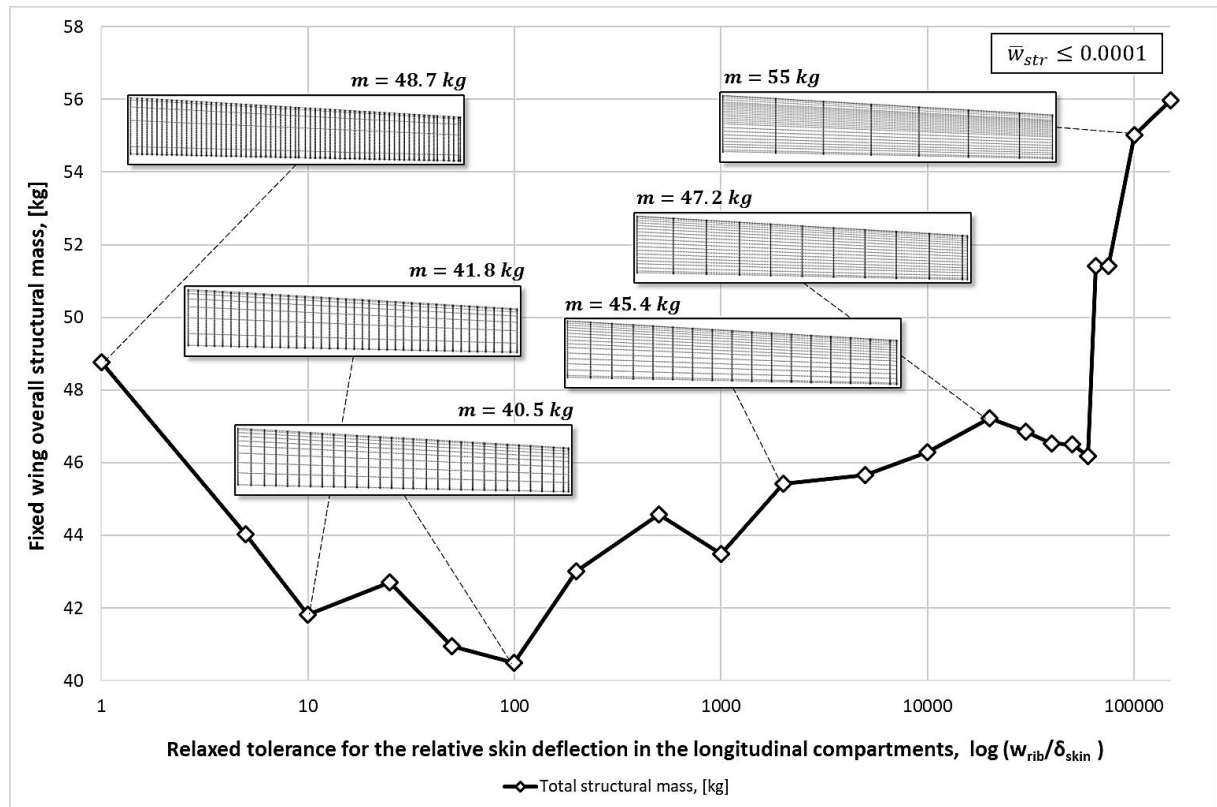


Fig. 9. Optimal ribs and stringers configurations of the load-bearing structure for an ISTAR MALE UAV fixed wing with hinged skin panels

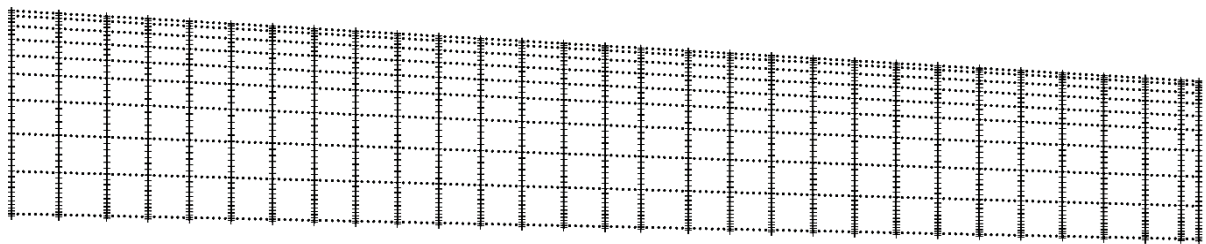


Fig. 10. Optimal ribs and stringers configuration for hinged skin panels with the objective for minimal mass while preserving the aerodynamic surface shape within the permissible deflection tolerance

4. Conclusion

The tendency to solve the problem for the optimal design of the fixed wing's structural layout topology under the objectives of maximum stiffness and minimum mass with topology optimization methods for optimal material distribution dictates the necessity for preliminary design of the skin stiffeners configuration. The requirements for providing structural stability against buckling and for maintaining the form of the aerodynamic surface cannot be ignored when considering the specifics of the applied structural loads.

A numerical method that implements a sequential scanning of the discrete aerodynamic surface model and estimates the stiffeners configuration in accordance with a predefined aerodynamic shape-preserving tolerance can be developed provided that the distribution of the pressure coefficients on the wing surface is obtained. The method was modified during the study to incorporate the possibility of taking another optimal design objective into account, more precisely the objective for minimum of the structural mass. A design problem for the fixed wing supporting structure of an ISTAR MALE UAV is used to demonstrate the method for optimal design of the ribs and stringers configuration.

The final configuration is determined by the result with minimal structural mass among all of the feasible candidates from a conducted parametric study. The problem is solved under the assumption of monolithic as well as dismountable hinged skin panels. In the first case, the placement of the stringers

in the separate longitudinal compartments depends only on the established tolerance for preserving the shape, while in the second case the stringers are placed under the additional constraint for uninterrupted force flows in the structure. The pre-designed configuration of the skin stiffeners provides an opportunity to implement various topology optimization methods for optimal design of the internal load-bearing structure of the fixed wing under the objectives of minimal structural mass and maximum stiffness. In this case, the topology optimization algorithm will distribute the structural material to resist the principle acting load, notably the wing's bending moment, with significantly lower processing power, generating a spanwise spar-like load-bearing structure.

References

1. Aage N., E. Andreassen et al. Giga-voxel computational morphogenesis for structural design. *Nature*. 2017, Vol. 550, Issue: 7174, pp. 84-86, ISSN: 1476-4687. Retrieved from: doi:10.1038/nature23911.
2. Bendsoe M., O. Sigmund. Topology optimization: theory, methods, and applications. 2004, Heidelberg, Springer, ISBN: 9783662050866.
3. EASA Easy Access Rules for Normal, Utility, Aerobatic and Commuter Category Aeroplanes, CS-23: Amendment 4. 2018, European Union Aviation Safety Agency. [accessed 01 February 2023]. Retrieved from: <https://www.easa.europa.eu/downloads/47182/en>.
4. Federal Aviation Regulations (FAR) Part 23: Airworthiness Standards: Normal, Utility, Acrobatic and Commuter Category Airplanes. 2016, Federal Aviation Administration. [accessed 01 February 2023]. Retrieved from: <https://www.ecfr.gov/current/title-14/chapter-I/subchapter-C/part-23>.
5. NATO. Light unmanned aircraft systems airworthiness requirements - AEP-83 EDITION B. STANAG 4703/24.11.2016:Ed.2, 2016, United States Department of Defense.
6. Зайцев В., В. Рудаков. Конструкция и якість на самолетите. 1980, София, Военно издателство
7. Кънчев Н. Нелинейна глобална оптимизация на напречния силов набор на право крило за БВС клас I – Мини. Сборник с доклади от Годишна международна научна конференция на ВВБУ „Георги Бенковски“, Октомври 2021, гр. Долна Митрополия, ISSN: 2738-716X.
8. Образцов И., Л. Булычев, В. Васильев. Строительная механика летательных аппаратов. 1986, Москва, Машиностроение
9. Хертель Г. Тонкостенные конструкции. 1965, Москва, Машиностроение.

Discoveries of New Asteroids in The International Astronomical Search Collaboration Science Program

Milen Simeonov

Georgi Benkovski Bulgarian Air Force Academy (BAFA), Faculty of Aviation, Dolna Mitropoliya, Bulgaria,
E-mail: msimeonov@af-acad.bg

Abstract: The article presents the work and the results of a group of lecturers, teachers, cadets and students in the International Astronomical Search Collaboration science program. The methodology for tracking and detecting asteroids, as well as the process of confirming the new discoveries and naming the new objects by the International Astronomical Union, are addressed. With the help of a NASA's Jet Propulsion Laboratory software, are calculated the orbital elements and are presented the orbital diagrams of the new asteroids, discovered by the Georgi Benkovski Bulgarian Air Force Academy's Aerospace Society Teams.

Keywords: *IASC, asteroids, astronomical observations, orbital elements*

1. Introduction

Astronomers who study the Minor Bodies in the Solar System organize, manage and participate in various scientific and research programs. One of the most successful programs is the International Astronomical Search Collaboration (IASC) – a program, which has given very good results during the past 16 years. This scientific program enables cadets, students and pupils from universities and colleges to make real astronomical studies and discoveries of astronomical images and objects, and search for and follow up near-Earth asteroids, which are already known.

The IASC is a citizen science program, which provides high-quality astronomical data to citizen scientists around the world. These scientists are able to make original astronomical discoveries and participate in hands-on astronomy. The Collaboration itself has many gifted staff members and trainers who dedicate their time and money to keeping IASC running smoothly. Most of the IASC staff are volunteers and experienced participants, which allows IASC to continue to offer its programs for free.

Currently, near-Earth asteroids make up about a third of the roughly one million asteroids discovered so far in the Solar System. Most of them reside in the Main Asteroid Belt (MAB), located between Jupiter and Mars. Professional astronomers, amateur-astronomers, cadets, students and pupils from universities and colleges from all over the world, have made the discoveries.

A group of lecturers, cadets and students from Georgi Benkovski Bulgarian Air Force Academy (BAFA) has been taking part in the IASC program, since 2020. They have participated in several observational research campaigns. They have followed up hundreds of asteroids and have discovered three new asteroids, since October 2022.

2. 30,000 Near-Earth Asteroids Discovered, and Numbers are Rising

The International Astronomical Search Collaboration was started in October 2006 by a group of lecturers from Hardin-Simmons University (HSU), Abilene, Texas and is organized and sponsored by National Aeronautics and Space Administration (NASA). Since then, Program Director has been the Professor of Mathematics and Astronomy – Dr. Patrick Miller, who also teaches Introductory Astronomy, as well as Astronomical Research Methods at HSU.

We have now (October 13, 2022) discovered 30,039 near-Earth asteroids in the Solar System – rocky bodies orbiting the Sun on a path that brings them close to the Earth's orbit. The majority of these were discovered in the last decade, showing how our ability to detect potentially risky asteroids is rapidly improving. An asteroid is called a near-Earth asteroid (NEA) when its trajectory brings it within 1.3 Astronomical Units (au) of the Sun. 1 au is the distance between the Sun and the Earth, and so NEAs can come within at least 0.3 au, 45 million kilometers, of our planet's orbit.

Astronomers have catalogued asteroids for more than two centuries since Giuseppe Piazzi discovered the very first asteroid, Ceres, in 1801. The first near-Earth asteroid, (433) Eros, was discovered nearly one hundred years later, on August 13, 1898. Carl Gustav Witt and Felix Linke, at the Urania Observatory, in Berlin and independently by Auguste Honoré Charlois at the Nice Observatory, discovered the roughly 30 km Eros asteroid. The stony asteroid's orbit brings it to within around 22 million kilometers of Earth – 57 times the distance of the Moon.

Not only is Eros the first known NEA, but the first asteroid to be orbited by a spacecraft and the first to have a spacecraft land on it. Early calculations of the space rock's orbit also enabled a precise determination of the then imperfectly known distance between the Sun and the Earth [6].

Bulgarian teams of pupils from secondary schools in Varna and Shumen, as well as students from The University of Shumen, have been taking part in the program, since 2008. Teams of lecturers, cadets and students from Nikola Vaptsarov Bulgarian Naval Academy have been participating in the IASC program, since 2017, and a group of lecturers, cadets and students from Georgi Benkovski Bulgarian Air Force Academy – since 2020.

So far, Bulgarian participants have followed up several thousand asteroids, over 250 preliminary and over 40 provisional discoveries have been made, three new of which have come as a result of the work of Georgi Benkovski Bulgarian Air Force Academy's Aerospace Society Teams.

3. Participation of Georgi Benkovski Bulgarian Air Force Academy's Aerospace Society Teams in The International Astronomical Search Collaboration Science Program for the Period March 2022 – April 2023

The Georgi Benkovski Bulgarian Air Force Academy's Aerospace Society joined the IASC program in May 2020. Aerospace Society is the name of the group of lecturers, cadets and students from BAFA who take part in the program. Each year, the Society participates in more than 10 observational campaigns.

Following their participation in each of the observational campaigns, the cadets and the students receive a Certificate for participation and/or a Certificate for discovery (preliminary discovery) of a new asteroid (*Figure 1*).



Figure 1. Certificates for participation of the Aerospace Society's team members in various campaigns of The IASC science program for the period March 2022 – April 2023 (chronologically)

The new asteroids are given preliminary temporary designations. After their following up and the refinement of their orbital elements, the asteroids are assigned a permanent number (are linked) and they could be named.

After these asteroids have been monitored for a period of 5-7 years, their orbital elements are refined and these discoveries are designated as provisional. Then, an opportunity is given to the people who

have discovered them to name them in accordance with the requirements of the International Astronomical Union: Division F Working Group for Small Bodies Nomenclature (SBN) [3].

The WGSBN is a Working Group (WG) of the International Astronomical Union (IAU) and is responsible for assigning names to minor planets and comets. It is a functional WG, which means that it exists beyond the regular three-year lifespan of IAU WGs.

There are 15 members of the WGSBN, 11 of whom are voting members. The other four members, who are ex-officio, are representatives for the IAU WG Planetary System Nomenclature (PSN) and the Minor Planet Center (MPC), as well as the IAU President and General Secretary (PGS). There are currently more than 24,000 named minor planets [9].

The following up of the newly discovered asteroids makes it possible for their orbits to be refined [1, 2, 4].

The members of the Georgi Benkovski Bulgarian Air Force Academy's Aerospace Society Teams are Milen Simeonov, Kristiyana Nikolova, Nikolay Manev, Aneliya Bliznakova, Radina Bodurova, Borislav Ivanov, Aleks Sandev, Siyana Yankova, Ivan Yankov and Vasilena Markova.

The periods of the campaigns, in which cadets, students and lecturers from BAFA's Aerospace Society Teams participated for the period March 2022 – April 2023, are as follows:

- September 21 – October 17, 2022 – International Asteroid Search. Campaign (**IASC**);
- November 18 – December 13, 2022 – All Bulgaria Asteroid Search Campaign (**All BG ASC**);
- January 16 – February 10, 2023 – International Asteroid Search Campaign (**IASC**);
- March 17 – April 12, 2023 – International Asteroid Search Campaign;
- April 17 – May 12, 2023 – All Bulgaria Asteroid Search Campaign (**All BG ASC**) and International Asteroid Search Campaign (currently participating in both, May 03, 2023).

4. Following Up and Discovering New Asteroids in The International Astronomical Search Collaboration Science Program

The participation of the Georgi Benkovski Bulgarian Air Force Academy's Aerospace Society Teams in the IASC program has been extremely successful. The members of the BAFA Aerospace Society Teams have processed thousands of astronomical images and have made dozens of preliminary discoveries, as well as three new provisional discoveries. This means that, the teams of BAFA's Aerospace Society Teams have discovered three new objects in the Solar System and the orbit of a large number of new asteroids is yet to be confirmed.

In Table 1, the results of the scientific and research work of the Georgi Benkovski Bulgarian Air Force Academy's individual teams, are summarized and presented for the period March 2022 – April 2023.

Table 1: *Summarized results of the individual teams' work in the astronomical campaigns for the period March 2022 – April 2023*

Year	Campaigns	Processed images	Preliminary discoveries	Provisional discoveries	Participants
since March 2022	All BG ASC IASC	> 600 in total	12 in total	2021 VM21 2021 VZ17 2021 VC680	SSS / SC / ASS
2023	IASC All BG ASC	> 750 in total	5	0	SSS / SC / ASS

Note: The data in the table is as at 23h59min59sec on May 03, 2023. The scientific and research work of the Georgi Benkovski Bulgarian Air Force Academy's Aerospace Society Teams continues uninterrupted and new astronomical images are being processed. New preliminary discoveries are being made, as well.

In Figure 2, Certificates certifying the discovery of the three new asteroids, part of the MAB, located between Jupiter and Mars, are presented.



Figure 2. Certificates for the discovery of the three new asteroids

5. Orbital Elements of the Three New Asteroids Discovered by the Georgi Benkovski Bulgarian Air Force Academy's Individual Teams

The orbital elements make it possible to calculate the ephemeris of the object, which means that, it can be observed and followed up at any time. The accuracy of the astrometric calculations affects the accuracy of the calculated orbital elements. Accurately calculated orbital elements, allow an accurate ephemeris to be made (table with object coordinates). The correct ephemeris will show the exact position of the object in the sky, which will allow it (the object) to be observed with telescopes. As a result of these observations, it will be possible to obtain a new image of the asteroid with the CCD matrix of the telescope [5].

Because of that, very accurate and precise calculations of the positions of asteroids have to be made. The asteroids, discovered by the teams of Georgi Benkovski Bulgarian Air Force Academy, are part of the MAB, located between Jupiter and Mars.

Chronologically, the asteroids were discovered, as follows:

- **2021 VM21** asteroid – discovered by the members of the **Space Cadets – Bulgarian Air Force Academy Team**, citizen scientists Milen Simeonov (Team Leader), Kristiyana Nikolova and Nikolay Manev;
- **2021 VZ17** asteroid – discovered by the members of the **Aerospace Society – Bulgarian Air Force Academy Team**, citizen scientists Milen Simeonov (Team Leader), Kristiyana Nikolova and Nikolay Manev;
- **2021 VC68** asteroid – discovered by the members of the **Aerospace Society – Bulgarian Air Force Academy Team**, citizen scientists Milen Simeonov (Team Leader), Kristiyana Nikolova and Nikolay Manev.

Almost all of the asteroids in our Solar System are orbiting in a broadband 31,221,273.6 km wide, between Jupiter and Mars.

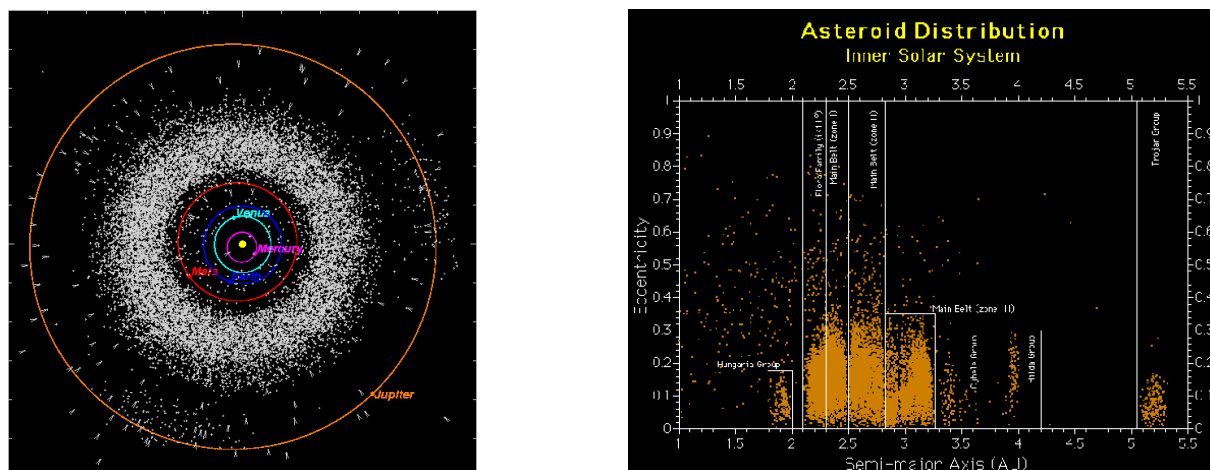


Figure 3. Asteroid Distribution, Inner Solar System, Solar System Orbits Diagrams and Distribution Graphs (image: Solar System Dynamics Group, NASA Jet Propulsion Laboratory, California Institute of Technology, http://ssd.jpl.nasa.gov/orbit_diagrams.html) [8]

The chart presented on Figure 3 shows how asteroids compare to each other in terms of how far they are from the Sun (Semi-Major Axis, SMA, AJ) and what the shape of their orbit is. Just like many other bodies in the Solar System, the orbits made by asteroids are not perfect circles, but ellipses. The axis marked Eccentricity is a measure of how far from circular each orbit is. The smaller the eccentricity number is, the more circular the orbit is [8].

With the help of Orbit Viewer software of NASA's Jet Propulsion Laboratory (JPL), implemented using two-body methods, the orbital elements and the orbital diagram of each of the three newly discovered asteroids, are calculated and presented.

The members of the **Space Cadets – Bulgarian Air Force Academy Team**, citizen scientists Milen Simeonov (**Team Leader**), Kristiyana Nikolova and Nikolay Manev, discovered the **2021 VM21** asteroid.

The **2021 VM21** asteroid is part of the MAB, located between Jupiter and Mars.

The discovery was made using astronomical images, taken on November 1, 2021. The orbital elements were calculated on the base of 32 astronomical images. As a result of the processing of these astronomical images and the calculated equatorial coordinates, it is determined that the period of the **2021 VM21** asteroid orbiting the Sun is 5.6852918 years.

The orbital elements of the **2021 VM21** asteroid are presented in Figure 4.

Osculating Orbital Elements				Miscellaneous Details	
Epoch 2460000.5 (2023-Feb-25.0) TDB Reference: JPL 2 (heliocentric IAU76/J2000 ecliptic)				solution date	2021-Dec-03 23:41:53
Element	Value	Uncertainty (1-sigma)	Units	# obs. used (total)	32
e	0.2639061179064032	4.0773E-5		data-arc span	31 days
a	3.18539313984413	.00029789	au	first obs. used	2021-11-01
q	2.344748402302177	.00020194	au	last obs. used	2021-12-02
i	15.21103339140553	.0033401	deg	planetary ephem.	DE441
node	209.5894426102008	.0038573	deg	SB-pert. ephem.	SB441-N16
peri	179.1160881105756	.025543	deg	condition code	5
M	95.04173832823726	.0062459	deg	norm. resid. RMS	.47111
tp	2459452.280022145316	.080253	TDB	source	JPL
period	2021-Aug-25.78002215			producer	Otto Matic
	2076.552844036631	.29129	d	Earth MOID	1.34827 au
	5.685291838567094	7.9751e-4	y	Jupiter MOID	1.42768 au
n	0.1733642372905823	2.4319E-5	deg/d	T_{Jup}	3.090
Q	4.026037877386083	.0003765	au		

Figure 4. Osculating Orbital Elements of the **2021 VM21** asteroid (image: Solar System Dynamics, NASA Jet Propulsion Laboratory, California Institute of Technology)

The team that made the discovery, has prepared a proposal for the Name of the asteroid, which will be sent to the IASC Program Director – the Professor of Mathematics and Astronomy – Dr. Patrick Miller, for submission to the IAU Division F WGSBN. The asteroid will be named ‘Botev’, after the name of Hristo Botev (born Hristo Botyov Petkov, January 06, 1848 – June 01, 1876, aged 28 years) – a Bulgarian revolutionary and poet. Botev is considered by Bulgarians to be a symbolic historical figure and national hero. His poetry is a prime example of the literature of the Bulgarian National Revival, though he is considered to be ahead of his contemporaries in his political, philosophical, and aesthetic views.

Botev’s image was methodically built up as a revolutionary icon by 19th century postliberation intellectuals and authors, most notably by Zahari Stoyanov and Ivan Vazov. The more controversial aspects of his past, including his anarchist and early socialist views, were deliberately toned down in order not to offend Bourgeois sensibilities.

The orbital diagram of the **2021 VM21** asteroid is presented in Figure 5.

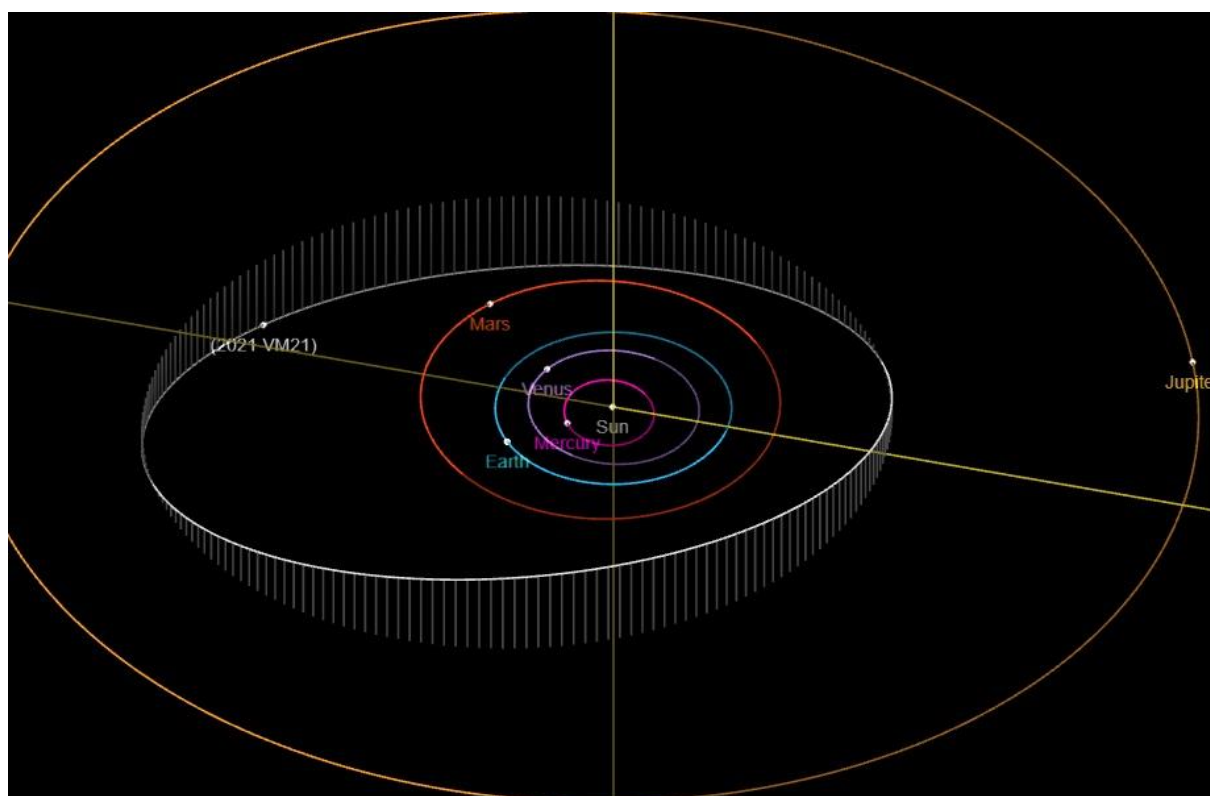


Figure 5. Orbit of the **2021 VM21** asteroid at 00h00min UTC, May 03, 2023, Earth distance: 3.231 au, Sun Distance: 3.595 au (image: Solar System Dynamics, NASA Jet Propulsion Laboratory, California Institute of Technology)

The members of the **Aerospace Society – Bulgarian Air Force Academy Team**, citizen scientists Milen Simeonov (**Team Leader**), Kristiyana Nikolova and Nikolay Manev, discovered the **2021 VZ17** asteroid.

The **2021 VZ17** asteroid is part of the MAB, located between Jupiter and Mars.

The discovery was made using astronomical images, taken on November 1, 2021. The orbital elements were calculated on the base of 14 astronomical images. As a result of the processing of these astronomical images and the calculated equatorial coordinates, it is determined that the period of the **2021 VZ17** asteroid orbiting the Sun is 4.1860746 years.

The orbital elements of the **2021 VZ17** asteroid are presented in Figure 6.

Osculating Orbital Elements

Epoch 2460000.5 (2023-Feb-25.0) TDB Reference: JPL 1 (heliocentric IAU76/J2000 ecliptic)			
Element	Value	Uncertainty (1-sigma)	Units
e	0.1654033416918195	.0021211	
a	2.597362185988218	.0034248	au
q	2.167749800841797	.0082897	au
i	8.344754131567475	.072121	deg
node	63.90960871939742	.089727	deg
peri	317.4266345587369	.32461	deg
M	130.5362113606591	.27059	deg
tp	2459446.096836058924 2021-Aug-19 59683606	.56159	TDB
period	1528.963779003457	3.024	d
	4.186074685841087	8.2793e-3	y
n	0.2354535829714944	.00046569	deg/d
Q	3.026974571134638	.0039912	au

Miscellaneous Details

solution date	2021-Nov-23 22:08:32
# obs. used (total)	14
data-arc span	11 days
first obs. used	2021-11-01
last obs. used	2021-11-12
planetary ephem.	DE441
SB-pert. ephem.	SB441-N16
condition code	7
norm. resid. RMS	.51959
source	JPL
producer	Otto Matic
Earth MOID	1.17828 au
Jupiter MOID	2.44309 au
T_jup	3.382

Figure 6. *Osculating Orbital Elements of the 2021 VZ17 asteroid (image: Solar System Dynamics, NASA Jet Propulsion Laboratory, California Institute of Technology)*

The team that made the discovery has prepared a proposal for the Name of the asteroid. The asteroid will be named ‘Prodan’ – after the name of Prodan Tarakchiev (born Prodan Stoyanov Tarakchiev, November 12, 1885 – April 29, 1957, aged 72 years) – the Bulgarian pioneer of aviation, who, while on a joint combat air mission with Radul Milkov during the First Balkan War, used the first aerial bombs on October 16, 1912, just days after the start of the first Balkan War, lasted 50 minutes and astounded the Ottoman army. The flight of the two pilots trained in Germany, France and Russia, has gone down in the history of the Bulgarian Air Force (BGRF). That is the reason why, in 1963, the Council of Ministers issued a decree declaring October 16 as the day of the BGRF.

The proposal will be sent to the IASC Program Director – the Professor of Mathematics and Astronomy – Dr. Patrick Miller, for submission to the IAU Division F WGSBN.

The orbital diagram of the 2021 VZ17 asteroid is presented in Figure 7.

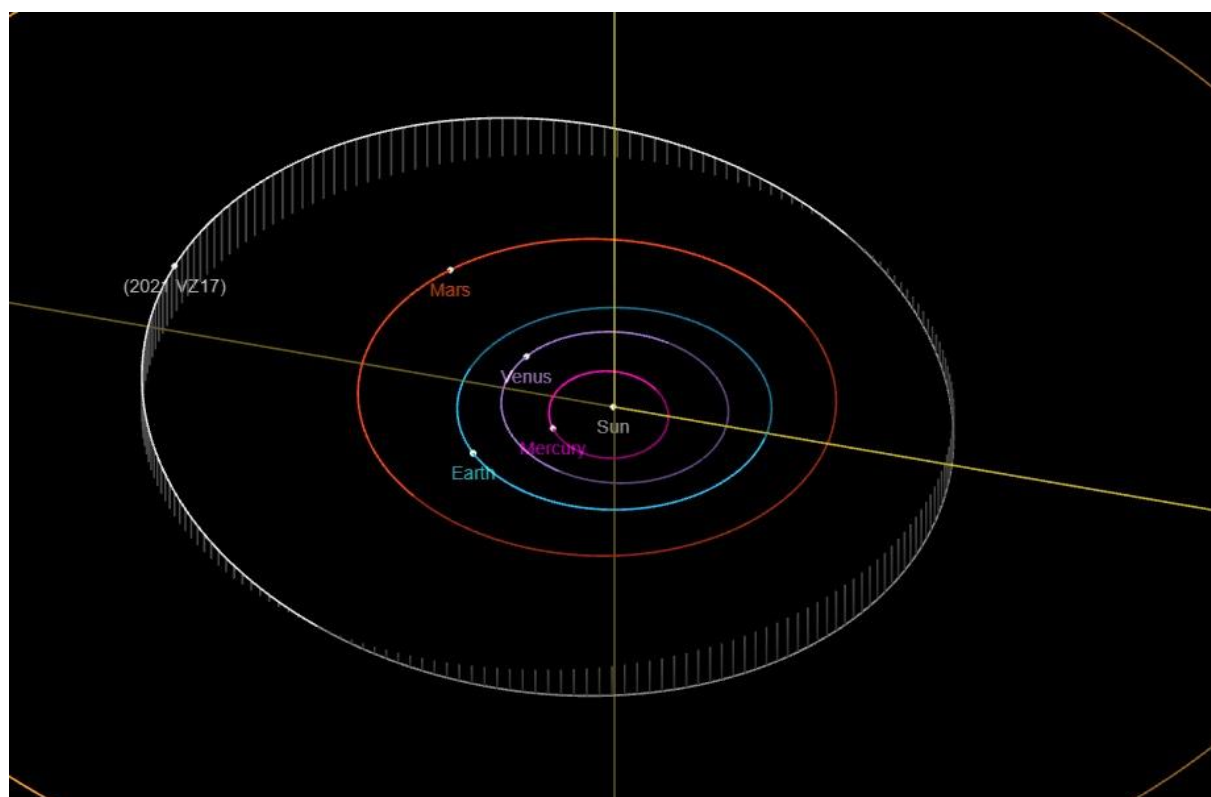


Figure 7. *Orbit of the 2021 VZ17 asteroid at 00h00min UTC, May 03, 2023, Earth Distance: 2.381 au, Sun Distance: 2.964 au (image: Solar System Dynamics, NASA Jet Propulsion Laboratory, California Institute of Technology)*

The members of the **Aerospace Society – Bulgarian Air Force Academy Team**, citizen scientists Milen Simeonov (**Team Leader**), Kristiyana Nikolova and Nikolay Manev, discovered the **2021 VC68** asteroid.

The **2021 VC68** asteroid is part of the MAB, located between Jupiter and Mars, as well.

The discovery was made using astronomical images, taken on November 1, 2021. The orbital elements were calculated on the base of 15 astronomical images. As a result of the processing of these astronomical images and the calculated equatorial coordinates, it is determined that the period of the **2021 VC68** asteroid orbiting the Sun is 5.5363827 years.

The orbital elements of the **2021 VC68** asteroid are presented in Figure 8.

Osculating Orbital Elements				Miscellaneous Details	
Epoch 2460000.5 (2023-Feb-25.0) TDB Reference: JPL 1 (heliocentric IAU76/J2000 ecliptic)				solution date	2022-Apr-15 01:06:51
Element	Value	Uncertainty (1-sigma)	Units	# obs. used (total)	15
e	0.2209314679609262	9.9448E-5		data-arc span	29 days
a	3.129526271043361	.0005818	au	first obs. used	2021-11-01
q	2.438115437959468	.00066427	au	last obs. used	2021-11-30
i	11.17837397339883	.0091483	deg	planetary ephem.	DE441
node	60.9862727116786	.0068511	deg	SB-pert. ephem.	SB441-N16
peri	315.7086545851687	.057205	deg	condition code	6
M	104.5668148759843	.020971	deg	norm. resid. RMS	.63976
tp	2459413.135481581804	.2717	TDB	source	JPL
	2021-Jul-17.63548158			producer	Otto Matic
period	2022.163789547675	.5639	d	Earth MOID	1.45371 au
	5.536382722923134	1.5439e-3	y	Jupiter MOID	1.69898 au
n	0.1780271221652753	4.9644E-5	deg/d	T_jup	3.147
Q	3.820937104127254	.00071033	au		

Figure 8. *Osculating Orbital Elements of the **2021 VC68** asteroid (image: Solar System Dynamics, NASA Jet Propulsion Laboratory, California Institute of Technology)*

The team that made the discovery has prepared a proposal for the Name of the asteroid. The asteroid will be named ‘Drinov’ – after the name of Marin Drinov (born Marin Stoyanov Drinov, October 20, 1838 – March 13, 1906, aged 68 years) – a Bulgarian historian and philologist from the National Revival period who lived and worked in Russia through most of his life.

He was one of the builders of modern Bulgaria and one of the originators of Bulgarian historiography. In 1869, as one of the eminent Bulgarian scholars, he participated in the founding of the Bulgarian Literary Society (BLS) in Braila (later renamed to Bulgarian Academy of Sciences, BAS). He was elected as its first chairman, its regular, since 1869 and Honorary Member, since 1898. He was also a long-time contributor to its periodical journal. He was a Deputy Governor of Sofia during the Russo-Turkish War (1877–1878) and the first Bulgarian Minister of Education (1878–1879).

Taking an active part in the organization of the newly liberated Bulgarian state and being a participant in the creation of the first laws on public education, Drinov is known as one of the authors of the Tarnovo Constitution.

He initiated the founding of the People’s Library of Cyril and Methodius (to which he bequeathed his personal books) and the Historical and Philological Society in Sofia.

He was a champion of the development of a unified literary language for all Bulgarian regions, which would promote their good spiritual growth and national unity. He attempted to impose an official Bulgarian spelling (so-called Drinov spelling) that was used in the first years after the Liberation.

The proposal to select the city of Sofia as the capital of Bulgaria, instead of Veliko Tarnovo (favored by Austrian diplomats), was also his [7].

The secondary school in the city of Pleven, which the Georgi Benkovski Air Force Academy inherited from the Municipality of Pleven, was named after Marin Drinov. Now the school is re-established and it functions as a Satellite Campus of the BAFA.

The first orthography of the standard Bulgarian language, established with a decree of the Minister of Education Todor Ivanchov in 1899, is attributed to Drinov. Bulgarian language underwent three orthographic reforms since: in 1921, 1923 and 1945.

The archive of Marin Drinov is part of the Scientific Archives of BAS (Collection No. 104K) and most of his works are digitized [7].

The proposal will be sent to the IASC Program Director – the Professor of Mathematics and Astronomy – Dr. Patrick Miller, for submission to the IAU Division F WGSBN.

The orbital diagram of the **2021 VC68** asteroid is presented in Figure 9.

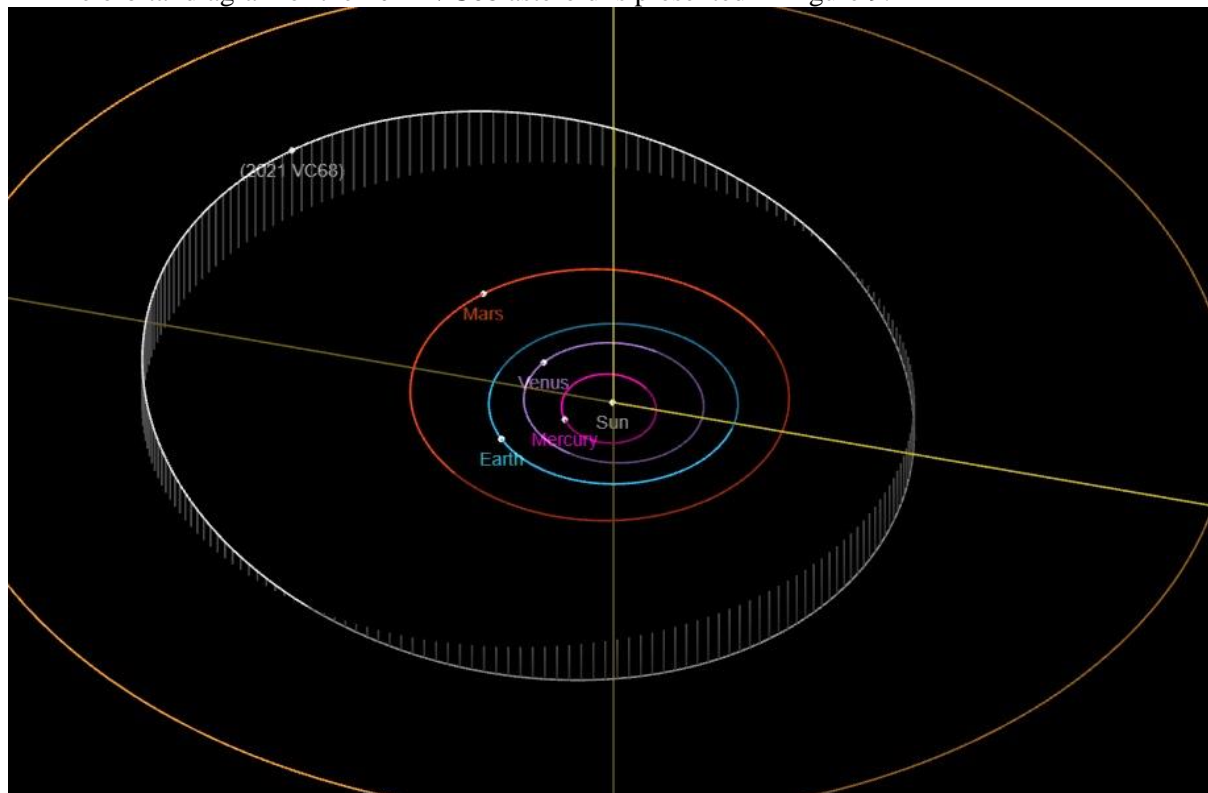


Figure 9. Orbit of the **2021 VC68** asteroid at 00h00min UTC, May 03, 2023, Earth Distance: 3.325 au, Sun Distance: 3.535 au (image: Solar System Dynamics, NASA Jet Propulsion Laboratory, California Institute of Technology)

6. Conclusions

The International Astronomical Search Collaboration Program is one of the most successful astronomical programs for cadets, students and pupils from universities and colleges, who are interested in astronomy. It creates a community, which makes real astronomical researches and discoveries of asteroids in the Solar System. The teams provide important assistance to professional astronomers, researching small bodies in the Solar System, making precise and accurate astrometric treatments.

The participation of Teams from the Bulgarian Military Academies and Universities, contributes to the discovery of new asteroids and the following up of asteroids, which are already known.

The participation of lecturers, cadets and students from the Georgi Benkovski Bulgarian Air Force Academy's Aerospace Society Teams in the International Astronomical Search Collaboration science program is a contribution to the study of asteroids in the Solar System, as a whole. In this way, Earth-hazardous objects, such as NEAs, can be detected and followed up long before a catastrophic collision with our planet Earth occurs.

In addition, the opportunity given to students to be an active part of the astronomy research process motivates them to expand their knowledge of Astronomy.

Understanding each activity in the process of work, discussing emerging problems, self-checking the results and their analysis – these are fundamental steps in mastering the difficult process of scientific knowledge and research.

References

1. RADEVA, V., D. KYURKCHIEVA, et al. Remote Astronomical Observations – An Innovation in Astronomy Education. *Chemistry: Bulgarian Journal of Science Education*. 2015, vol. 24, no. 5, p. 701-714, ISSN 1313-8235. (in Bulgarian)
2. SIMEONOV, M. D., P. G. PENEV. NASA Research Campaigns – Benefits and Prospects for Development. *Proceedings of Near Space – A Common Goal Scientific Conference*. Veliko

- Tarnovo, May 10-11, 2022, vol. 1, p. 102-112, ISSN 2815-3510. Retrieved from: doi: 10.34660/INF.2023.55.59.010. (in Bulgarian)
3. MILLER, J. P., International Astronomical Search Collaboration, *Space News*, Issue 60, June 2016.
 4. SIMEONOV, M. D., V. S. RADEVA, Detecting and Tracking Asteroids in The International Astronomical Search Collaboration Science Program. *Aeronautical Research And Development*. Dolna Mitropoliya, 2022, vol. 1, p. 58-69, ISSN 2815-2948.
 5. ASTOMETRICA. *Shareware for Research Grade CCD Astrometry* [online]. 2018 [accessed 29 April 2023.]. Retrieved from: <http://www.astrometrica.at/>.
 6. EUROPEAN SPACE AGENCY (ESA). 30,000 near-Earth asteroids discovered, and numbers are rising. *PHYS.ORG. News and Articles on Science and Technology* [online]. 2022 [accessed 02 May 2023.]. Retrieved from: <https://phys.org/news/2022-10-near-earth-asteroids.html>.
 7. PETROVA-TANEVA, M. *Marin Stepanovich Drinov*. SESDIVA [online]. N.d. [accessed 02 May 2023.]. Retrieved from: <https://sesdiva.eu/en/virtual-rooms/modern-authors/item/59-marin-stepanovich-drinov-en>.
 8. QUALITY REASONING GROUP. Northwestern University. *Space Environment*. N.d. [accessed 02 May 2023.]. Retrieved from: <https://www.qrg.northwestern.edu/projects/vss/docs/space-environment/2-how-asteroids-orbit.html>.
 9. WGSBN-IAU. *IAU: WG small bodies nomenclature (WGSBN)* [online]. N.d. [accessed 29 April 2023.]. Retrieved from: <https://www.wgsbn-iau.org/>.

Synthesizing and investigating the performance of Intelligent fuzzy logic controller for mechatronic system control

Radostina Calovska

Pleven, Bulgaria, radostina.calovska@gmail.com
Air Force Academy, Aviation Faculty, Dolna Mitropolia, Bulgaria

Abstract: In modern technologies and mechatronic systems, there is a constant increase in the application and implementation of different possibilities for their logical control. Such controllers can be built on the basis of fuzzy set theory and, through logical operations, to perform pre-set tasks to achieve a certain goal. Management methods that are performed by intelligent systems with logical structure and operations are increasingly common. Unlike algorithms in other types, the work of fuzzy controllers is based on knowledge bases, through which logical decisions are made for the management of various systems.

Keywords: *Fuzzy logic controller, Membership function, logic operation, climate control.*

1. Introduction

In the presented material, an example mathematical model of an automatic car window control system is considered, through which it is possible to analyze the operation of an intelligent controller with set parameters of the system, control rules and the desired final state of the temperature in the passenger compartment. The used model is described in the material [1]. Fuzzy Logic Toolbox [5] provides MATLAB functions, applications, and a Simulink block for analyzing, designing, and simulating fuzzy logic systems.

The product enables the synthesis and configuration of input and output signals, membership functions and rules of fuzzy inference systems. It is possible to automatically set membership functions and rules of a fuzzy inference system. It is possible to evaluate designed fuzzy logic systems in MATLAB and Simulink, and to use the fuzzy inference system as a support system and to explain artificial intelligence (AI) based models.

The fuzzy control controller is a system of rules based on which the input controls the output through a process of fuzzification and defuzzification. Fuzzification is the process of assigning the numerical input to a system of fuzzy sets with a certain degree of membership. This degree of membership can be anywhere in the interval 0-1. If it is 0, then the value does not belong to the given fuzzy set, and if it is 1, then the value fully belongs to the fuzzy set [3].

Defuzzification is the process of obtaining a quantifiable result in clear logic and the corresponding degrees of membership. It represents a transformation of a fuzzy set into a crisp set, which is needed in fuzzy control systems, and its result is described in terms of fuzzy set membership [2]. The degree of truth (membership) is represented graphically by membership functions. These functions characterize the fuzzing regardless of whether the elements in the fuzzy sets are discrete or continuous. They can be defined as a technique for solving practical problems through experience.

2. Synthesizing Fuzzy Logic Controller for Mechatronic System Control

Mamdani Fuzzy Interference System (Fig.1) [4] was chosen to control the system, which has more intuitive and easy-to-understand rule bases that are well suited for application in expert systems where the rules are created on the basis of human knowledge.

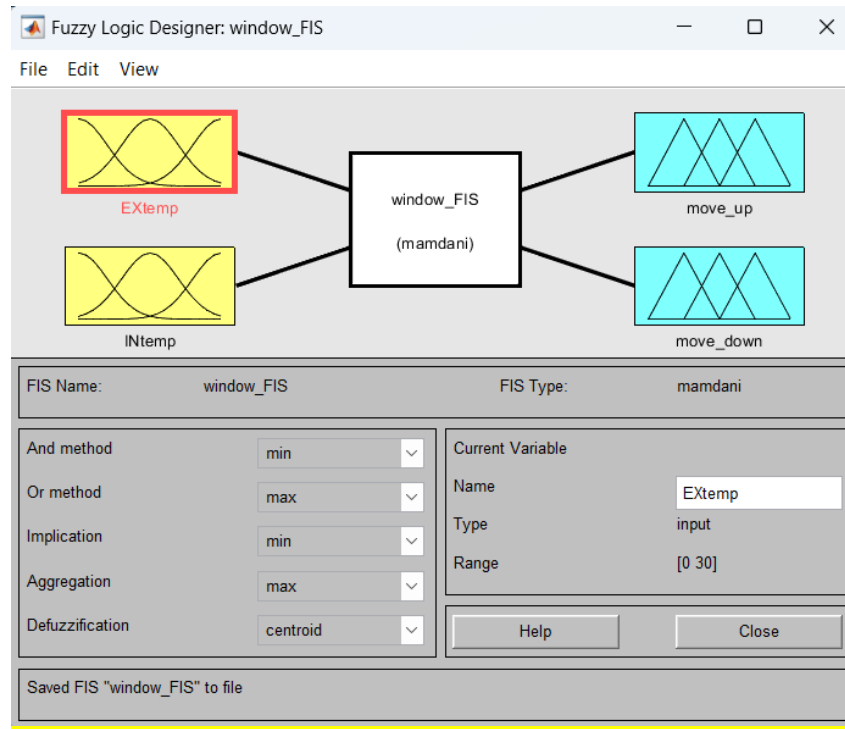


Figure 1. Fuzzy Interference System

Triangular membership functions have been synthesized for the input values of the interior temperature in the passenger compartment and the external ambient temperature. Determining the control rules and through a defuzzification process, the output of the logical Fuzzy Controller [5] is given signals to drive the window servo in the up or down direction, respectively. Fig.2 shows the general view of the Membership Functions [6], through which the management is carried out.

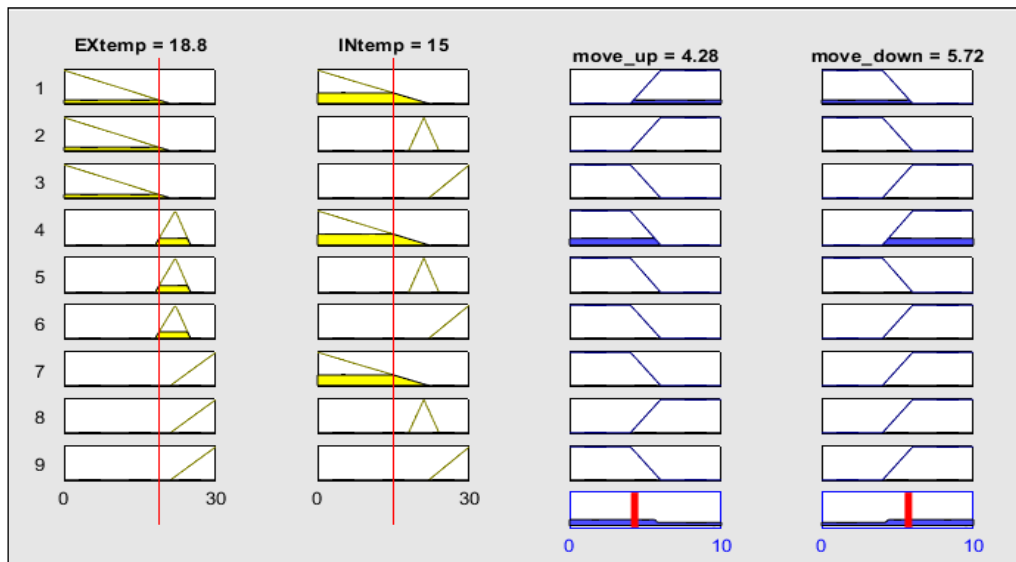


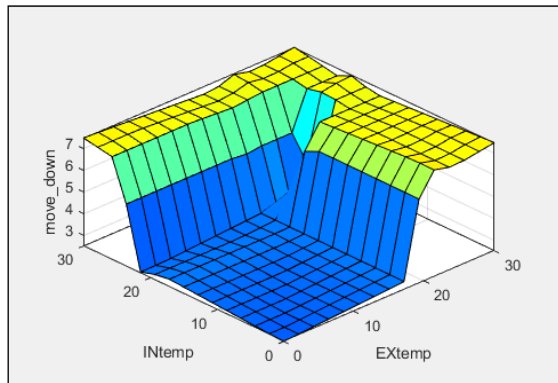
Figure 2. Membership Functions

A change in the outside temperature (EXtemp) and the temperature in the car compartment (INtemp) is detected by the synthesized Membership functions and based on 9 rules, the controller moves the position of the window, aiming to reach the desired INtemp, which is approximately 23°. The set rules state that:

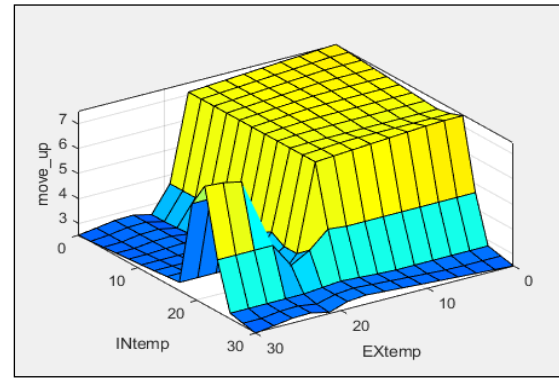
1. If EXtemp is cold and INtemp is cold, then window moves up and remains closed;
2. If EXtemp is cold and INtemp is normal, then window moves up and remains closed;
3. If EXtemp is cold and INtemp is hot, then window moves down;

4. If EXtemp is normal and INtemp is cold, then window moves down;
5. If EXtemp is normal and INtemp is normal, then window remains in neutral position;
6. If EXtemp is normal and INtemp is hot, then window moves down;
7. If EXtemp is hot and INtemp is cold, then window moves down;
8. If EXtemp is hot and INtemp is normal, then window remains in neutral position;
9. If EXtemp is hot and INtemp is hot, then window moves down.

Fig. 3 shows the relationship between the movement of the servo motor, respectively, to open (Fig. 3a) and close (Fig. 3b) the window or remain in a neutral position, according to the temperature changes in the external environment and the temperature in the car compartment.



a) Surface for move down position



b) Surface for move up position

Figure 3. Surface Viewer of the operation of Fuzzy Logic Controller according to set rules

3. Fuzzy Logic Controller performance analysis results

To verify the performance of the synthesized fuzzy controller according to the rules defined in Fig.2, simulation studies are conducted with the model described in [1]. As an example of the operation of the fuzzy controller, the control of the system at a set constant EXtemp=18°C is considered. The results of the operation of the controller when changing INtemp in the car compartment are shown in Fig.4. It can be seen that the Fuzzy Logic Controller processes the temperature changes and by changing the position of the passenger compartment window, adjusts the temperature to the desired value (approximately 23°). The stabilized temperature as a function of time is shown in Fig.5.

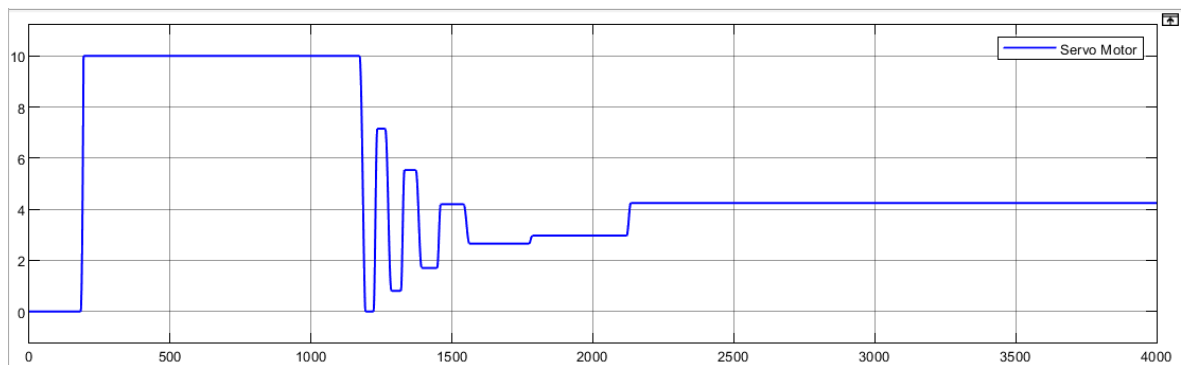


Figure 4. A graph of the window's movement as a function of time

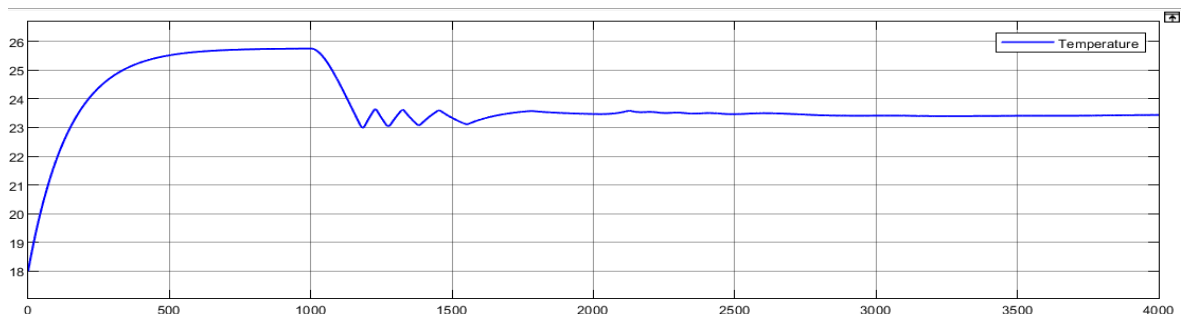


Figure 5. Graph of temperature changes in the car compartment as a function of time

4. Comparison of the performance of a finite state machine based logic controller and the performance of a Fuzzy Logic Controller

Fig.6 shows the operation of a logic controller built on the basis of finite state machines [1].

Analyzing the operation of the Finite State Machine and Fuzzy Logic Controller, it is possible to see that both controllers work at the same initial system values and, applying different logic methods, stabilize the temperature in the passenger compartment to the desired degrees, controlling the servo motor to drive the car window.

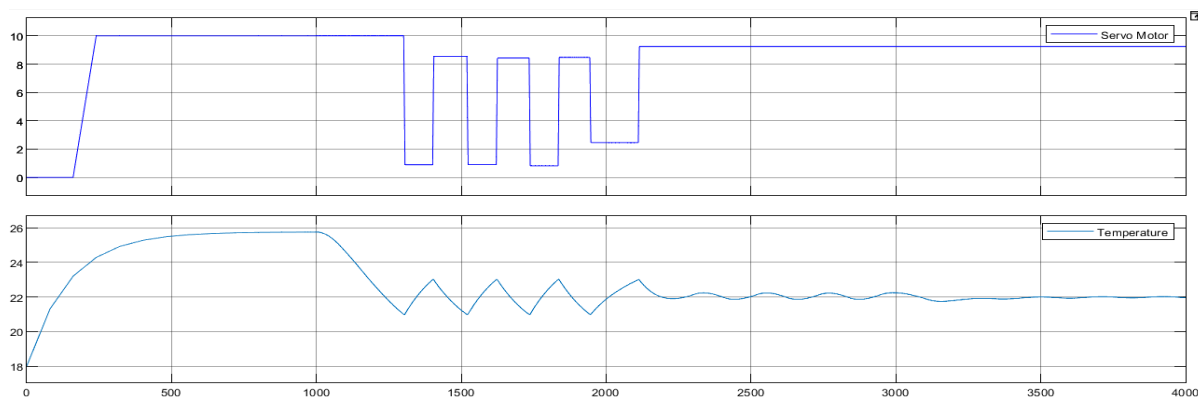


Figure 6. Graph of the operation of a logic controller based on finite state machines for the movement of the window and the temperature changes in the car compartment as a function of time

5. Conclusions

1. A Fuzzy Logic Controller is synthesized for the operation of the selected mechatronic system, and the control rules and corresponding membership functions are formulated.
2. The operation of the controller was investigated according to the set rules and the desired final state of the system was determined through the analysis.
3. A comparison is made between the performance of a logic controller based on finite state machines and a Fuzzy Logic Controller.
4. From the presented material it is established that the management of a mechatronic system can be carried out on the basis of logical operations.

References

- [1] Radostina Calovska, Stefan Biliderov "Synthesis and research of a controller for microclimate stabilization in an automobile based on finite state machines", Aeronautical Research and Development Volume1, 2022 ISSN 2815-293X ISSN 2815-2948
- [2] Defuzzification <Defuzzification - Wikipedia> 02.05.2023
- [3] Fuzzification<Fuzzy logic - Wikipedia> 02.05.2023
- [4] Fuzzy inference system < Mamdani and Sugeno Fuzzy Inference Systems - MATLAB & Simulink (mathworks.com)> 02.05.2023
- [5] Fuzzy Logic Toolbox <<https://www.mathworks.com/products/fuzzy-logic.html>> 03.05.2023
- [6] Membership function < <https://www.mathworks.com/help/fuzzy/foundations-of-fuzzy-logic.html>> 03.05.2023

Computer Modeling Investigation of the Penetration of an Aircraft Munition (Bomb) Depending on Target Structure

Milen Atanasov¹, Kolyo Kolev², Danyo Lalov³

Air Force Academy Dolna Mitropolia, Bulgaria, maa_69@abv.bg; Air Force Academy Dolna Mitropolia, Bulgaria, kolev_007@abv.bg; Air Force Academy Dolna Mitropolia, Bulgaria, danyo@abv.bg.

Abstract A study of the penetration of aviation ammunition into a whole with a different structure was made. The relationship between penetration depth and target structure is shown.

Keywords: *Penetration, Munition, Target.*

1. Introduction

To calculate the penetrating action of ammunition in a dense medium, semi-empirical formulas are used, which are obtained on the basis of integration of the equations for the movement of ammunition in a dense medium, taking into account the resistance forces of the medium determined experimentally. The impact action of the ammunition is characterized by the penetration thickness of the barrier or by the magnitude of the distance traveled S in the barrier and the time t [1, 2, 3, 4, 5].

2. Description

The barrier resistance law is [5]:

$$(1) \quad F_p = \pi R^2(a + b),$$

where F_p is the barrier force;

R – the radius of the ammunition;

a – the statistical constituent of the resistance force of the barrier has a pressure dimension;

V – ammunition movement speed in a dense environment;

b – the dynamic constituent of the resistance force has dimensional density.

The maximum path S_{\max} of the ammunition in a dense medium at $V=0$ is represented by the expression [8]:

$$(2) \quad S_{\max} = \frac{2,303m}{2\pi R^2 b} \lg \left(1 + \frac{b}{a} V_k^2 \right),$$

where V_k is the velocity of the projectile encountering the barrier, and the maximum time t_{\max} for penetration at $V=0$ is [8]:

$$(3) \quad t_{\max} = \frac{m}{\pi R^2 \sqrt{ab}} \arctg \left(\sqrt{\frac{b}{a}} V_k \right).$$

The values of the coefficients a and b are determined experimentally and are dependent on the type of medium (table 1) and on the shape of the front part of the ammunition $\lambda=f(h/d)$ (table 2), where h is the height of the front part, d – the diameter of the ammunition [5].

Table 1. Mechanical Properties

Medium	k_p	Medium	k_p
Clay	$4,2 \cdot 10^{-6}$	Granite	$1,6 \cdot 10^{-6}$
Sand	$4,5 \cdot 10^{-6}$	A brick	$2,5 \cdot 10^{-6}$
Rock	$2 \cdot 10^{-6}$	Reinforced concrete	$0,8 \cdot 10^{-6}$
Concrete	$1,2 \cdot 10^{-6}$	Reinforced concrete	$0,7 \cdot 10^{-6}$

Table 2. Shape of the Front of the Ammunition λ

h/d	0,0-0,5	0,5-1,0	1,0-1,5	1,5-2,0
λ	1,0	1,1	1,25	1,4

The depth h_m of ammunition penetration into a barrier is calculated using the formula (Fig. 1) [5]:

$$(4) \quad h_m = k_p \lambda_1 \frac{m}{d^2} V_k \sin \alpha_p,$$

where k_p is the barrier resistance coefficient;

α_p – the angle of encounter of the ammunition with the barrier.

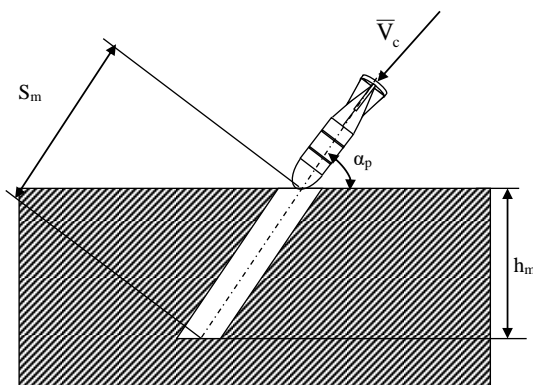


Figure 1. Penetration of the Ammunition into the Medium

The developed program is based on a mathematical model describing the free fall of a body with certain geometric and mechanical parameters. The program makes it possible to determine the depth of penetration of the aviation bomb "BETAB" in multilayer structures when released from extremely low heights (10-50 m), speeds from 150 m/s to 250 m/s and with angles of encounter of the ammunition with the partition – 10^0 - 90^0 .

3. Results

3.1 Penetration of "BETAB" aviation bomb in concrete (Table 3).

penetration coefficient: $k_p = 1.2 \cdot 10^{-6}$

- mass of the aviation bomb ("BETAB") $m = 500\text{kg}$;
- coefficient depending on the shape of the front part of the aviation bomb $\lambda = 1.4$
- bomb caliber $d = 0.46\text{ m}$

Table 3. The Depth h_m of Penetration of the Ammunition Into Concrete

h_m, m	$V=150\text{m/s}$	165	190	210	230	240	250
$\alpha_p = 90, \text{degr}$	0,595	0,655	0,754	0,834	0,913	0,953	0,992
85	0,593	0,653	0,751	0,830	0,910	0,949	0,989
80	0,586	0,645	0,743	0,821	0,899	0,938	0,977
75	0,575	0,633	0,729	0,805	0,882	0,920	0,959
70	0,560	0,616	0,709	0,783	0,858	0,895	0,933
65	0,540	0,594	0,684	0,756	0,827	0,863	0,899
60	0,516	0,567	0,653	0,722	0,791	0,825	0,859
55	0,488	0,537	0,618	0,683	0,748	0,780	0,813
50	0,456	0,502	0,578	0,639	0,699	0,730	0,760
45	0,421	0,463	0,533	0,589	0,646	0,674	0,702

40	0,383	0,421	0,485	0,536	0,587	0,612	0,638
35	0,342	0,376	0,433	0,478	0,524	0,546	0,569
30	0,298	0,328	0,377	0,417	0,457	0,476	0,496
25	0,252	0,277	0,319	0,352	0,386	0,403	0,419
20	0,204	0,224	0,258	0,285	0,312	0,326	0,339
15	0,154	0,170	0,195	0,216	0,236	0,247	0,257
10	0,103	0,114	0,131	0,145	0,159	0,165	0,172

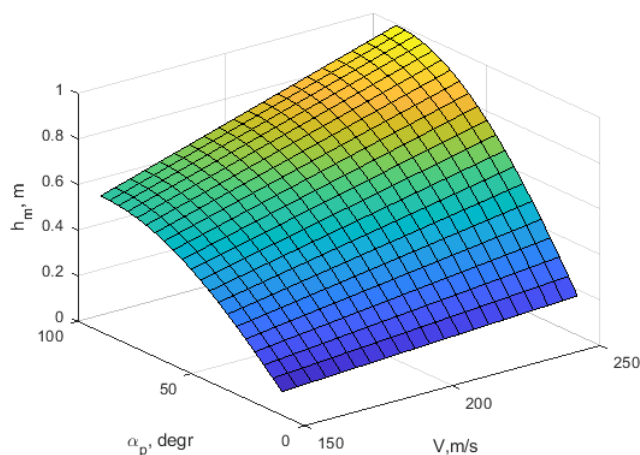


Figure. 2. Dependence of the Penetration Depth into Concrete on V and α_p

3.2 Penetration of a "BETAB" aviation bomb in a brick (table 4).

- penetration coefficient: $k_p = 2.5 \cdot 10^{-6}$
- mass of the aviation bomb ("BETAB") $m = 500$ kg;
- coefficient depending on the shape of the front part of the aviation bomb $\lambda = 1.1$;
- bomb caliber $d = 0.46$ m.

Table 4. The Depth h_m of Penetration of the Ammunition Into Brick

h_m, m	$V=150m/s$	165	190	210	230	240	250
α_p =90, degr	0,975	1,072	1,235	1,365	1,495	1,560	1,625
85	0,971	1,068	1,230	1,359	1,489	1,554	1,618
80	0,960	1,056	1,216	1,344	1,472	1,536	1,600
75	0,942	1,036	1,193	1,318	1,444	1,506	1,569
70	0,916	1,008	1,160	1,282	1,404	1,465	1,527
65	0,883	0,972	1,119	1,237	1,355	1,413	1,472
60	0,844	0,929	1,069	1,182	1,294	1,351	1,407
55	0,798	0,878	1,011	1,118	1,224	1,278	1,331
50	0,747	0,821	0,946	1,045	1,145	1,195	1,244
45	0,689	0,758	0,873	0,965	1,057	1,103	1,149
40	0,627	0,689	0,794	0,877	0,961	1,002	1,044
35	0,559	0,615	0,708	0,783	0,857	0,895	0,932
30	0,487	0,536	0,617	0,682	0,747	0,780	0,812
25	0,412	0,453	0,522	0,577	0,632	0,659	0,687
20	0,333	0,367	0,422	0,467	0,511	0,533	0,556
15	0,252	0,278	0,320	0,353	0,387	0,404	0,420
10	0,169	0,186	0,214	0,237	0,260	0,271	0,282

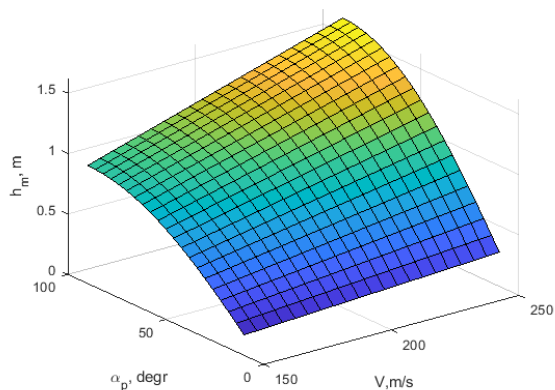


Figure. 3. Dependence of the Penetration Depth into Brick on V and α_p

3.3 Penetration of "BETAB" aviation bomb in clay (Table 5).

penetration coefficient: $k_p = 4.2 \cdot 10^{-6}$

- mass of the aviation bomb ("BETAB") $m = 500$ kg;
- coefficient depending on the shape of the front part of the aviation bomb $\lambda = 1.25$;
- bomb caliber $d = 0.46$ m.

Table 5. The Depth h_m of Penetration of the Ammunition Into Clay

h_m, m	$V=150m/s$	165	190	210	230	240	250
$\alpha_p=90,$ degr	1,861	2,047	2,357	2,605	2,853	2,977	3,101
85	1,854	2,039	2,348	2,595	2,842	2,966	3,090
80	1,833	2,016	2,321	2,566	2,810	2,932	3,054
75	1,797	1,977	2,277	2,516	2,756	2,876	2,996
70	1,749	1,923	2,215	2,448	2,681	2,798	2,914
65	1,686	1,855	2,136	2,361	2,586	2,698	2,811
60	1,612	1,773	2,041	2,256	2,471	2,578	2,686
55	1,524	1,677	1,931	2,134	2,337	2,439	2,540
50	1,425	1,568	1,806	1,996	2,186	2,281	2,376
45	1,316	1,447	1,667	1,842	2,018	2,105	2,193
40	1,196	1,316	1,515	1,675	1,834	1,914	1,994
35	1,067	1,174	1,352	1,494	1,637	1,708	1,779
30	0,930	1,023	1,179	1,303	1,427	1,489	1,551
25	0,786	0,865	0,996	1,101	1,206	1,258	1,311
20	0,636	0,700	0,806	0,891	0,976	1,018	1,061
15	0,482	0,530	0,610	0,674	0,738	0,771	0,803
10	0,323	0,355	0,409	0,452	0,495	0,517	0,539

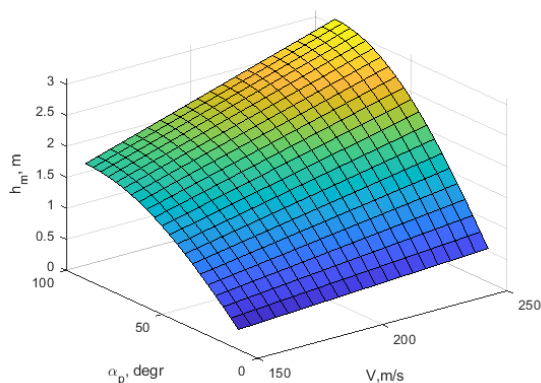


Figure. 4. Dependence of the Penetration Depth into Clay on V and α_p

It is known from practice that at angles of encounter with the partition smaller than 30° a ricochet occurs.

As constant values in the program product, the diameter of the aviation bomb d , the mass m are involved, but if it is necessary to study the penetration depth of other larger or smaller in caliber and mass aviation bombs in different environments, these constant values can be changed. The depth of penetration of the aviation bomb can be seen from the results obtained and depend mostly on the speed of encounter with the barrier, the angle of encounter and the penetration coefficient depending on the properties of the medium K_p .

As the speed of encounter with the barrier increases, the depth of penetration increases. It is greatest at an encounter speed of 250 m/s and an angle of 90° . At lower speeds of the order of 150-180 m/s and small encounter angles of $10^\circ \div 30^\circ$, it is possible to get a ricochet if the barrier is made of concrete or solid primer. At a speed of 150 \div 180 m/s and angles $10^\circ \div 30^\circ$ and penetration coefficient $K_r = 4.4 \cdot 10^{-6} \div 17 \cdot 10^{-6}$, the probability of ricochet of the aviation bomb is smaller because the barrier is of softer composition.

4. Conclusions

1. The developed software product is based on a mathematical model describing the free fall of a body with certain geometric and mechanical parameters. The program makes it possible to determine the depth of penetration of the "BETAB" aviation bomb in multi-layered structures when they are released from extremely low heights. This provides a prerequisite for the study of new aviation bombs of the "BETAB" type, with the aim of lightening the fairing (frontal part), at the expense of the "BETAB" explosive or its shape.

2. The solved tasks can contribute to the creation of new samples of aviation bombs of the "BETAB" type with a gunpowder-rocket engine.

Acknowledgments

The research in this article was carried out in fulfillment of Task 1.1.2. "Analysis and evaluation of disaster, accident, emergency and crisis management systems and development of scientifically based proposals for their improvement" by the National Scientific Program "Security and Defense", adopted by RMS No. 731 of 21.10.2021. and according to Agreement No. D01-74/19.05.2022.

References

1. Загорски Н., Асенов Св., Приблизени модели за оптимизация на параметрите за експлоатация и техническо обслужване на авиационните системи с оценка на точността и достоверността на получаваните резултати, Journal of the Technical University at Plovdiv "Fundamental Sciences and Applications", Vol. 14(2), 2009, стр. 359-364; Периодично издание, на английски език, ISSN 1314-5258
2. Загорски Н., Сотиров Г., Асенов Св., Анализ на теория на полета на делтапланер за определяне на изисквания и методи за оценка на летателната годност, Fourteenth International Scientific Conference, SPACE ECOLOGY SAFETY SES 2018, Proceedings, стр. 158-166. ISSN 1313-3888
3. Zagorski N., Jordanov D., Tsholakov St., Role of power reserve in parallel hydraulic movements of aircraft controls, Aerospace Research in Bulgaria, 34, 34, Bulgarian Academy of Sciences. Space Research and Technology Institute, 2022, ISSN:p-ISSN 1313 - 0927, DOI:https://doi.org/10.3897/arb.v34.e08, p.p. 95-105.
4. Маринов А., Определяне на силата на челно съпротивление действаща на тяло с оптимална ротационна форма при свръхзвукова скорост, Сборник научни трудове от Юбилейната научна конференция по повод 10 години от създаването на Националния военен университет „Васил Левски“, Том 7, Велико Търново, 2012 г., ISBN 978-954-753-095-9, Стр. 10-142.
5. Покровский Г. И. Сассапарель В. И. и др., Курс авиационных бомб, М., ВВИА „Н. Е. 1970 г.

Calculation of the Deformation of the Fairing of an Aviation Munition (Bomb), When Penetrating a Target With a Multi-Layer Structure

Milen Atanasov¹, Kolyo Kolev², Danyo Lalov³

Air Force Academy Dolna Mitropolia, Bulgaria, maa_69@abv.bg; Air Force Academy Dolna Mitropolia, Bulgaria, kolev_007@abv.bg; Air Force Academy Dolna Mitropolia, Bulgaria, danyo@abv.bg.

Abstract We present the results of numerical modeling of the deformation of the head of aviation bomb “BETAB” for penetration into multilayer structure by computer assisted modeling. This is a simulation of free falling body made of different materials and their interaction with solid surface.

Keywords: *Simulation, Aviation Bomb, Deformation, Free Fall.*

1. Introduction

In modern conditions, along with the development of nuclear, chemical and bacteriological weapons, unguided aviation munitions for hitting ground targets continue to be improved [1, 2, 3]. Of the existing ones, aviation bombs are widely used for hitting targets with a multi-layered structure with a caliber of 500 kg (BETAB 500) - fig. 1, for hitting highly protected objects with a reinforced concrete coating.

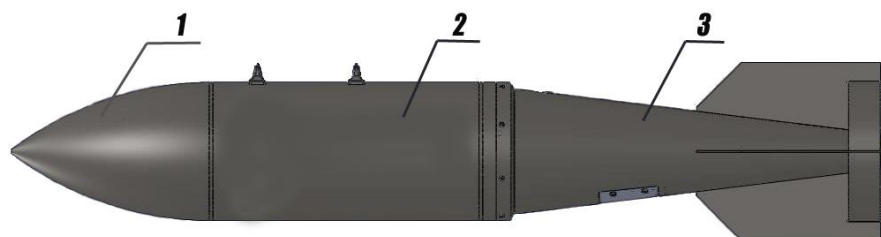


Figure 1. Basic device of BETAB 500
1. Fairing (front part) 2. Cylindrical part 3. Stabilizer


The front part (1) is made of cast steel, which is unnecessarily massive in most cases. Its design and shape can be optimized in order to increase the mass of the warhead and the stability of the ammunition during flight [4, 5].

The destructive action of BETAB is determined by the kinetic energy it possesses when meeting the barrier. The knowledge of the law of movement of the ammunition during its penetration into solid media allows experimental (simulation) studies with new materials for making the fairing of BETAB to be done [5].

2. Description

To solve the problem, it is necessary to be familiar with known physical and mechanical characteristics of metals (table 1).

Table 1. Mechanical Properties of Various Metals

	Properties	Steel	Cast iron	Aluminum
	Plasticity	$\sigma_b=860$	$\sigma_b=420$	$\sigma_b=1200$
	Fragility	$K_u=0,42$	$K_u=0,62$	$K_u=0,50$
	Hardness	HB=360	HB=210	HB=160
	Density	7,8g/sm ³	7,874g/sm ³	2,7g/sm ³

The penetration of aviation ammunition into a solid barrier consists of three stages:

1. impact on the surface of the medium;
2. penetration of the body into the medium;
3. movement of the body in the medium.

The first stage is characterized by the occurrence at the point of impact of a shock wave of contraction, both in the primer and in the body of the ammunition. As a result of the sudden stop when the ammunition meets the barrier, large loads occur.

To solve the task of ammunition penetration in a certain medium, it is necessary to perform an analysis of the deformation caused to the fairing of the aviation ammunition.

The minimal deformation indicates that the fairing is too massive and should be lightened or the material changed in order to optimize the product. For the purpose of the theoretical experiment, a body (simulation model) was constructed with the same dimensions as the "BETAB" product, with different fairings, with a contour thickness of 10 mm (cast iron, steel, aluminum).

The test is carried out at a height $H=2000$ m and a speed $V=40$ m/s of separation from the aircraft of the aviation ammunition, the front part of which is made of the above-mentioned materials.

3. Results

A numerical experiment was conducted simulating the deformation of the airfoil upon impact with the barrier. The deformations of the fairing structures (made of cast iron, steel, aluminum) of the aviation ammunition are shown in fig. 2, 3 and 4.

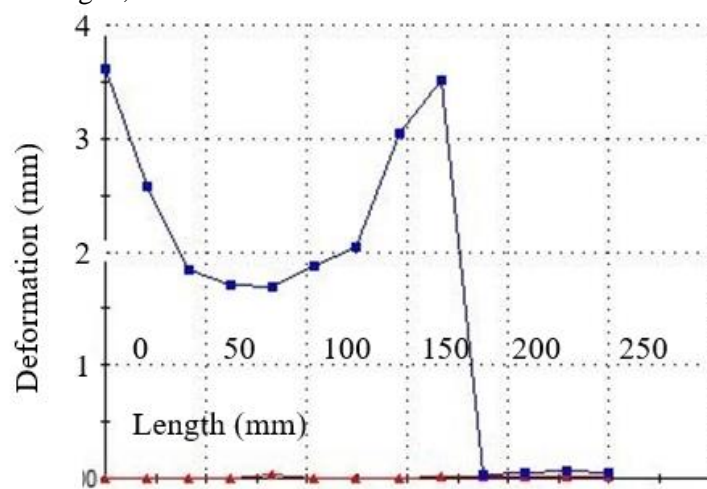


Figure2. Deformation of the Fairing Made of Cast Iron

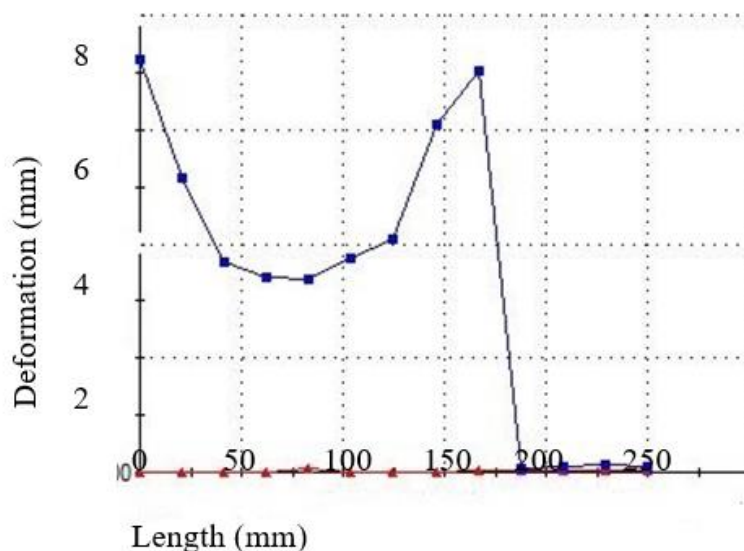


Figure 3. Deformation of the fairing made of steel

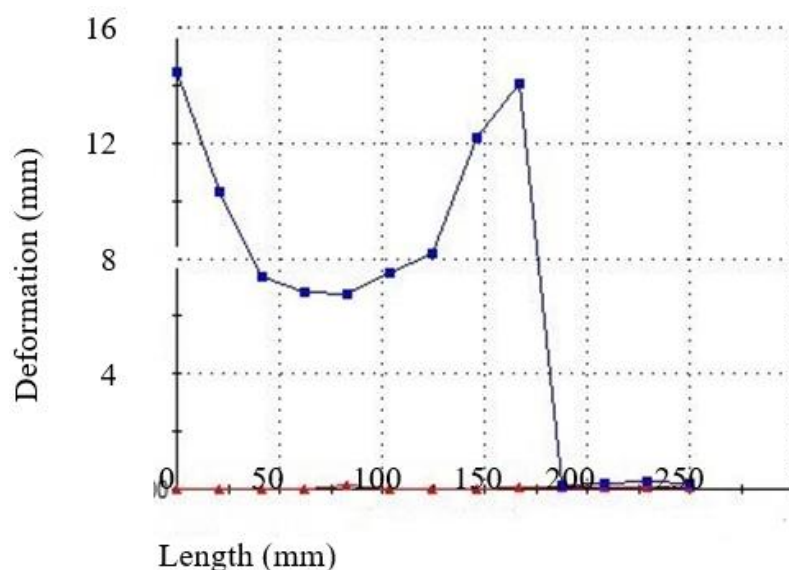


Figure.4. Deformation of the fairing made of aluminum

The figures show the deformations of the fairings of the aviation ammunition along their entire length. At the beginning, a deformation peak is observed due to the impact of the body with the partition. Then there is a drop, because of the modulus of elasticity of the specific materials.

The body of the ammunition is subjected to such deformation that after a certain length, the modulus of elasticity no longer has an effect. Then the material begins to creep and a second deformation peak is reached.

After a certain length, the vibrations from the deformation begin to decrease until they disappear completely.

4. Conclusions

- 1 The conducted research, with different structural calculations, allows the determination of the deformation of the fairing, for new samples of aviation ammunition.
2. The developed simulation makes it possible to lighten the fairing of aviation munitions, at the expense of the shape and amount of payload of the munition, with the aim of its optimization.

Acknowledgments

The research in this article was carried out in fulfillment of Task 1.1.2. "Analysis and evaluation of disaster, accident, emergency and crisis management systems and development of scientifically based proposals for their improvement" by the National Scientific Program "Security and Defense", adopted by RMS No. 731 of 21.10.2021. and according to Agreement No. D01-74/19.05.2022.

References

1. Загорски Н., Асенов Св., Приближени модели за оптимизация на параметрите за експлоатация и техническо обслужване на авиационните системи с оценка на точността и достоверността на получаваните резултати, Journal of the Technical University at Plovdiv "Fundamental Sciences and Applications", Vol. 14(2), 2009, стр. 359-364; Периодично издание, на английски език, ISSN 1314-5258
2. Загорски Н., Сотиров Г., Асенов Св., Анализ на теория на полета на делтапланер за определяне на изисквания и методи за оценка на летателната годност, Fourteenth International Scientific Conference, SPACE ECOLOGY SAFETY SES 2018, Proceedings, стр. 158-166. ISSN 1313-3888
3. Zagorski N., Jordanov D., Tsholakov St., Role of power reserve in parallel hydraulic movements of aircraft controls, Aerospace Research in Bulgaria, 34, 34, Bulgarian Academy of Sciences. Space Research and Technology Institute, 2022, ISSN:p-ISSN 1313 - 0927, DOI:https://doi.org/10.3897/arb.v34.e08, p.p. 95-105.
4. Маринов А., Определяне на силата на челно съпротивление действаща на тяло с оптимална ротационна форма при свръхзвукова скорост, Сборник научни трудове от Юбилейната научна конференция по повод

10 години от създаването на Националния военен университет „Васил Левски“, Том 7, Велико Търново, 2012 г., ISBN 978-954-753-095-9, Стр. 10-142.

5. Покровский Г. И., Сассапарель В. И. и др., Курс авиационных бомб, М., ВВИА 1970 г.

Analysis of the possibilities for the applicability of different types of unmanned aerial vehicles in the crisis management process - building a functional framework for the application of different unmanned aerial vehicles

Stefan Biliderov, Radoslav Chalakov

Air Force Academy, Aviation Faculty, Dolna Mitropolia, Bulgaria, biliderow_ss@yahoo.com,
Rakovski National Defence College. Faculty "Command-Staff", Sofia, Bulgaria, r.chalakov@rndc.bg

Abstract: While the role of unmanned aerial vehicles (UAVs) continues to grow in all sectors of society, new applications for drones in security and defense continue to emerge. Although the capabilities provided by drones in the theater of war have already been explored, more research is now being undertaken into their potential to improve security.

Keywords: Unmanned aerial vehicles (UAVs), Unmanned aerial platforms (UAVs), crisis management

Introduction to the problem

The European Commission has already recognized the potential of unmanned aerial vehicles in security and defense and is working with the European Aviation Safety Agency (EASA) to help gather more information and better understand how these powerful devices can prove useful in addressing the security challenges of the future.

How are the devices used in the defense and security sector? What advantages do they have over other technologies?

Currently, it is still quite early for UAVs to be fully implemented and therefore their use in security is quite limited at this point. From the classification of crises and the combination presented in the report "**Analysis of the possibilities of the applicability of different types of UAV in the crisis management process - the signs and criteria for classifying crises**" it is possible to determine the necessary means based on the analysis of their possibilities.

Types of UAVs used in the crisis management process

Modern Unmanned platforms (UPL) are used in two major directions. The first is related to satisfying certain amateur goals, and the second is the professional direction. In both directions, the development of UPL uses the professional skills of teams of specialists in construction, engines, equipment, automatic control and payload management.

The advantages of UPL, which make them more attractive than manned aviation are [6]:

- small mass and dimensions of the UAVs, which results in great economy and duration of the flight;
- low production cost and low cost of operation;
- multifunctionality of use depending on the type of equipment installed and the missions and tasks performed;
- real-time aerial reconnaissance and surveillance capability;
- lack of technical and psychophysiological limitations when using them in complex and dangerous conditions;
- wide range of tasks performed in peacetime, crisis and war at strategic, operational and tactical levels.

Despite the obvious advantages of UAVs, they are not without a number of disadvantages:

- less adaptability than manned aviation in the event of a sudden change of tasks and missions during their execution;
- unsolved problems in providing secure communication channels between the UAV and the control center;
- transmission of information with distortion;

- possible reuse issues after landing and rescuing the UAVs;
- lower level of reliability compared to manned aviation;
- insufficient multiplicity of use of UAVs, etc.

The drawbacks listed in this way are evidence that UAVs are applicable in solving a very wide range of tasks of various nature which can be defined as:

- various types of security, control and surveillance;
- search and assessment in areas of disasters, accidents and environmental catastrophes;
- monitoring of forests, agricultural crops and crops, surveying activities;
- mapping and surveying;
- fast updating of topographical information in populated areas.

The purpose and use of UPL for various purposes, at the current stage of the development of the technology, has no visible limits. However, quite conditionally these purposes, depending on the tasks that are performed, can be divided into two tasks for civil purposes and tasks related to security and defense.

It is very important in the process of choosing an UPL to make a selection between the different construction schemes which are the airplane and helicopter (copter) schemes. The choice between aircraft and helicopter schemes depends on the application of the unmanned system. In order to make this choice, it is necessary to make a comparative analysis of the advantages and disadvantages of UAV systems using an airplane or a helicopter.

UAV aircraft scheme - Advantages are: greater relative load capacity compared to the helicopter; longer flight duration compared to a helicopter with a similar take-off weight; greater radius of action compared to a helicopter with a similar take-off weight.

UAV aircraft scheme - Disadvantages are: the need for a dedicated runway; need for additional devices for shortening the take-off run when the aerodrome length is insufficient – catapults, launch accelerators, springboards, etc.; the need for additional devices to shorten the landing distance when the aerodrome length is insufficient - traps, airbags, parachutes, etc.; limitation on minimum possible flight speed; significantly lower maneuverability in a horizontal plane compared to that of a helicopter .

UAVs according to the helicopter (copter) scheme - Advantages are: take-off and landing from limited-sized and (or) hard-to-reach sites, operation from urbanized areas; range of flight speeds from V_{\max} to 0, hovering over certain points of the route; higher maneuverability in a horizontal plane, with a turning radius tending to zero; possibility of safe landing in autorotation mode.

UAVs according to the helicopter (copter) scheme - Disadvantages are: a shorter flight duration compared to an aircraft with a similar take-off weight; smaller radius of action compared to an aircraft with a similar take-off weight; lower relative load capacity compared to the aircraft.

In the market, autonomous unmanned helicopters (UAHs) or autonomous unmanned copters (AUCs) are increasingly preferred over unmanned aerial vehicles (UAVs). This is understandable from a number of physical advantages of helicopters over airplanes, such as: no need to provide a runway; possibility of hovering over a specific point of the terrain; possibility of quick maneuvers, etc.

There are significant advantages of autonomous drones (AD) over other UAVs. They are expressed in [1]:

- highly integrated hardware and software platform for fully autonomous flights;
- integrated control method including: autonomous take-off and landing; automatic tracking of the flight path; automatic tracking of set and detected targets;
- built-in functionality, which includes: automatic execution of tasks based on a pre-planned flight path; high level of knowledge representation with reasoning; diagnostic and monitoring system and chronological recognition system;
- hybrid software architecture and integrated control support system;
- sensor platform for integrated perception, which includes: an image processing system and techniques for combining information from different sensors;
- integration of AD into the C4ISR infrastructure using a cooperative multi-agent framework.

From the resulting analysis and comparisons, 4 types of platforms can be determined with the possibility of use in the combination of the manifestation of the crises:

- airplane;
- helicopter;

- copter;
- combined (hybrid) scheme.

With **the airplanes platforms** different types of combinations are available. Depending on the number of engines, a total of 5 (five) combinations can be classified - single-screw; twin screw; four-screw ; six-screw ; eight-screw.

Looking at them depending on the type of engine, a total of 2 (two) types can be defined - LPG and electric.

Based on the number of wings, a total of 3 (three) types will be classified - monoplanes; duplexes; triplanes.

According to the wing profile, airplanes can be divided into 3 (three) types - with a straight aerodynamic profile; with a flat profile; with an inverted airfoil.

A total of 3 (three) types can be determined depending on the sweep of the wing, with a straight sweep; without bowing; with reverse sweep.

Based on the V shape of the wing, there are 3 (three) types - with a straight V shape; without the V shape; with an inverted V shape.

Depending on the position of the tailplanes, there are a total of 3 (three) types - high; mid-positioned; low lying.

The **helicopter platforms** can be divided into a total of 6 (six) types.

- single screw circuit;
- longitudinal diagram;
- cross section;
- coaxial circuit;
- cross propeller scheme;
- with reactive bearing screw.

With **the copters platforms** are available different types of combinations, which can be divided into a total of 4 (four) types:

- three times (3 times);
- four times (4 times);
- hexacopter (6 floods);
- octocopter (8 floods).

In the case of hybrid schemes, in addition to the full combination of aircraft and copter schemes (28 in total), the following are also added:

- autogyro;
- rotorcraft;
- with the tilt of the rotors;
- vertical takeoff aircraft schematic.

Which brings the total number of combinations to **32** types.

Table 1: UAV platforms

UAV platforms	airplane	helicopter	copter	hybrid
options (C)	22	6	4	32

Each of the described types has its operational capabilities. Accordingly, the population represents the set $n = \sum_1^n B = 64$, which means that $n = 64$ possible UAV designs. The sample size $k = 4$ UAV classification criteria and features. Then, each non-return unordered sample of volume k from the population of volume n represents the combination:

$$(1) \quad C_n^k = \frac{n!}{k!(n-k)!} = 635\,376$$

Combinations of expression (1) from the material cited in the introduction are opposed by combinations of expression (1). If we divide expression (1) by expression (1) from the present development, we get:

$$(2)$$

$$(2) \quad Nub = \frac{Nub_{crisys}}{Nub_{UAVs}} = 256,56$$

Expression (2) shows that 256,56 crisis manifestations (Nub) can be countered by only one unmanned platform. The goal of the work is ultimately to develop a suitable hardware and software platform for fully autonomous flight, applicable to a wide range of tasks, covering low and high autonomous functionality in the form of control and artificial intelligence.

Building a functional framework for the application of different UAV in different types of crises

From the expressions (1) (the previous material), (1) and (2) (the present material) it can be seen that it is not possible to unilaterally determine the technological means (UAV) that cover the entire range of possible manifestations of the crises. In this case, it is necessary to model the decision-making process for the application of a specific UAV in an emerging crisis.

In this case, the IDF0 functional modeling framework comes to the rescue. The idea of IDF0 is a methodology for functional modeling of some system. It is shown in Fig.1.

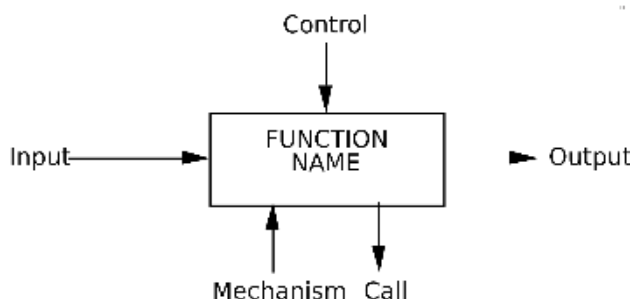


Figure 1 Principles of functional system modeling.

The IDEF0 model shown in Fig.1 is based on a simple syntax. Each activity is described by a boxed verb-based label. Inputs are shown as arrows entering the left side of the activity box, while output is shown as arrows exiting the right side of the box. Controls are shown as arrows entering the top of the box, and mechanisms are shown as arrows entering the bottom of the box. Inputs, Controls, Outputs and Mechanisms (ICOM) are called concepts [2].

IDEF0 is a functional modeling methodology and graphical notation designed to formalize and describe business processes. A distinctive feature of IDEF0 is its emphasis on object subordination. IDEF0 discusses logical relationships between works, not their temporal sequence (workflow). The description resembles a "black box" with inputs, outputs, controls and a mechanism that is gradually detailed to the required level. Also, to be properly understood, there are dictionaries describing activities and arrows. It also shows any control signals that have not been shown on the DFD (Data Flow Diagram). This model is used in the organization of business processes and projects based on the modeling of all processes: both administrative and organizational [3], [4].

Describing through IDEF0 the process of the applicability of different types of UAV in the crisis management process, the diagram shown in Fig.2 is constructed.

The analysis of the functional framework (Fig. 2) for the application of different UAV in different types of crises leads to the conclusion that the process is extremely complex and voluminous. This is also the reason that here in the developed material the functionality is considered only up to level A0. On this basis, the research is to be continued at level A1, A2, etc., and it is necessary to establish the depth that can be reached.

NEWNS - National Early Warning and Notification System
ESD - End State Desired

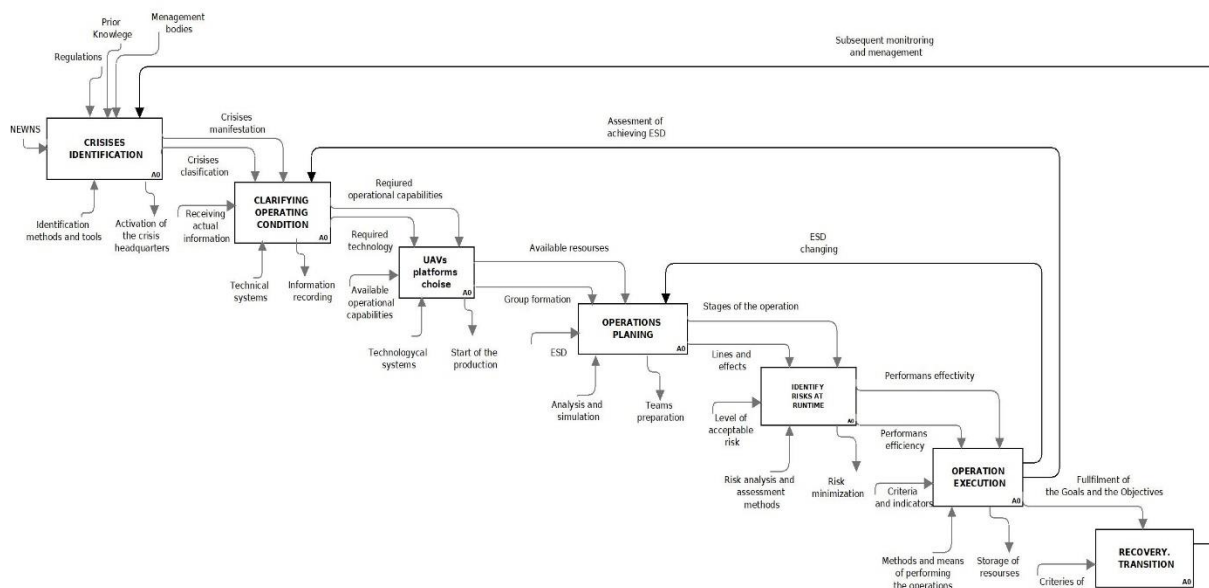


Figure 2 Functional diagram of the application of UAV in the crisis management process

Another possible modeling approach is Petri Nets, but in this case the functional modeling method according to the IDEF0 standard was chosen. The process begins with "Crisis Identification", which is carried out with the help of the National Crisis Management System, which includes a Unified National Monitoring, Early Warning and Disclosure System (NEMS). This is where the Crisis Staff comes into play. It is possible to use different forecasting methods based on past and current information about the manifestations of crises. This makes it possible to use a knowledge base on which to base a developed expert system through various quantitative and qualitative methods [1].

The Crisis Staff conducts an "Operational Conditions Clarification" using the comprehensive approach to assess all factors. Here the impact of the various manifestations of the crisis on the general operational situation is established. It is possible to present the data with diagrams. They are particularly suitable when visualizing a large amount of information and supporting the decision-making process. The following chart types are available [4]:

- Reflective influences;
- Reflecting causes and effects;
- Reconstructive processes in time;
- Information flow processes;
- Organizational;
- Decision tree;
- Diagrams of Ven.

Based on the assessed crisis manifestations and the need for specific operational capabilities provided by the currently available technology, a decision is made to use an appropriate UAV platform. Here, for the respective platform, it is necessary to perform an automated analysis, which in economics is called "Cost and Profit Volume Analysis", "Operational Analysis" or CVP Analysis [5].

CVP analysis is better to be done beforehand. This type of analysis is used in the strategic planning of an organization's activities. Other types of tools that may be used to determine the appropriate UAV platform for a particular manifestation of the signs of a given crisis and related to the available resource are:

- deterministic factor modeling;
- factor analysis methods;
- ABC analysis;
- SWOT analysis;
- and others.

Operational analysis aims to identify the dependence of the financial results of a given action, enterprises, firm, structure or organization on the volume and costs of sales (sales). The ratio (cost \rightarrow volume \rightarrow profit) is used for it. Therefore, it is possible to determine the interrelationships between existing costs and income (benefits) for different volumes of production (or purchase of UAV). Operational analysis aims to find the most useful combination of variables. This approach is considered one of the most effective means of planning and forecasting the activity of the company (organization). It should be noted that operational analysis and cost management include not only the calculation of coefficients, but also their correct interpretation. This means that it is necessary to draw conclusions that will improve the situation in the future. Strategic and tactical decisions need to be made wisely and carefully. Operational analysis allows obtaining a wide range of indicators, based on which it is possible to effectively influence the final work of the company (structure). Among them should be noted [5]:

- The most profitable from the point of view of the execution of the assortment with a limited number of resources.
- Even sales (realizations).
- The minimum selling price (on the UAV exit platform).
- Possibility of reducing prices when increasing the volume of sales (realizations).
- The ability to see how structural changes in scope affect enterprise profitability (added value to security).
- Solving problems of the type of purchase / production of parts and / or semi-finished products.

Also, the use of operational analysis makes it possible to estimate the minimum order values (the manufacture of UAV platforms) that should be taken in the presence of certain circumstances. It is always necessary to look for the Margin of Safety through risk assessment in each of the activities related to the development, use and disposal of UAVs. In this way, the process of "Platform Selection with UAVs" is carried out and an answer is given, whether it is necessary to build structures to support a certain operational reserve of UAVs, to produce UAVs (with certain operational capabilities) after the crisis identification stage or to switch to a combination of the two. Possible tools at this stage, supporting explicit decision-making, are divided into two large groups: quantitative and qualitative evaluation methods. They are united by the subject area of multivariate analysis.

Then, the "Operation Planning" stage begins. Here operational analysis is developed to support the decision making process. This term means decomposition of activities and insight into the process itself [6]. The main purpose of operational analysis is to support decision-making through the use of modeling and simulations, optimization, logical, mathematical, statistical and empirical methods and techniques as analytical tools. Operational analysis supports the activities related to the development of concepts and conducting experiments throughout the entire period - from planning to implementation and evaluation of their results [7]. In Fig. 3 is shown the iterative relationship in the decision-making process. [6]

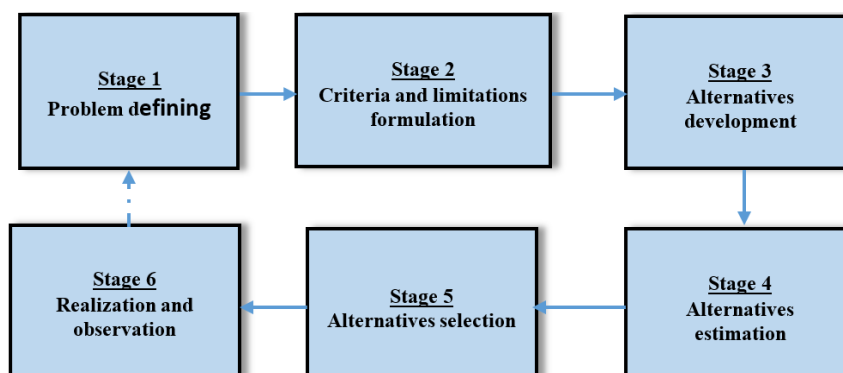


Figure 3 Functional block diagram of the decision making process

It can be seen that through this functional flow chart, all stages in the operation planning for the application of UAVs in the crisis management process are covered. Based on the information model of Fig. 2 in the operational analysis, a tree structure is obtained, which affects all the activities included in

this analysis. This is one of the syntax structures of the IDF0 from Fig. 1. Fork at which an IDEF0 arrow segment (passing from source to use) splits into two or more arrow segments. Fig.4 shows such a branch.

In addition, it is possible to use the methods of multi-criteria analysis to support the implicit decision-making process. Through this analysis, objects or situations are evaluated according to multiple mutually exclusive (contradictory) criteria. Quite often, multi-criteria decision-making is used when opposing two mutually exclusive criteria - price and quality.

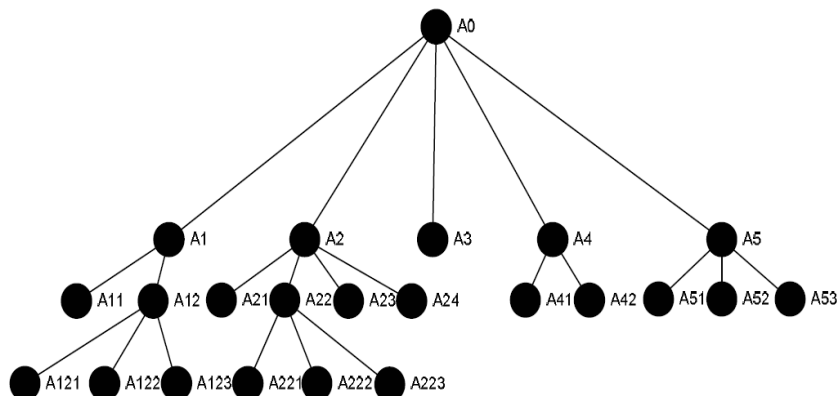


Figure 4 Tree of nodes in operational analysis

The research in this material goes only to the A0 level, as shown in Fig. 2. To continue with the decomposition down the tree (Fig.4) additional research is needed, which goes beyond the set goal in the development. Risk management is necessary at every stage, but here the focus is entirely on "Identifying the risks for the specific conditions". The IDF0 framework is also suitable for describing risk management processes [8].

The identification of risks is actually due to a detailed analysis of the objectives, which are based on the strategies adopted for action in the crisis management process and represent its general documented plans. Any uncertainty associated with this process must be recognized, categorized and described. Risk can be caused by both internal and external factors. Individual risks can be the result of both external and internal factors [9]. The growing uncertainty in the manifestation of crises necessitates the use of specific risk management models. One such risk management model is presented in [10].

In this case, the IDF0 framework presents the main activities of the risk management process, including the following content:

- Initiating the process;
- Defining the environment;
- Identification of risks;
- Risk analysis;
- Risk Assessment;
- Counteraction to risk
- Monitoring and tracking of the risk management process.

The decomposition of the activities according to this framework gives the full functionality of the stages in the management of this process. It is possible to determine the values of the risk elements using:

- knowledge from historical data – quantitative risk analysis methods are used;
- expertise – qualitative methods implemented by coding with numbers or modeled with known functions from the fuzzy sets.

After determining the elements of risk, the rule base is drawn up, having the form: "If the exposure to event A is k_1 , and its probability of occurrence is k_2 , then the consequences are (usually) k_3 ." The derived rules generate the mathematical dependence of the output value on the input data, in this case the consequence of the risk [10]. These are mathematical models for risk assessment based on intelligent technologies, which can be modeled with specialized means based on fuzzy logic, taking into account the incomplete determination in quantitative and qualitative data.

After the planning of the operation and assessment of the possible risks related to the operational situation, the "Execution of the operation" stage is triggered by appropriately selected and used UAVs. From the analysis of the application of UAVs, it is established that at this stage there are no restrictions on their use. In order not to waste a resource, it is necessary that the UAV mission is related to the specific operational situation. In the Crisis Headquarters, the implementation of the effects and activities along the operational lines is monitored, using the structure and composition of the National Monitoring, Early Warning and Disclosure System (NSNRPO), insofar as the National Crisis Management System is linked to it. There is still a regulatory gap here.

In this way, the crisis management process is carried out, where a number of specific features of this process are embodied in the OODA cycle (Observation - Orientation - Decision - Action). Assessment of reaching the desired end state (DES) is done in Crisis Headquarters, which has the authority to decide to move to the last stage of Fig. 2 – Recovery and Transition. It is possible that in the process of managing the crisis, the conditions will change, which will also lead to a change of the HCS and the mission, depending on the current operational conditions and capabilities. Here, the Crisis Staff is responsible for Initiating change and planning according to the changes that have occurred with a change in the mission of the UAV (if necessary).

In the event of problematic inconsistencies that affect the lines of operation, it is necessary to establish the root cause. A powerful tool in this direction is the Kepner-Tregoe analysis. Although Root Cause Analysis (RCA) itself is a reactive tool, but when properly and correctly conducted, it is preventive in nature. Other similar methods are: the bowtie method and the method of analysis of the variants of errors and their effect (FMEA).

In root cause mapping, the 5 Whys principles and tree are commonly used; the Ishikawa (Fishbone) method; 6 sigma; process map. A logical tree is built to determine the root cause, models of the event's manifestation are created and Hypotheses (informed assumptions) are built on their basis.

After that, it is necessary to test the built Hypotheses, for which the 6 sigma method or the Lean method is suitable. When it is necessary to evaluate the effect of the failure of an action on the line of operations, it is possible to use the method - Analysis of failures and their effect (FMEA). This method is used in two directions: for a process problem and for a technique problem. It involves the analysis and prioritization of process or technique failures.

After reaching the HCS and assessing the operational situation, proceed to Restoring stability and Transition. The system is preparing to perform its functions in anticipation of the next crisis.

Conclusion

Unmanned aerial vehicles are already used in everyday life as tools that are applied to survey infrastructure for the purpose of improving safety, monitoring, collecting scientific research data, etc. In the article, an analysis of the types of platforms used in UAVs was performed, and the combinations were calculated with the return of the possible configurations. Based on the obtained results, a functional model of the process of selecting a specific UAV was developed depending on the manifestations of the crisis and the current operational conditions, where work is limited to A0 level of the model. Further development is the subject of other publications and is beyond the scope of this material.

The research in this publication was carried out in fulfillment of Task 3.1.9. "Construction of a network of autonomous low-powered flying devices (quadrocopters) for control of an urbanized area" by the National Scientific Program "Security and Defense", adopted by RMS No. 731 of 21.10.2021. and according to Agreement No. D01-74/19.05.2022.

Literature

1. Nikolina Toncheva Anton Nedyalkov PRODUCTION AND OPERATIONS MANAGEMENT, Ruse, 2002
2. Varun Grover, William J. Kettinger . Process Think: Winning Perspectives for Business Change in the Information Age, 2000
3. Veis Šerifi1, Predrag Dašić , Ratimir Ječmenica1, Dragana Labović . Functional and Information Modeling of Production Using IDEF Methods, Strojniški vestnik - Journal of Mechanical Engineering 55(2009)2
4. Announcing the Standard for INTEGRATION DEFINITION FOR FUNCTION MODELING (IDEF0). Draft Federal Information Processing Standards Publication 183, 1993 December 21

5. Operational analysis like element on management on expenses . CVP analysis . Point on equilibrium .
<https://bg.stuklopechat.com/novosti-i-obschestvo/75611-operacionnyy-analiz-kak-element-upravleniya-zatratami-cvp-analiz-tochka-bezubytochnosti.html>
6. A. Lazarov, Hristov N., Radulov I., Andreeva P. Operational analysis. Implementation guide. Sofia 2008
7. Hristov, N. Architectural approach in defense. - Sofia: MO, 2013.
8. Hui-Ping Tserng , I-Cheng Cho, Chun-Hung Chen, Yu-Fan Liu. Developing a Risk Management Process for Infrastructure Projects Using IDEF0. Sustainability 2021, 13, 6958.
<https://doi.org/10.3390/su13126958>
9. Vasil Bozhkov. On the risk assessment process as part of understanding internal control (part two).
AUDIT , no . 03/2020, year XXIV
10. A model for risk management in defense and armed forces planning . city _ Sofia , 2011

Hohmann Orbit Transfer Analysis

Assen Angelov Marinov

Bulgarian Air Force Academy, Faculty of Aviation, asen_aerodynamics@abv.bg

Abstract: The Air Force cannot have a modern and sufficient capability to react quickly to potentially major threats if it does not also develop the space segment. The article considers transfer from a base orbit to a medium Earth orbit of satellite.

Keywords: *Air Force, Hohmann transfer, satellite orbit.*

1. Introduction

Space provides opportunities that can't be realized from the altitudes at which modern aircraft fly. Artificial satellites have the ability to observe much larger areas on Earth. In addition to enabling large-scale observation of the Earth's surface and atmosphere, satellites also provide communication. Space, at the current level of technology, is better suited for the transfer of electromagnetic signals compared to activities that involve carrying loads of large mass. As a result, space basing is best suited when there is a need for:

- large-scale atmospheric monitoring;
- global communication and data transfer;
- the precise location of objects of interest;
- large-scale intelligence;
- missile launch detection to provide early warning of a possible attack.

Some of these tasks can be performed regionally, in an emergency, and by aircraft, but they cannot yet stay in the air for years.

This shows us that the Air Force cannot have a modern and sufficient capability to react quickly to potentially major threats if it does not also develop the space segment.

At this stage, space basing is not economically viable for deploying weapons, as this mission can be performed very well from the ground, at a much lower cost. At this stage, intercontinental range ballistic missiles have a rapid and global effect, and are significantly cheaper in terms of cost than eventual space-based weapons.

However, large-scale reconnaissance, detection and early warning of a possible attack cannot be carried out quickly enough in the current environment and capabilities of ground-based weapon systems without the presence of an indigenous satellite system.

This requires the Air Force to build the human and technical capability to operate these satellite systems.

The speed of satellites is not arbitrary; it is determined by their orbit and is closely related to altitude. Satellites in low earth orbits (low orbits are hundreds of kilometers above the earth) move rapidly relative to the earth. They can make a single orbit of 1.5 to 2 hours. Satellites in higher orbits move at slower speeds, and the distance they travel in one orbit is longer [2]. Unlike aircraft, once in orbit, a satellite does not need constant power to stay in flight. Maneuvering in space is accomplished with small onboard engines.

However, all these activities would involve considerable maneuvering in space, which is usually accompanied by the consumption of a large amount of fuel. For this reason, the orbits of these objects have to be very accurately specified at the design stage of the orbit concerned.

What has been said so far shows the crucial place of orbital dynamics development in the Air Force space segment.

Orbital dynamics (also called orbital mechanics or astrodynamics) studies the motion of rockets and satellites in orbit and solves practical problems of maneuvering and controlling the orbit of these vehicles [4].

Maneuvering in Earth orbit serves to the following purposes:

- moving from one orbit to another;
- fine-tuning and maintenance of an orbit already reached (even though the satellites are in orbit, it may be slightly perturbed, say by the Moon and Sun), requiring them to be fine-tuned;
- performing a docking between two satellites (e.g. ISS and Cargo mission);
- forced deorbiting to avoid the accumulation of space debris, since in low Earth orbit, satellites deorbit to enter the atmosphere and burn up;
- sending the satellite into a so-called "graveyard" orbit (for geostationary satellites, because they are very far away it is difficult to move them to the ground to burn up, so they are sent into a higher orbit called a "graveyard" in which inactive satellites move).

One of the basic maneuvers used in orbital analysis and orbital design is the Hohmann Transfer, which is used to move from one orbit (at one altitude) to another orbit (at another altitude).

2. Hohmann transfer

In the coplanar Hohmann transfer, both velocity pulses are confined to the orbital planes of the initial and final orbits. For the Hohmann maneuver from an orbit of lesser height to a circular orbit of greater height, the first pulse creates an elliptical transfer orbit with a perigee height equal to the height of the initial circular orbit and an apogee height equal to the height of the final orbit. The second pulse rotates the transfer orbit at apogee. Both pulses are posigrade, meaning they are in the direction of the orbital motion [1, 3].

$$\begin{aligned} R_i &= R_e + H_i \\ R_f &= R_e + H_f, \end{aligned} \quad (1)$$

where:

R_i – initial geocentric radius;

R_f - radius of the final circular;

H_i - initial orbit altitude;

H_f - final orbit altitude.

The difference between the speed on the initial orbit and the perigee speed of the transfer orbit is:

$$\Delta V_{mfi} = V_{cl} \sqrt{1 + \left(\frac{\sqrt{\frac{2R_f}{R_i + R_f}}}{\sqrt{\frac{2R_f}{R_i + R_f}}} \right)^2 - 2 \sqrt{\frac{2R_f}{R_i + R_f}}}, \quad (2)$$

where:

ΔV_{mfi} - magnitude of the first impulse;

V_{cl} – circular local velocity.

$$V_{cl} = \sqrt{\frac{G}{R_i}}, \quad (3)$$

where:

G - gravitational constant of the central body.

The difference between the speed on the final orbit and the apogee speed of the transfer ellipse is:

$$\Delta V_{msi} = V_{cl} \sqrt{\left(\frac{\sqrt{\frac{R_i}{R_f}}}{\sqrt{\frac{R_i}{R_f}}} \right)^2 + \left(\frac{\sqrt{\frac{R_i}{R_f}}}{\sqrt{\frac{R_i}{R_f}}} \right)^2 \left(\frac{\sqrt{\frac{2R_i}{R_i + R_f}}}{\sqrt{\frac{2R_i}{R_i + R_f}}} \right)^2 - 2 \left(\frac{\sqrt{\frac{R_i}{R_f}}}{\sqrt{\frac{R_i}{R_f}}} \right)^2 \sqrt{\frac{2R_i}{R_i + R_f}}}, \quad (4)$$

where:

ΔV_{msi} - magnitude of the second impulse.

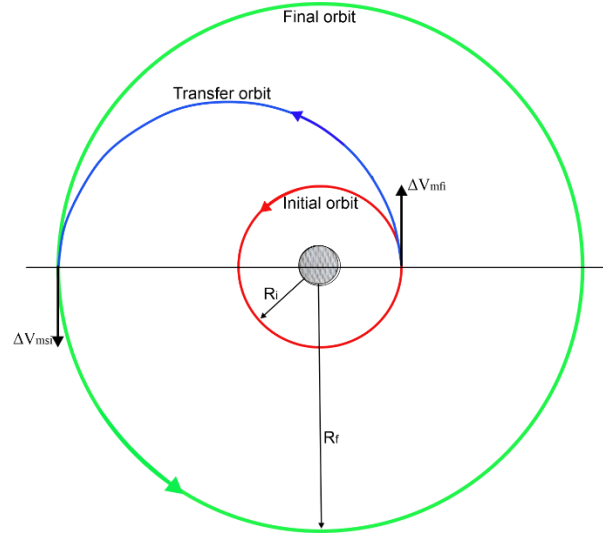


Fig. 1. Geometry of coplanar Hohmann transfer

Hohmann transfer allows orbital transfer between two circular orbits which have different orbital inclinations.

$$\Delta V_{mfi} = V_{cl} \sqrt{1 + \left(\frac{2R_f}{R_i + R_f} \right)^2 - 2 \frac{2R_f}{R_i + R_f} \cos \theta_{fi}}, \quad (5)$$

where:

$\cos \theta_{fi}$ - plane change from the first impulse.

$$\Delta V_{msi} = V_{cl} \sqrt{\left(\frac{R_i}{R_f} \right)^2 + \left(\frac{R_i}{R_f} \right)^2 \left(\frac{2R_i}{R_i + R_f} \right)^2 - 2 \left(\frac{R_i}{R_f} \right)^2 \frac{2R_i}{R_i + R_f} \cos \theta_{si}}, \quad (6)$$

where:

$\cos \theta_{si}$ - plane change from the second impulse.

The relationship between the plane change angles is:

$$\theta_t = \theta_{fi} + \theta_{si} \quad (7)$$

The total magnitude of the impulse ΔV_t required for the maneuver is the sum of the two impulses:

$$\Delta V_t = \Delta V_{mfi} + \Delta V_{msi} \quad (8)$$

3. Numerical Solution

Basic manoeuvres used in orbital analysis and orbital design are:

- Hohmann transfer;
- Bielliptic transfer;
- Phase transfer;
- Change of orbital inclination.

Knowing these four types of manoeuvres we can control any orbit in Earth space.

The purpose of this study is, given an initial orbit and inclination and a desired final orbit and inclination, to determine:

- initial radius of the orbit;
- initial velocity of the orbit;
- magnitude of the first impulse;

- final orbit radius of the orbit;
- final orbit velocity of the orbit;
- magnitude of the second impulse;
- total magnitude of the impulse;
- first inclination change;
- second inclination change;
- total inclination change
- transfer orbit semimajor axis;
- transfer orbit eccentricity;
- transfer orbit inclination;
- transfer orbit perigee velocity;
- transfer orbit apogee velocity;
- transfer orbit coast time.

Optimizing the non-coplanar Hohmann transfer can determine by solving for the root of a derivative:

$$\frac{\partial \Delta V_t}{\partial \theta_{fi}} = \frac{\left(\sqrt{\frac{2R_f}{R_i + R_f}} \right) \sin \theta_{fi}}{\sqrt{1 + \left(\sqrt{\frac{2R_f}{R_i + R_f}} \right)^2 - 2 \left(\sqrt{\frac{2R_f}{R_i + R_f}} \right) \cos \theta_{fi}}} - \frac{\left(\sqrt{\frac{R_i}{R_f}} \right)^2 \left(\sqrt{\frac{2R_i}{R_i + R_f}} \right) (\sin \theta_t \cos \theta_{fi} - \cos \theta_t \sin \theta_{fi})}{\sqrt{\left(\sqrt{\frac{R_i}{R_f}} \right)^2 + \left(\sqrt{\frac{R_i}{R_f}} \right)^2 \left(\sqrt{\frac{2R_i}{R_i + R_f}} \right)^2 - 2 \left(\sqrt{\frac{R_i}{R_f}} \right)^2 \left(\sqrt{\frac{2R_i}{R_i + R_f}} \right) \cos(\theta_t - \theta_{fi})}}. \quad (9)$$

Results from Hohmann orbit transfer calculation

Source data:

- 1) initial orbit altitude - 200.0000 km;
- 2) final orbit altitude - 20200.0000 km;
- 3) initial orbit inclination – 35°;
- 4) final orbit inclination – 63.4°.

Results

- 1) initial orbit radius - 6578.1363 km;
- 2) initial orbit velocity - 7784.2621 m/s;
- 3) ΔV_{mfi} - 2131.0544 m/s;
- 4) first inclination change - 3.2595°;
- 5) final orbit radius - 26578.1363 km;
- 6) final orbit velocity - 3872.6355 m/s;
- 7) ΔV_{msi} - 1960.5885 m/s;
- 8) second inclination change - 25.1405°;
- 9) total inclination change - 28.4000°;

- 10) ΔV_t - 4091.6428 m/s;
- 11) transfer orbit semi-major axis - 16578.1363 km;
- 12) transfer orbit eccentricity - 0.6032;
- 13) transfer orbit inclination - 38.2595° ;
- 14) transfer orbit perigee velocity - 9856.2534 m/s;
- 15) transfer orbit apogee velocity - 2439.4404 m/s;
- 16) transfer orbit coast time - 10621.4680 s.

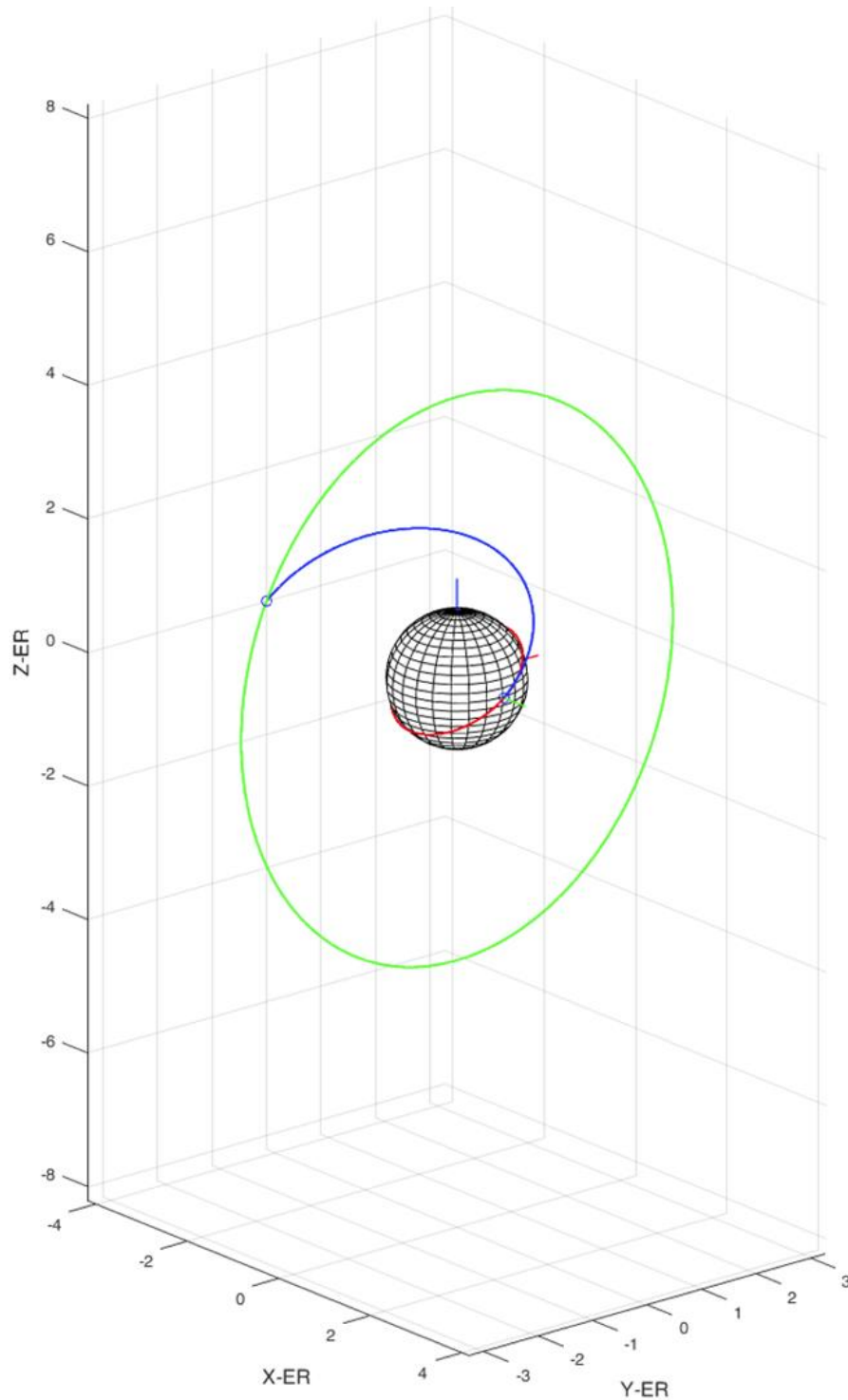


Fig.2. Hohmann orbit transfer

4. Conclusion

The example presented is a typical example of a transfer from a base orbit to a medium Earth orbit, because higher orbit satellites are almost always placed in a low orbit by the launch vehicle and use their rocket engines to reach their target orbit.

The most common application of satellites in such an orbit is positioning systems, such as the Global Positioning System – 20200 km.

Satellites in low-Earth orbit have little signal delay compared to those in higher orbit. Their disadvantage is the relatively high radial velocity of the satellite, which requires a larger number of ground tracking stations to be used to ensure constant communication. Most scientific satellites and many weather satellites are in a nearly circular, low Earth orbit. The satellite's inclination depends on what the satellite was launched to monitor.

Two mean Earth orbits are notable: the semi-synchronous orbit and the Molniya orbit. A semi-synchronous orbit is a nearly circular orbit (about 20,200 kilometers above the surface). A satellite at this altitude takes 12 hours to complete one orbit. As the satellite moves, the Earth rotates beneath it. For 24 hours, the satellite crosses the same two points on the equator every day. This is the orbit used by the Global Positioning System (GPS) satellites.

The second common mean Earth orbit Molniya works well for observing high latitudes.

References

1. Jezewski D., Lyndon B., Primer Vector Theory and Applications, Space Center Houston, NASA Technical Report.
2. Onoda M., Young. O., Satellite Earth Observations and Their Impact on Society and Policy, Japan Aerospace Exploration Agency, 2017.
3. Wright D., Grego L., Gronlund L., The Physics of Space Security, NASA, 2005.
4. Wilmer M., Military Applications of High-Altitude Satellite Orbits, Department of the Air Force, 2016.

Hohmann transfer in polar orbits

Assen Angelov Marinov

Bulgarian Air Force Academy, Faculty of Aviation, asen_aerodynamics@abv.bg

Abstract: The Air Force cannot have a modern and sufficient capability to react quickly to potentially major threats if it does not also develop the space segment. The article considers transfer in low polar Earth orbit of satellite.

Keywords: *Hohmann transfer, polar orbit, satellite orbit.*

2. Introduction

It is often necessary to visualize the orbit of a satellite relative to points on Earth. For example, there may be a need to know when a remote sensing spacecraft will be over an area of national security interest.

This paper will consider the placement of classical orbital elements. These elements assist in the visualization and analysis of orbits in space. They assist in determining ground tracks to identify when certain parts of the Earth cross into the spacecraft's field of view.

The orbit inclination angle (i) can be between 0° and 180° . When the inclination angle is less than 90° , the orbit is prograde (fig. 1 c), and when it is greater than 90° , the orbit is retrograde (fig. 1 d).

When the inclination angle is 90° , the orbit is polar (Fig. 1 b). It is sometimes assumed that when the inclination angle is between 80° and 100° , the orbit is strictly polar.

If the inclination angle is 0° or 180° , the orbit is equatorial (fig. 1 a), and when it is less than 10° , it is nearly equatorial.

Some satellites have an inclination between 60° and 90° . This means that they possess a polar orbit, and when the inclination is 90° the orbit is strictly polar. Strictly polar orbits are commonly used by satellites studying remote regions of the Earth's environment, military satellites (the first military navigation systems), geodetic satellites, etc.

Hence, the value of the inclination is used to distinguish two main classes of orbits. When $0^\circ < i < 90^\circ$, the satellite moves with the Earth's rotation (in the eastward direction), and the satellite is in a direct orbit or prograde orbit (the satellite orbits in a direction coincident with the Earth's rotation direction) (fig. 1 c). If $90^\circ < i < 180^\circ$, the satellite is moving in the direction opposite to the earth's rotation (westward), so it is in an indirect orbit or retrograde orbit (the satellite orbits in the direction opposite to the earth) (fig. 1 d).

Some of the first satellites were launched as early as 1967 - Aurora-1 ($h = 3\,850$ km) and OV3-6 ($h = 420$ km). In 1975, Explorer-54 or AE-D, $h_p = 151$ km and $h_a = 3\,819$ km were launched. In 1981, the Dynamics Explorer-1 and -2 satellites (also called DE-A and DE-B), in high and low eccentric orbits, respectively. The REX-1 and -2 (Radiation Experiment) satellites were launched in 1991 and 1996, respectively, in low orbits ($h = 800$ km), etc [4].

In a separate group are the military reconnaissance satellites. To this group of satellites belongs the first working navigation system of the US Navy. The first polar-orbiting satellite of this group was Transit-5A, launched in 1962, in a low orbit with $h = 340$ km, $i = 90.6^\circ$. The other three satellites, with orbits of $h \approx 1100$ km and inclination $i = 90.0 \pm 0.3^\circ$, respectively, Transit-5B 1, launched in 1963, right next to Transit-O-23 and -O-32, then Transit-O-25 and -O-31, launched in pairs in 1988 [4].

Military reconnaissance satellites designed to operate for long periods (the French Helios satellites) can also be found in these orbits. On the other hand, for reconnaissance satellites on short sporadic missions of a few days or so, the idea of an orbit synchronous with the Sun would be nonsensical. In fact, each orbit is synchronous with the Sun for a period of three days, in the sense that the satellite will fly over a given latitude at nearly constant local time.

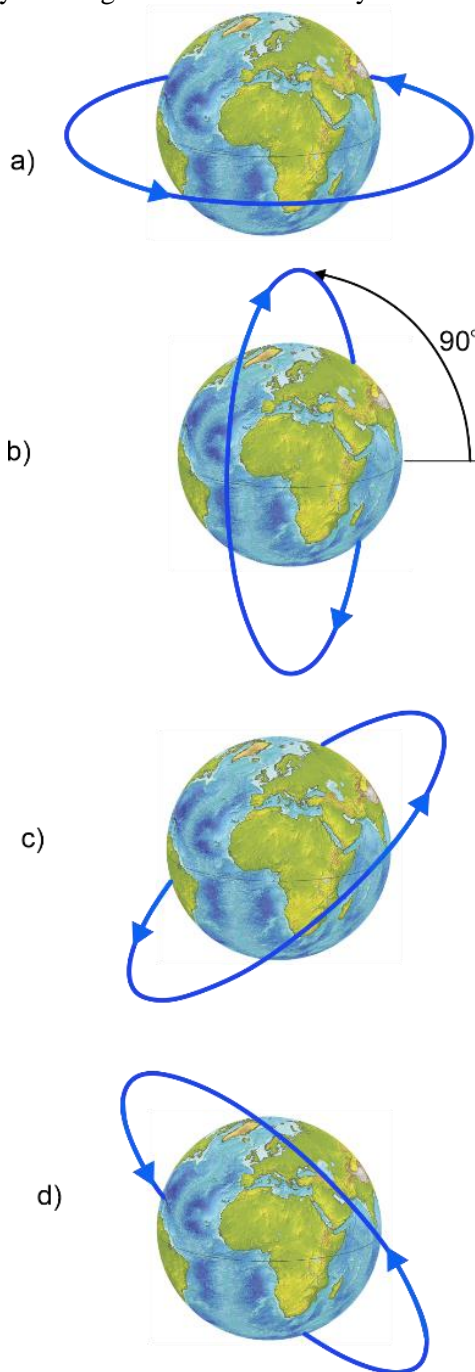


Fig. 1. Inclination angle

The Hohmann transfer can be used for non-coplanar orbits in addition to coplanar ones. That is, to change the orbital plane, the satellite needs to create the velocity that will take it out of its current plane. As the orbital plane changes, the inclination of the orbit changes. For changes in the plane, the direction and magnitude of the satellite's initial and final velocities must be taken into account.

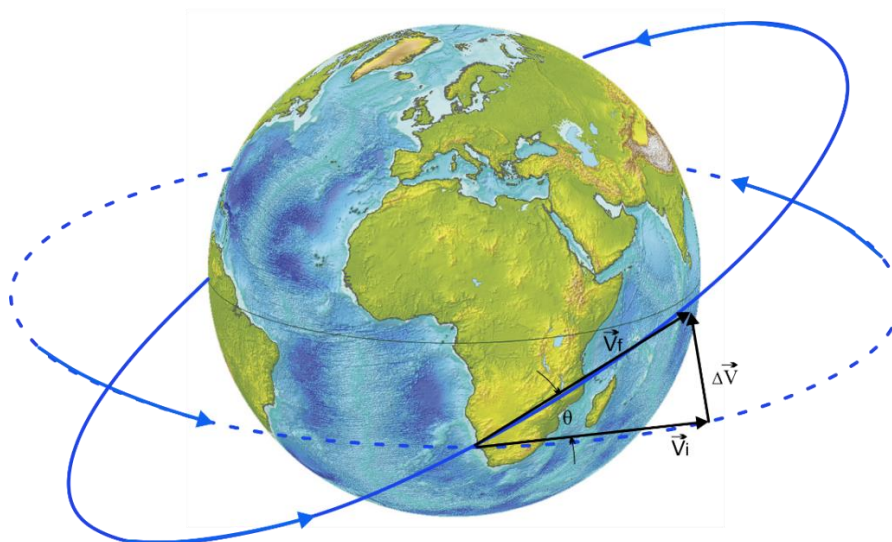


Fig. 2. Plane change

In this case, the initial and final velocities must remain the same, and to change the inclination of the orbit it is necessary to change the velocity at the ascending or descending node [3]:

$$\Delta V = 2V_i \sin\left(\frac{\theta}{2}\right), \quad (1)$$

where: ΔV – velocity change;

$V_i = V_f$ – velocities in the initial and final orbits;

θ – plane-change angle.

In this case, the orbit will rotate around the line connecting the two nodes and only the inclination of the orbit will change.

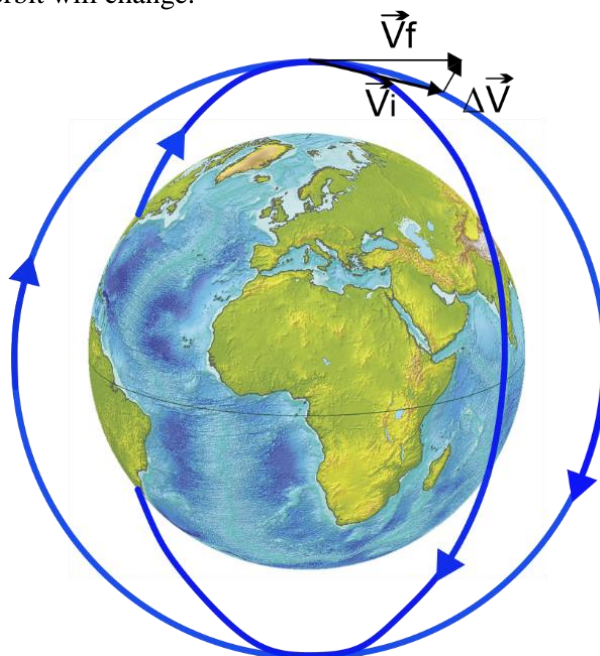


Fig. 3. Velocity change

When the purpose of the maneuver is to make a satellite observation over a specific point (a specific target) on the Earth at a specific time of day, a change of plane can be used to change the right ascending point.

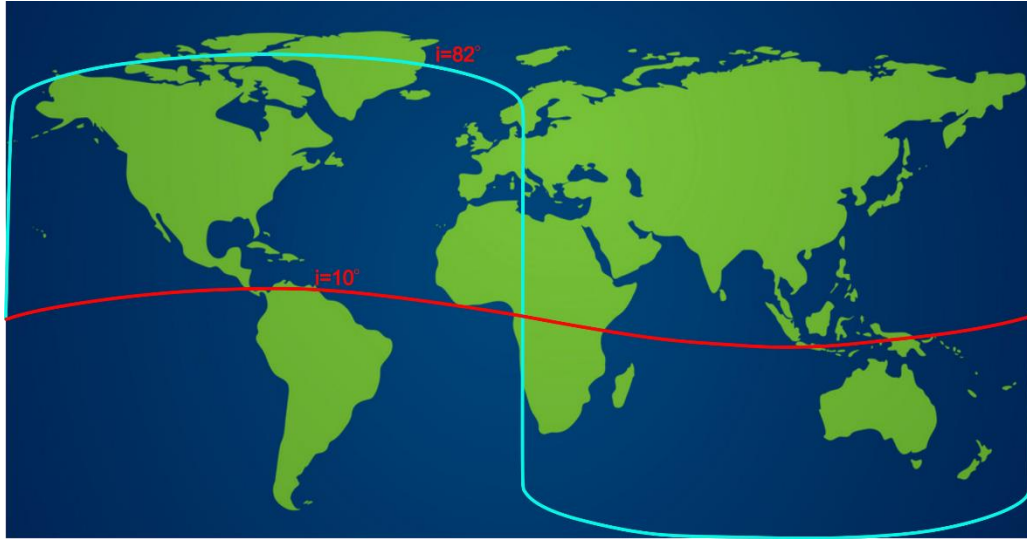


Fig. 4. Trajectory of a satellite on the Earth's surface

2. Transfer of Hohmann

In a polar orbit, a change of plane above the North or South Pole results in a change of the right ascending node ascension only. A plane change made anywhere else changes the inclination and right ascension of the ascending node [1, 2].

Hohmann transfer equation:

$$\Delta V_{mfi} = \sqrt{GM \left(\frac{2}{R_i} - \frac{1}{R_{i+f/2}} \right)}, \quad (2)$$

where:

ΔV_{mfi} - magnitude of the first impulse;

$R_{i+f/2} = \frac{R_i + R_f}{2}$ - semi-major axis of transfer.

$$\Delta V_{msi} = \sqrt{GM \left(\frac{2}{R_f} - \frac{1}{R_{i+f/2}} \right)}. \quad (3)$$

The difference between the speed on the final orbit and the apogee speed of the transfer ellipse is:

$$\Delta V_{msi} = V_{cl} \sqrt{\left(\sqrt{\frac{R_i}{R_f}} \right)^2 + \left(\sqrt{\frac{R_i}{R_f}} \right)^2 \left(\sqrt{\frac{2R_i}{R_i + R_f}} \right)^2 - 2 \left(\sqrt{\frac{R_i}{R_f}} \right)^2 \sqrt{\frac{2R_i}{R_i + R_f}}} \quad (4)$$

where:

ΔV_{msi} - magnitude of the second impulse;

V_{cl} - circular local velocity.

Hohmann transfer allows orbital transfer between two circular orbits which have different orbital inclinations.

$$\Delta V_{msi} = V_{cl} \sqrt{\left(\sqrt{\frac{R_i}{R_f}} \right)^2 + \left(\sqrt{\frac{R_i}{R_f}} \right)^2 \left(\sqrt{\frac{2R_i}{R_i + R_f}} \right)^2 - 2 \left(\sqrt{\frac{R_i}{R_f}} \right)^2 \sqrt{\frac{2R_i}{R_i + R_f}} \cos \theta_{si}}, \quad (5)$$

where: $\cos \theta_{si}$ - plane change from the second impulse.

2.1. Numerical solution

As the name suggests, polar orbits pass over the Earth's polar regions from north to south. A satellite's orbit does not have to cross the poles exactly to be called a polar orbit. An orbit that passes within 20-30 degrees of the poles is still classified as a polar orbit.

Polar orbits are used for reconnaissance and Earth observation. If a satellite is in a polar orbit at an altitude of 800 km, it is moving at approximately 7.5 km per second.

These orbits are mostly performed at low altitudes between 200 and 1000 km. Satellites in polar orbit view the entire Earth's surface from above and may pass over the North and South Poles several times a day.

Results from Hohmann orbit transfer analysis

Source data:

- 1) initial orbit altitude - 200.0000 km;
- 2) final orbit altitude - 1000.0000 km;
- 3) initial orbit inclination – 60°;
- 4) final orbit inclination – 60°.

Results

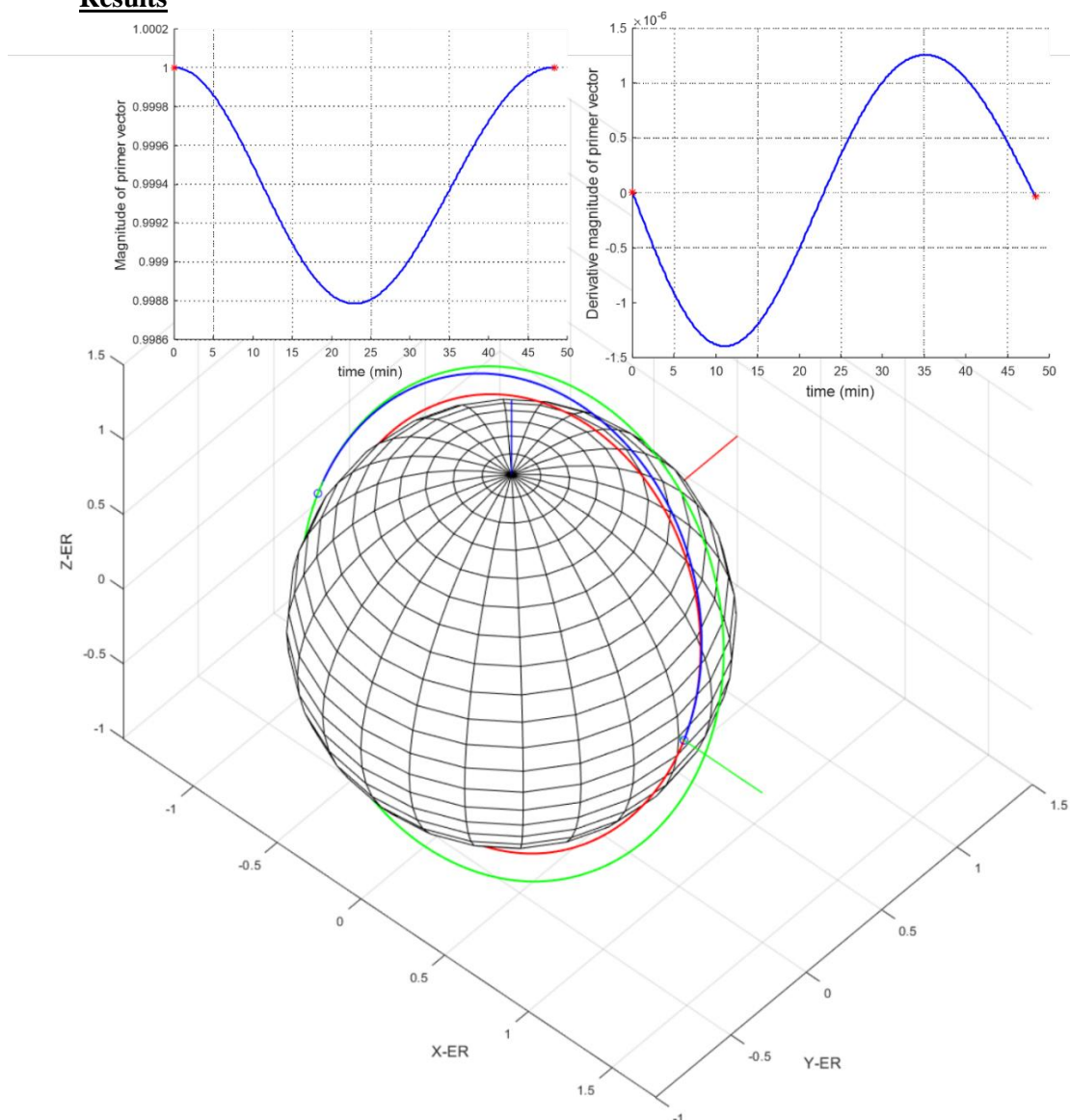


Fig.5. Hohmann orbit transfer in polar orbit

- 1) initial orbit radius - 6578.1363 km;
- 2) initial orbit velocity - 7784.2621 m/s;
- 3) ΔV_{mfi} - 219.9956 m/s;
- 4) first inclination change - 0.0000°;

- 5) final orbit radius - 7378.1363km;
- 6) final orbit velocity - 7350.1389 m/s;
- 7) ΔV_{msi} - 213.7706 m/s;
- 8) second inclination change - 0.0000°;
- 9) total inclination change - 0.0000°;
- 10) ΔV_t - 433.7662 m/s;
- 11) transfer orbit semi-major axis - 6978.1363 km;
- 12) transfer orbit eccentricity - 0.0573;
- 13) transfer orbit inclination -60°;
- 14) transfer orbit perigee velocity - 8004.2577 m/s;
- 15) transfer orbit apogee velocity - 7136.3683 m/s;
- 16) transfer orbit coast time - 2900.6155 s.

Source data:

- 1) initial orbit altitude - 200.0000 km;
- 2) final orbit altitude - 1000.0000 km;
- 3) initial orbit inclination – 60°;
- 4) final orbit inclination – 90°.

Results

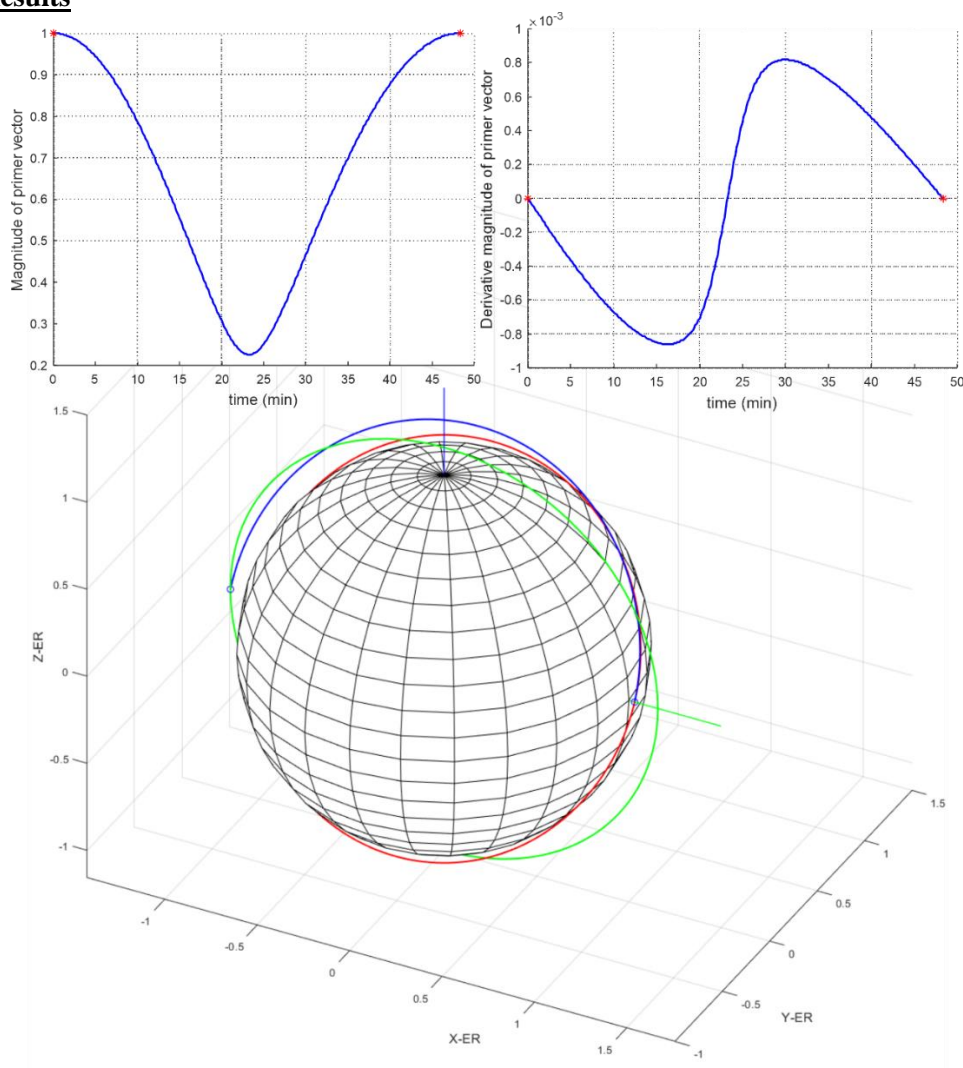


Fig.6. Hohmann orbit transfer in polar orbit

- 1) initial orbit radius - 6578.1363 km;
- 2) initial orbit velocity - 7784.2621 m/s;
- 3) ΔV_{mfi} - 484.4825 m/s;
- 4) first inclination change - 3.1336°;
- 5) final orbit radius - 7378.1363 km;
- 6) final orbit velocity - 7350.1389 m/s;
- 7) ΔV_{msi} - 3371.7999 m/s;
- 8) second inclination change - 26.8664°;
- 9) total inclination change - 30.0000°;
- 10) ΔV_t - 3856.2824 m/s;
- 11) transfer orbit semi-major axis - 6978.1363 km;
- 12) transfer orbit eccentricity - 0.0573;
- 13) transfer orbit inclination - 63.3701°;
- 14) transfer orbit perigee velocity - 8004.2577 m/s;
- 15) transfer orbit apogee velocity - 7136.3683 m/s;
- 16) transfer orbit coast time - 2900.6155 s.

3. Conclusion

The example presented is a typical example of a transfer in low polar Earth orbit.

A comparison is made of the required velocity cost of increasing altitude while maintaining orbit inclination and increasing altitude while increasing orbit inclination to pure polar, and calculations are presented that help to make the necessary analysis in the Hohmann transfer. It can be seen that when an orbit change is required in low Earth orbits, the cost of the required transfer rate is relatively small. However, if a change of the orbit inclination angle to polar is also required, almost twice as much velocity expenditure is required for the first pulse and ten times as much velocity expenditure is required for the second pulse to change the orbit altitude and inclination.

The obtained results for magnitude and derivative magnitude of primer vector show that the proposed transfers are optimal.

References

1. Jezewski D., Lyndon B., Primer Vector Theory and Applications, Space Center Houston, NASA Technical Report.
2. Montenbruck O., Gill E., Satellite Orbits — Models, Methods, and Applications, New York, 2000.
3. Wright D., Grego L., Gronlund L., The Physics of Space Security, NASA, 2005.
4. Wilmer M., Military Applications of High-Altitude Satellite Orbits, Department of the Air Force, 2016.

Tracking a Low Earth Orbit Satellite

Konstantin Metodiev

Space Research and Technology Institute, Bulgarian Academy of Sciences, Sofia, Bulgaria,
komet@space.bas.bg

Abstract: Current study objective is to propose a solution to orbital elements propagation problem and gather images from NOAA-18 low Earth orbit satellite. Free software packages have been used to determine orbit osculating elements and orbital decay. In addition, rise and set times are predicted of satellite – ground station visibility periods. The satellite transmits automatically an analogous signal containing images at long-wave infrared and between near-visible and mid-wave infrared wavelength. The signal is stored by listening to a web-based software-defined radio. After demodulation, the signal is converted to a grayscale image.

Keywords: *SciLab, CelestLab, Orbit Propagation, NOAA-18, Automatic Picture Transmission*

1. Introduction

Trajectory of a celestial body moving within conservative force field is relatively easy to predict. In real life however, various perturbing forces act on the satellite and make it deviate from an ideal orbit predicted by the central-force problem. These might be variations of the Earth attractional force including zonal (due to central body oblateness), sectorial, and tesseral effects, solar wind, atmospheric drag, third body gravity, the Earth radiation pressure as a result of albedo, and relativistic effects to name but a few. What is more, the perturbing forces might be as big as or even bigger than the central attracting force. For instance, the J2 zonal harmonic is about 1000 times bigger than the lower order zonal harmonics and has the strongest perturbing effect on the orbit. As a result, orbit propagators are based on different equations of motion and numerical integration methods.

An artificial Earth satellite, one which had been roaming in the space for years even withdrawn from active service, tends towards a subtle descend (in free fall) under the influence of gravity. This implies, apart from evident satellite loss, some further difficulties the ground station crew get themselves into – data uncertainty, downlink attenuation, prediction of re-entry impact points of a virtually uncontrolled space object – and yet, though the satellite has a little life left, it is not considered redundant for being a useless piece of equipment – in fact the satellite is valued all the more. Orbital decay analysis deals with gradual decrease of the orbital elements as long as possible.

The current study comes up with a simple approach towards downloading images from Low Earth Orbiting (LEO) NOAA-18 satellite as well as orbit propagation including orbital decay. The software tools used to solve the problem are released for free and relatively easy to employ. They represent a good alternative to costly commercial packages.

2. Materials and Methods

The project has been implemented by means of SciLab, [1]. Both Celestlab, [2] and CelestlabX toolboxes are required in advance. An official permission to use the toolboxes is given by CeCILL free software license agreement, [3].

2.1. Osculating elements

A celestial body is said to move along an osculating orbit if all perturbing accelerations could be removed at a particular time (epoch), [4]. Both osculating and mean orbits share a common center of curvature. Alternative interpretation suggests that the osculating elements correspond to parameters of a Keplerian orbit that the satellite would follow if the perturbations suddenly ceased to act, [5]. CelestLab function CL_tle_genEphem generates an ephemeris (osculating position and velocity) from TLE within time of propagation. The function takes formal arguments TLE and a vector of modified Julian dates. There is an important point here worth noting, though. NASA has started counting Julian

days since 1st of January, 1958, whereas CNES Julian days start at 1st of January, 1950. Function CL_dat_convert converts a date from one type to another. It could be used to get the modified Julian date since 1950 (CNES).

2.2. Orbital decay (mean orbital state)

The Semi-analytic Tool for End of Life Analysis software (STELA) has been designed by CNES (French Space Agency) to support the French Space Operations Act. The CelestLabX v.3.4.1 toolbox includes an embedded version of STELA v.3.2. The STELA is said to be able to:

- Propagate (in long term) orbits around the Earth;
- Compute state vector time derivatives due to various forces;
- Compute satellite cross-sectional area, [6].

In current study, the aforementioned abilities have been utilized to predict orbital decay of NOAA-18. The satellite lifetime mainly depends upon mass to cross-sectional area ratio, satellite attitude including solar panels orientation, and upper atmosphere density.

The satellite NOAA-18 has following physical properties: 4.19 m (13.7 ft) long, 1.88 m (6 ft 2 in) wide (diameter), solar array 2.73 m by 6.14 m, launch mass $m = 2232$ kg (4921 lb), B^* drag term = $0.16185e-03$ EarthRadii⁻¹ (taken from TLE). Function CL_stela_area computes the area projected perpendicularly to a given direction. The mean satellite area (fixed solar arrays) $A = 3.5376399$ m² is computed further based on quadrature by CL_mean function. Given TLE data, the ballistic coefficient $Cd \cdot A/m = 2.0622e-03$ is computed by CL_tle_getBalCoef function, hence the drag coefficient $Cd = 1.3011218$. A good tutorial on computing the satellite drag coefficient might be found in CelestLab help pages. The user should look up for “Calculation of atmospheric drag.”

In paper [7] Cook recommends an average $Cd = 2.2$. This value is commonly applied to satellites with compact shapes in free molecular flow. It is acceptable should there be no alternative.

The quantities above have been computed after parsing a TLE script by CL_tle_parse function.

Table 1. Two-line elements set, NOAA-18, used in current study case

1	28654U	05018A	23028.13469840	.000000257	00000-0	16185-3	0	9997
2	28654	98.9255	103.1330	0014964	59.1090	301.1551	14.12849847911795	

2.3. Satellite crossing times

Mean local time of the ascending node (MLTAN) is yet another local time on the ground track. The MLTAN indicates an exact local time at which the satellite is crossing the equator from south to north. Alternatively, the MLTAN is defined as an hour angle between two meridian planes: one containing the line of nodes and other containing the mean Sun. The right ascension of the ascending node (RAAN) angle is given in inertial frame, consequently it does not account for the Earth rotation. The CelestLab function CL_op_locTime might be used to switch between RAAN and MLTAN. Alternatively, one may compute the MLTAN by means of formula, [8]

$$(1) \quad MLTAN = \frac{\Omega - \alpha_{\odot}}{15} + 12$$

where Ω is RAAN and α_{\odot} is right ascension of the mean Sun. The latter quantity is determined from following formula

$$(2) \quad \alpha_{\odot} = \alpha'_{\odot} + EqT$$

where α'_{\odot} is right ascension of the apparent Sun and EqT is Equation of Time.

Difference (in minutes) between apparent Sun and mean (fictitious) Sun is called Equation of Time. The mean Sun travels along the celestial equator at a uniform rate. It takes the mean Sun exactly the same time as the apparent Sun to complete one revolution (Simon Newcomb, 1895). Apparent solar time is a natural time whilst mean solar time assumes all days are 24 hours long. In Fig. 1, the Equation of Time is plotted for year 2023. Celestial coordinates (right ascension and declination) of the apparent Sun are computed by means of an algorithm described in [9].

The precession rate of a Sun-synchronous orbit equals orbital period of the Earth, i.e. about 365 solar days. Hence, the Sun-synchronous orbit maintains same orientation with respect to the Sun. In order to do that, the line of nodes must complete one revolution (360 deg) within a year. To meet Sun-orbit alignment criteria, the RAAN/MLTAN relationship should be considered obligatorily.

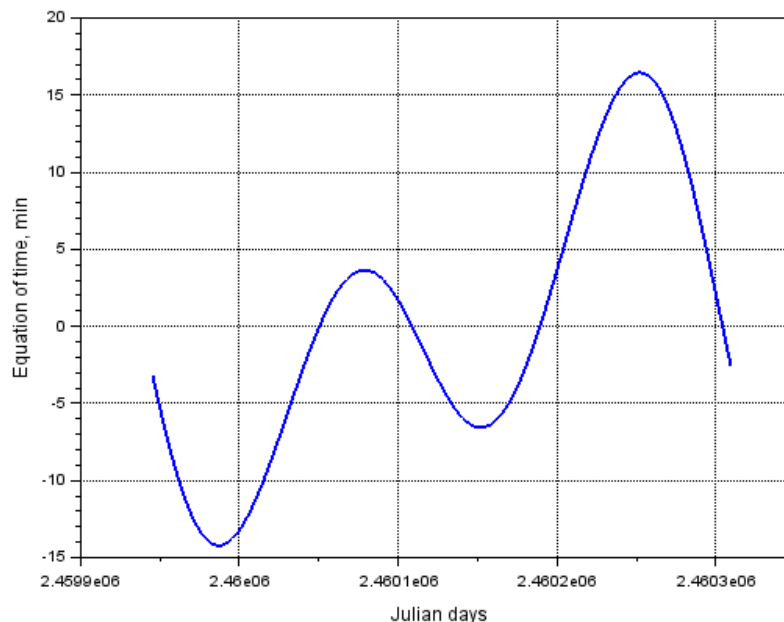


Fig. 1. Equation of time for year 2023

2.4. Listening to a web-based software-defined radio

A web-based software-defined radio is a radio repeater which shares data over the Internet and makes it possible for many users to listen to broadcasts and tune it at the same instant. Users can connect to the WebSDR server through a browser, open the interface page, and tune around the audio spectrum (divided into bands in advance). A band spectrum is visualized by means of the short-time Fourier transform which is used primarily to work out frequency and phase content of local sections of a non-periodic signal. It is widely known as “the waterfall.” In Fig. 2, web page of a Nuremberg-based repeater, [10] is shown alongside a satellite tracking window (left half). The NOAA-18 satellite appears to be within range which is why the automated radio transmission can be seen on the waterfall window, i.e. the rightmost red strip. Apart from various filters, frequency bands, and other settings, the interface provides a possibility for the user to store a transmission and download it subsequently as a WAV file. Downlink center frequency of NOAA-18 is 137.9125 MHz.

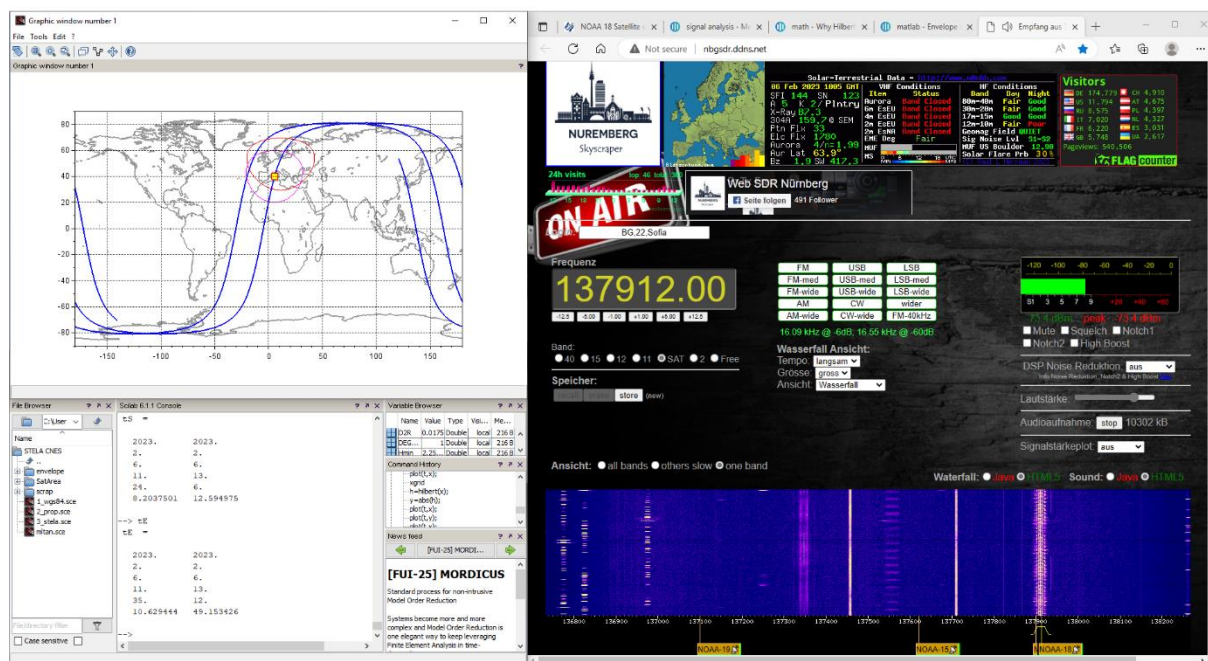


Fig. 2. Ground track in SciLab (left) and interface page of the WebSDR repeater in Nuremberg

2.5. Signal Processing

NOAA-18 satellite transmits weather images automatically. The raw analogous signal (at frequency of 2080 Hz) is amplitude modulated onto a 2.4 kHz sub-carrier and subsequently frequency modulated onto the 137 MHz carrier wave. Then the signal is passed on further to the on-board VHF transmitters.

Two ways of envelope extraction (signal demodulation) are commonly employed:

- Hilbert transform (function Hilbert)
- Low pass Butterworth filter (function iir) with cut-off frequency about 0.4π rad/sample or less
- “Lossy” peak detector, etc.

Function Hilbert in SciLab returns analytic representation of the signal in the form $X = x + j*y$. The real part x contains the source signal, whilst the imaginary part y contains the Hilbert transformation. In exponential notation, $X = A(t)*exp(j*\varphi(t))$ where $A(t)$ is amplitude, $\varphi(t)$ is phase, and $abs(A(t))$ is the envelope. By all accounts, Hilbert transformation does not work well in case of a broadband signal demodulation. Low-pass filter is preferable with cut-off $f = 0.38*11025/2 \approx 2095$ Hz or less.

The automatic picture transmission frame consists of two image channels (near-visible and long-wave infrared), image telemetry, and synchronization signal. Data are transmitted sequentially (in series) as a line. A complete line is 2080 pixels long. It takes each line 0.5 seconds to get across. The synchronization signal pattern is shown in Fig. 3, [11].

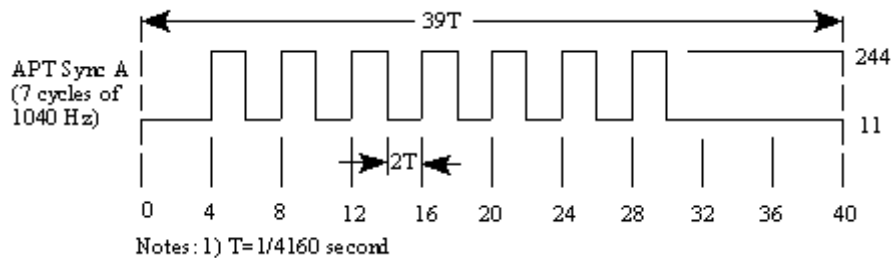


Fig. 3. Synchronization signal at the beginning of video line

Convolution and cross-correlation are both operations applicable to signals. Cross-correlation means moving a kernel (filter) smoothly across a signal, whereas convolution stands for sliding a flipped kernel across a signal. In addition, cross-correlation might be considered as sliding a dot (inner) product of two signals.

In order to detect the beginning of each APT frame, an exemplary synchronization signal was generated and convolved afterwards with the WAV file. The expected pattern is shown in Fig. 4, right half. It represents the signal convolved with a time-shifted representation of itself.

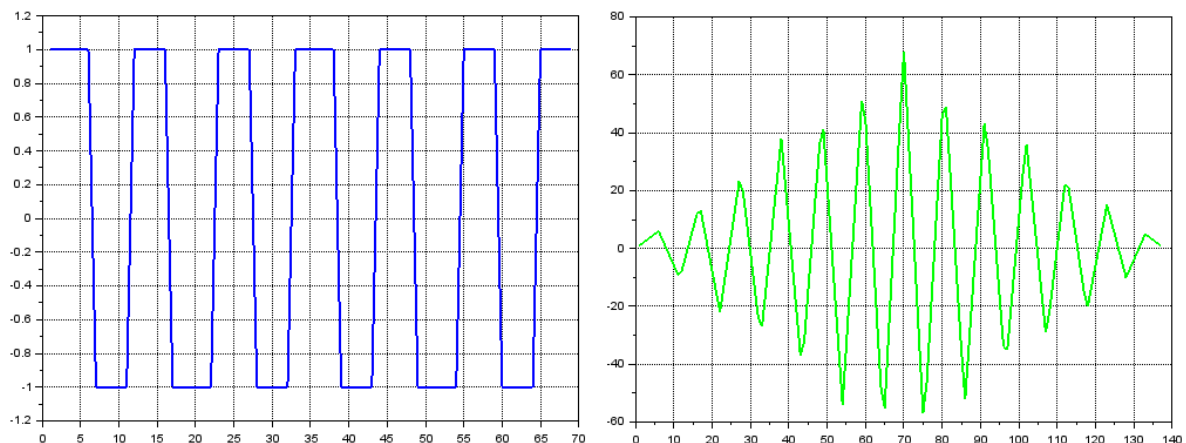


Fig. 4. Generated synchronization signal (left) and convolution, $F_s = 11025$ Hz

Sampling rate of the WAV file could be changed by either intdec function (in SciLab environment) or SoX tool, [12] whichever is preferable. The intdec function requires Image Processing and Computer

Vision toolbox. The SoX command line is shown in Table 2. In this case, the raw signal is resampled at 11025 Hz (samples per second, sps, unit might be used alternatively).

Table 2. Change sampling rate of a WAV file by means of SoX (Sound eXchange)

```
PS D:\%PathToSox%\sox-14-4-2>./sox input.wav output.wav rate 11025
```

3. Results

In following Table 3, two visibility periods of satellite NOAA-18 and ground station Nuremberg are shown. The mask angle is set to 10 deg so as to make up for the local mountain relief (if any) and city outline. The visibility circle increases dramatically for smaller elevation angle values. It was computed by CL_gm_stationVisiLocus function.

Table 3. Visibility passes, NOAA-18, mask angle 10 deg, UTC+1

Rise		Max		Set	
Local time	Azimuth, deg	Elevation, deg	Azimuth, deg	Local time	Azimuth, deg
02 Feb, 10:32	NNE 27.394	41.597	E 99.278	02 Feb, 10:42	SSE 168.404
02 Feb, 12:13	N 1.02	35.566	WNW -61.777	02 Feb, 12:22	WSW -127.07

In Fig. 5, satellite ground track is depicted, so are the subsatellite point and the ground station (Nuremberg) visibility loci. In the figure, the satellite is expected to remain within ground station visibility scope for 9 minutes (Table 3, second row). The ground track equatorial shift (difference in longitude between two consecutive ascending nodes) could be accounted for by the Earth rotation and line of nodes precession (node regression). In case of retrograde orbits, such as the orbit of NOAA-18, the line of nodes shifts in direction of the Earth rotation. The phenomenon is solely depictable in Earth Centered Earth Fixed coordinate frame.

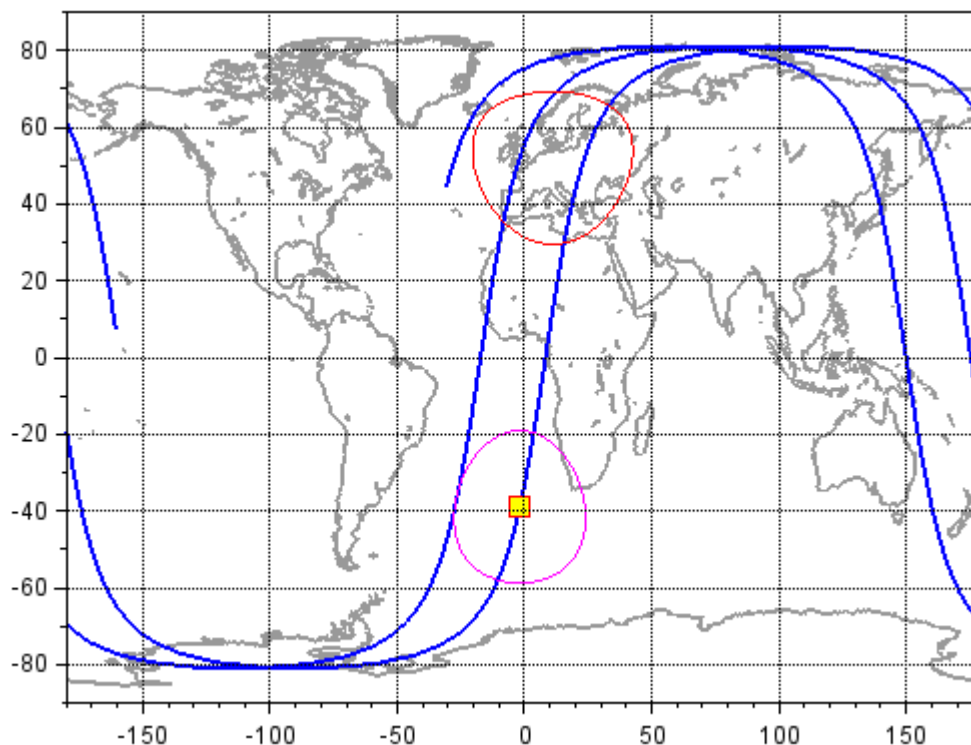


Fig. 5. Orbit track (blue), subsatellite point (magenta), and ground station (red) visibility loci

In Fig. 6, celestial coordinates of the satellite, according to data in Table 3, second row, are shown during two visibility intervals. The left parabola corresponds to a forthcoming visibility period. The satellite is expected to rise at 1.02 deg North and set at -127.073 deg West-South-West azimuth. Note, the elevation angle has been set to 10 deg, hence the curve end ordinates.

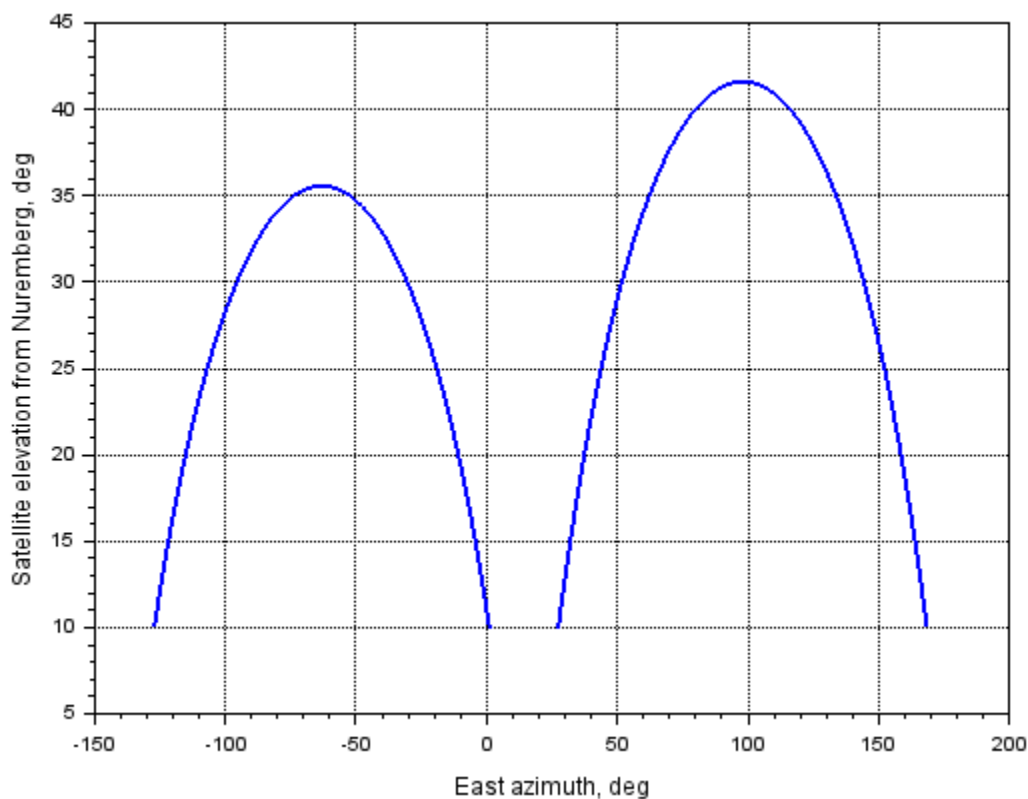


Fig. 6. Celestial coordinates of NOAA-18 during visibility interval

In Fig. 7, 8, two Keplerian elements are shown, i.e. inclination and semi-major axis, computed by STELA in terms of modified Julian date. The simulation period is 18 years (since 3rd of June, 2005).

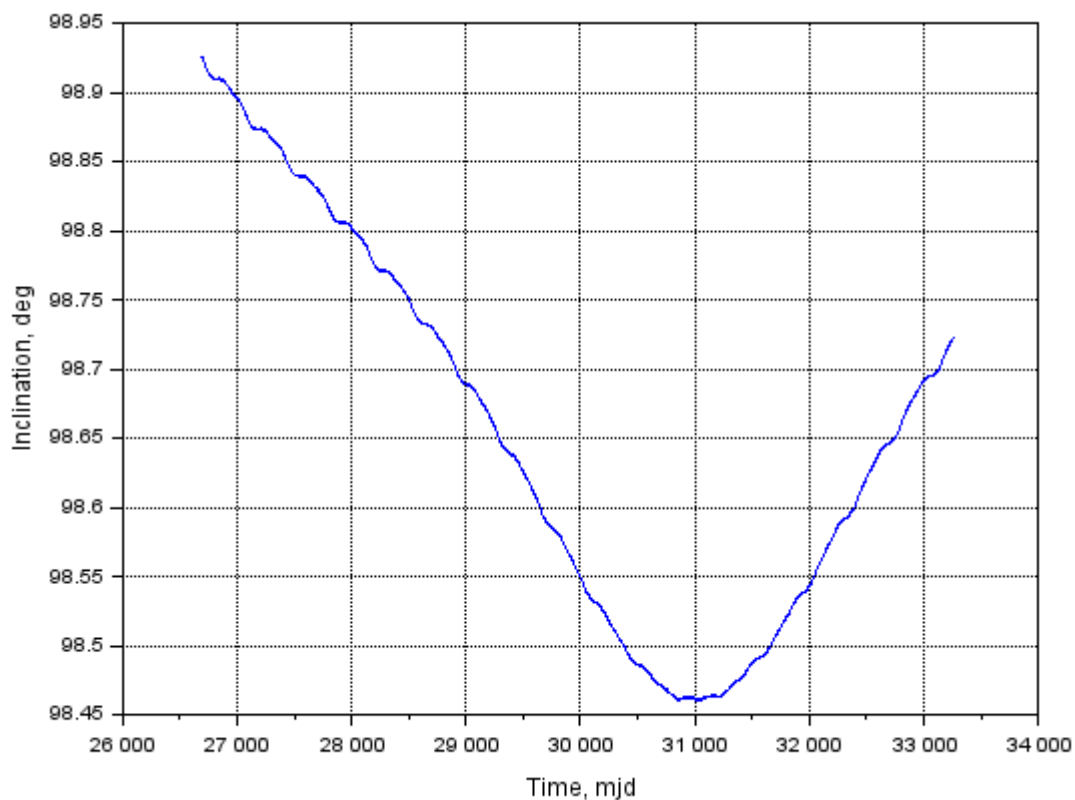


Fig. 7. Inclination, deg, vs. time, modified Julian date

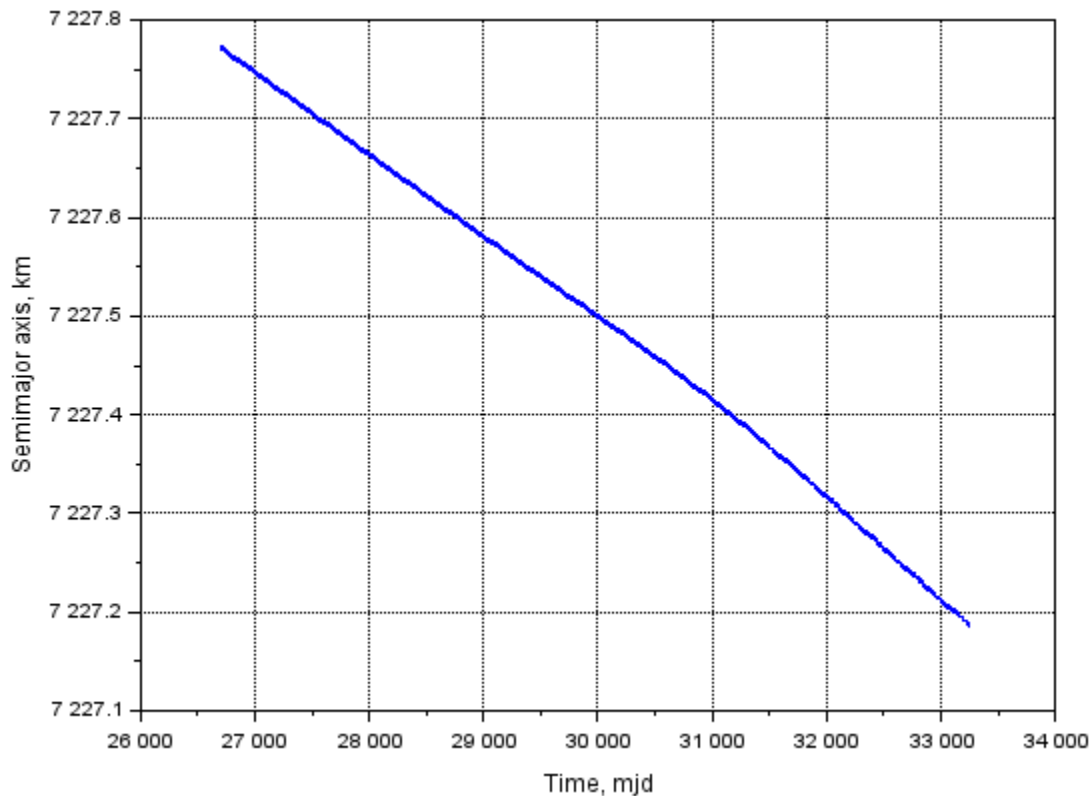


Fig. 8. Semimajor axis, km, vs. time, modified Julian date

Fig. 9 shows the obtained signal after convolution, in other words searching the demodulated WAV file for any synchronization signal. “Spikes” are set approx. 5500 samples apart, divided by sampling frequency of 11025 Hz equals 0.5 seconds. This result agrees well with the APT frame format, [11]. Both near-visible and long-wave infrared lines are discernible.

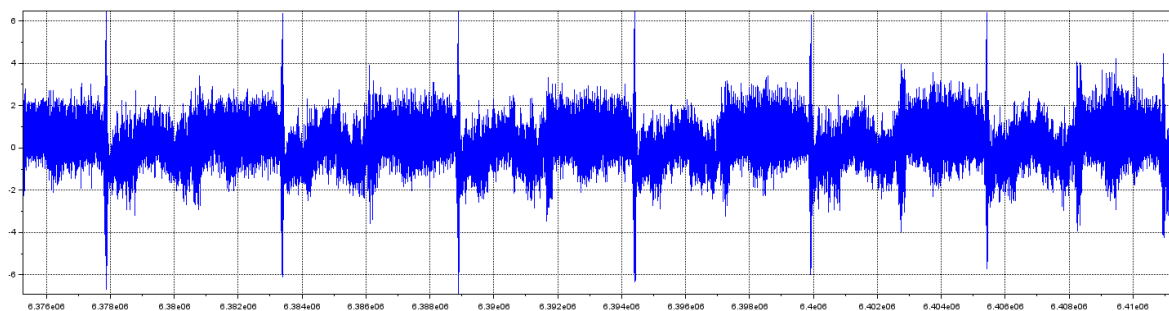


Fig. 9. Signal obtained after convolution, $F_s = 11025$ Hz

In Fig. 10, a decoded picture (near-visible and long-wave infrared) derived from the WAV file is depicted. There are good tools for decoding WAV files transmitted by NOAA satellites, [13], [14]. Image shown in Fig. 10 was obtained by noaa-apt tool. Short lateral strips on the right side of each image indicate image telemetry which is used to decode the image channel (reference values).

One reason of bad image quality might be low image resolution, i.e. 4 km/pixel.

4. Conclusions

CelestLab provides a quick and efficient way of propagating satellite orbits. The toolbox is being developed regularly and, what is more, available to the public for free. It solely takes the developer a few lines of code to work out a solution to the laborious problem of propagating satellite position and velocity. An exemplary code for osculating elements propagation might be found in Appendix section.

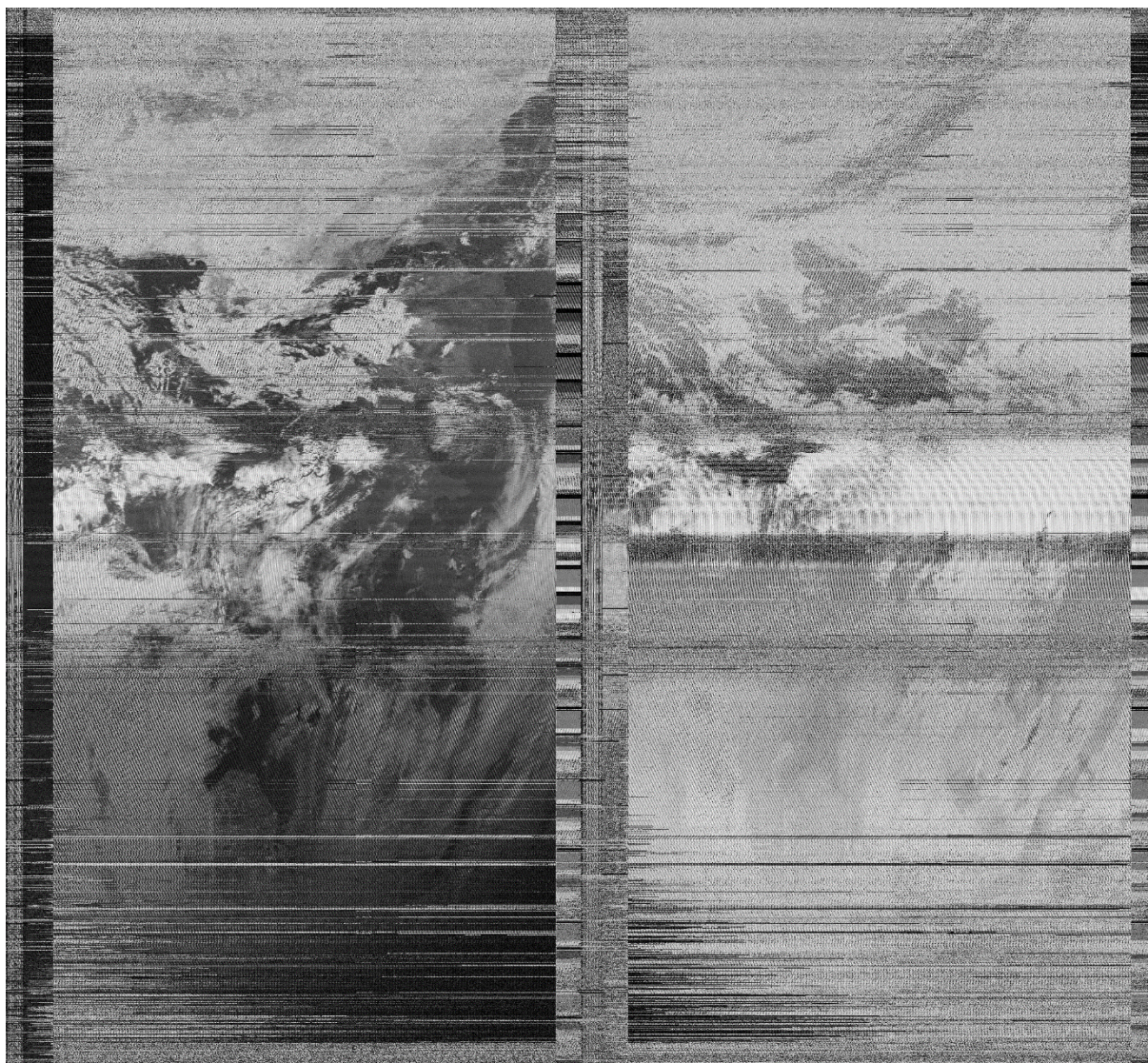


Fig. 10. NOAA-18 decoded images

It might be a better idea to buy a real computer-based radio receiver instead of listening to a web-based one. For example, RTL-SDR dongle, [15] is a cheap wideband software-defined radio which is regarded with great favour and approval by radio amateurs. Having acquired the hardware, the user might get weather images of hers/his current whereabouts.

Receiving and listening to radio messages is said to be always legal. Listening to a web-based repeater has never been in violation of the local legislation.

References

1. <https://www.scilab.org/>
Copyright © 1989-2005, INRIA ENPC. Scilab is a trademark of INRIA
2. Lamy, A., T. Martin, Celestlab: Spaceflight Dynamics Toolbox for Mission Analysis, 6th International Conference on Astrodynamics Tools and Techniques (ICATT), 14-17 March 2016, Darmstadt
<https://atoms.scilab.org/toolboxes/celestlab>
3. CeCILL (Ce[a] C[nrs] I[nria] L[ogiciel] L[ibre])
<https://atoms.scilab.org/licenses/1>
4. Bate, R., D. Mueller, J. White, Fundamentals of Astrodynamics, Dover Publications, Inc., New York, 1971, ISBN 0-486-60061-0, p. 391
5. Capderou, M., Satellites Orbits and Missions, Springer-Verlag France 2005, p. 77, ISBN: 2-287-21317-1
6. <https://www.connectbycnes.fr/en/stela>

7. Cook, G. E., Satellite Drag Coefficients, Planet. Space Sci., Vol. 13, 1965, p. 929
8. Mean Local Time of the Ascending Node, Explanatory Notes, Celestial and Orbital Mechanics series
<https://www.yumpu.com/en/document/read/36384921/mean-local-time-of-the-ascending-node-orbital-and-celestial->
9. Explanatory Supplement to the Astronomical Almanac, edited by P. Kenneth Seidelmann, University Science Books, Mill Valley, California, 1992, ISBN 0-915702-68-7, p.p. 484, 485
10. <http://nbgssdr.ddns.net/>
11. The NOAA KLM User's Guide, August 2014 Revision p. 4-57
12. <https://sox.sourceforge.net/>
13. <https://noaa-apt.mbernardi.com.ar/>
14. <https://github.com/Xerbo/aptdec>
15. <https://www.rtl-sdr.com/buy-rtl-sdr-dvb-t-dongles/>

Appendix. Osculating orbital elements propagation by means of CelestLab

```
clear;

str = [ .. // NOAA-18
"1 28654U 05018A 23028.13469840 .00000257 00000-0 16185-3 0 9997"; ..
"2 28654 98.9255 103.1330 0014964 59.1090 301.1551 14.12849847911795"];

tle = CL_tle_parse(str);

t = datevec(now()); // Local time (Sofia presumably), hence the line below
t(4) = t(4) - 2; // UTC
cjd0 = CL_dat_convert("cal", "cjd", t);
cjd0 = cjd0 - 1/12/2;
cjd = cjd0 + (0 : 60 : 86400/12) / 86400;

// cal = CL_dat_convert("cjd", "cal", tle.epoch_cjd); disp(cal);
// mlh = CL_op_locTime(cjd0, 'ra', tle.raan, 'mlh'); disp(mlh);

[pos_ecf, vel_ecf] = CL_tle_genEphem(tle, cjd, "ECF", 0);

scf(1);
CL_plot_earthMap(color_id = color("grey60"), res = 'high', thickness = 2);
CL_plot_ephem(pos_ecf, color_id = 2);
```


Fixed wing topology optimization: a numerical procedure for computational design model generation

Nikolay Kanchev

Bulgarian Air Force Academy, Aviation Faculty, Dolna Mitropolia, Bulgaria, nikolaikanchev@yahoo.com

Abstract: One of the most significant areas of research in the field of aircraft design is the reduction of the mass of aircraft structures while maintaining and even improving their mechanical properties. Optimal distribution of the structural material, taking into consideration both the imposed constraints and the state-of-the-art manufacturing technologies, is yet another way to reduce the maximum take-off weight in addition to the application of modern structural materials. Throughout the preliminary and detail stages of design, it is crucial to accurately synthesize the aircraft structural design model while taking into account both the special aspects of the operating conditions and the specifics of the optimization procedure. In this paper, an approach for generating a computer-aided design model of a fixed wing to be used in a topology optimization procedure is proposed and demonstrated.

Keywords: topology optimization, MALE UAV, fixed wing, SIMP, lightweight design.

1. Introduction

Recent methodologies for the design of manned and unmanned aircraft are characterized by the presence of optimization methods and procedures intended to lower the maximum take-off mass. The primary strategies for reducing the weight of the aircraft structure include:

- the use of novel structural materials with high stiffness and low mass;
- the development of structural optimization algorithms with an expanded design space and a sufficiently high, but practically achievable dimensionality;
- utilization of modern methods for reducing the number of assemblies in the structure while taking into consideration the advancements in the additive manufacturing technologies.

Each of the approaches discussed here has as a fundamental requirement that, in the most loaded flight phase, the mechanical properties of the aircraft structure must be preserved or even improved while the mass of the aircraft structure is reduced. This must be done within the bounds of the established safety factor.

The unmanned aerial vehicle's mass includes the useful payload, the equipment, the energy supply (fuel, batteries, etc.) and the load-bearing structure of the aircraft [8, 9, 14]:

$$1) \quad m_{MTOM} = m_{str} + m_{equip} + m_{bat} + m_{payload} \Leftrightarrow \bar{m}_{str} + \bar{m}_{equip} + \bar{m}_{bat} + \bar{m}_{payload} = 1$$

The desire to increase the relative weight of the equipment and payload drives the development of techniques for both reducing the relative mass of the structural layout in either of the aforementioned directions and increasing the energy density of the energy source. The Breguet equations provide a mathematical explanation for the physical effects of \bar{m}_{bat} (or \bar{m}_{fuel} for UAV with internal combustion engine - ICE) and m_{MTOM} on the flight's range and endurance [8, 14]:

<p>• ICE UAV</p> $2) \quad L = \frac{c_L}{c_D} \frac{\eta_{prop}}{BSFC} \cdot \ln \left(\frac{1}{1 - \bar{m}_{fuel}} \right)$ $3) \quad t = \frac{1}{V} \frac{c_L}{c_D} \frac{\eta_{prop}}{BSFC} \cdot \ln \left(\frac{1}{1 - \bar{m}_{fuel}} \right)$	<p>• Electrical UAV</p> $L = \frac{c_L}{c_D} \frac{E_{spec}}{g} \bar{m}_{bat} \eta_{prop} \eta_{bat} f$ $t = \frac{1}{V} \frac{c_L}{c_D} \frac{E_{spec}}{g} \bar{m}_{bat} \eta_{prop} \eta_{bat} f$
--	---

where c_L is the UAV's lift coefficient, c_D is the UAV's drag coefficient, η_{prop} is the propeller efficiency, $BSFC$ is the break specific fuel consumption [kg/(W·h)], V is the UAV's true airspeed [m/s], E_{spec} is the specific energy of the batteries [J/kg], η_{bat} is the efficiency of the power source and f is the battery's usable power coefficient.

Increasing the energy density of the on-board power sources has been the subject of many recent scientific publications and constitutes a distinct line of research [7]. The advancements in structural optimization methods and procedures, on the other hand, have the greatest potential for reducing the maximum take-off mass (MTOM) and for providing essential information on the topology of the load-bearing structure at the early stages of the UAV design [1, 10, 18, 19]. Topology optimization methods are the most advantageous in this aspect [6, 13, 20].

2. Computational design model generation

2.1. Main difficulties in computational design model generation for topology optimization procedure

During the preliminary and detail design stages, it is essential to accurately synthesize a computational design model of the aircraft structure, taking into consideration both the characteristics of the operating environment and the specifics of the optimization procedure. In all methods for gradient and discrete structural topology optimization one has to specify the so called active and passive optimization domains, to select finite elements with sufficient number of degrees of freedom providing medium to high level of discretization, and to choose the control parameters for the optimization process appropriately [5]. The most widely used approach for topology optimization is the method with approximation of the structural elasticity defined as a structural compliance minimum problem with constraint imposed on the relative volume of the final result [4]:

$$\begin{aligned}
 \mathbf{x} &= \{x_1, x_2, x_3, \dots, x_i\}^T, \quad i = 1, 2, \dots, n \\
 \min C(\mathbf{x}) &= \mathbf{F}^T \mathbf{U} = \mathbf{U}^T \mathbf{K} \mathbf{U} = \sum_{i=1}^n \mathbf{u}_i^T \mathbf{k}_i \mathbf{u}_i = \sum_{i=1}^n (x_i)^p \mathbf{u}_i^T \mathbf{k}_0 \mathbf{u}_i \\
 \mathbf{K} \mathbf{U} &= \mathbf{F} \\
 \sum_{i=1}^n x_i v_i / V_0 &\leq f_0 \\
 0 < x_{min} &\leq x_i \leq 1
 \end{aligned}$$

where $x_i = \rho_i / \bar{\rho}$ is the relative density of the i -th finite element, p is the penalty coefficient (usually $p=3$), $C(\mathbf{X})$ represents the objective function – the structural compliance, \mathbf{X} is the global vector of design variables – the relative densities in each of the finite elements, \mathbf{F} is the global vector of external nodal loads, \mathbf{U} is the global vector of the nodal displacements, \mathbf{K} represents the global stiffness matrix of the structure, $V(\mathbf{X}) = V_{str}$ is the volume of the optimal topology, V_0 is the initial volume of the structure, k_i is the stiffness matrix of the i -th finite element with relative density x_i , x_{min} and x_{max} represent the bottom and upper limit of the interval for continuous variation of the elemental densities, k_0 and u_i are the elemental stiffness matrix and nodal displacements vector for the i -th finite element, f_0 is the relative volume, which is the ratio of the final to initial volume of the discretized structure.

The approximation model of the method is defined as follows [4]:

$$E(x_i) = E_{min} + (x_i)^p (E_0 - E_{min}),$$

where E_0 is the structural elasticity, $x_i = \rho_i / \bar{\rho}$ is the relative density of the i -th finite element, p is the penalty coefficient ($p=3$), $E_{min} = 10^{-4}$ for avoiding singularity of the global stiffness matrix and $E(x_i)$ represents the stiffness of the i -th finite element with relative density x_i .

When developing a computational design model for topology optimization of a fixed wing, one should take into account that the procedure's algorithm places the structural material in the zones with greatest nodal displacements of the finite elements [20]. The structure of the fixed wing is characterized with displacements of different magnitudes: large displacements due to general wing bending, small displacements due to wing twisting and even smaller displacements in the skin panels. Detecting the relatively small local displacements of the skin panels, for example, requires a very high degree of

discretization, which usually entails a significant processing power [1]. The topology optimization procedure allows for the generation of optimal and rational designs based on some previously available information about the object and its operating conditions. The main goal is to restrict and guide the feasible optimization space toward structural topologies which satisfy those technology requirements that cannot be explicitly or implicitly defined in the optimization problem. Such requirements in the context of the optimal design of a fixed wing for a UAV include providing a margin of stability against buckling, preservation of the aerodynamic shape in the most loaded flight phase, etc.

2.2. Numerical procedure for UAV's fixed wing computational design model generation

General fixed wing parametrization is performed with a computational design model composed of multiple spanwise airfoils placed at specific incidence angles in accordance with the aerodynamic and geometric twist distribution. The model generation procedure performs preliminary design of the airfoils through a set of control points connected with high-order parametric curves and subsequent closure of the sections with common parametric surface forming the outer streamlined skin [15]. The parameterization of each airfoil is achieved by the fitting of the high-order curves to the control points whose coordinates are obtained either by analytical expressions or from a coordinate file. The most common analytical approaches for generation of the sectional airfoils control points are:

- from the NACA series through equations for the curvature of the mean camber line and the airfoil thickness distribution along the chord (Fig.1) [2];
- implicitly by class and shape functions, the so-called CST approach (Class-Shape Transformation) [11, 12];
- by variation of particular geometric parameters (leading edge radius, maximum thickness, maximum curvature, angle at the trailing edge, etc.), the so-called PARSEC method [16].

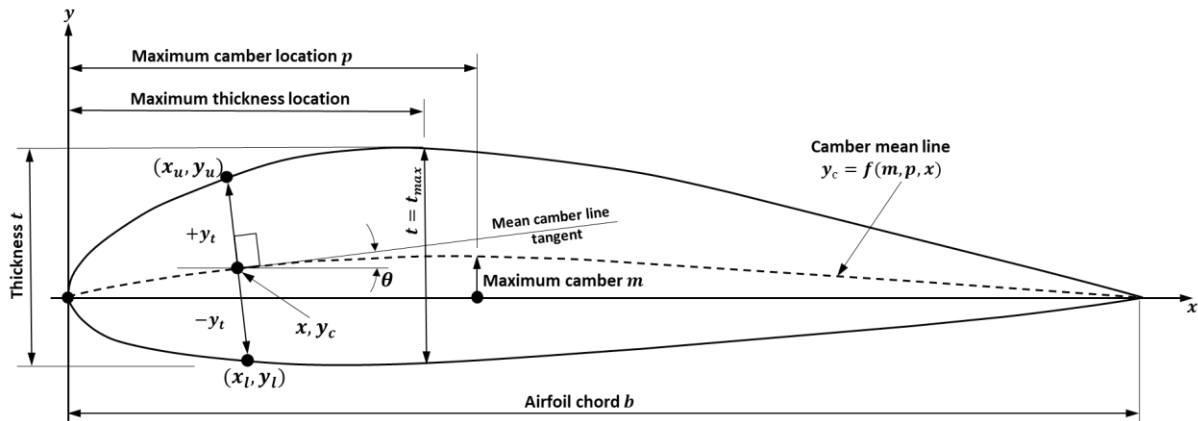


Figure 1. Basic parameters of the NACA series airfoils [2]

Figure 2 depicts the flowchart of a NACA series airfoil generation algorithm applicable in a numerical procedure for parametric modeling of a fixed-wing aircraft. The contour of the profile is modeled by b-spline functions based upon the control points obtained in advance.

The synthesis of the computational design model of a fixed wing for UAV is carried out by sequential generation of the airfoils in the particular sections with a subsequent loft of the sections by non-uniform rational basis spline (NURBS) forming the streamlined skin surface [15]. With previously specified span l_{wing} , area S_{wing} , taper η , sweep χ , dihedral ψ and relative thicknesses c_0 and c_t of the base and tip chord, the design model of the wing is built by calculating some additional parameters using the following analytical expressions [21]:

- base chord length b_0 , tip chord length b_t and aspect ratio λ of the wing:

$$6) \quad b_0 = \frac{2\eta S_{wing}}{l_{wing}(\eta + 1)}; \quad b_t = \frac{b_0}{\eta}; \quad \lambda = \frac{l_{wing}^2}{S_{wing}};$$

- leading and trailing edge sweep χ :

$$\chi_{l.e.} = \arctan \left[\tan \chi_{1/4} + \frac{\eta - 1}{\lambda(\eta + 1)} \right]$$

$$\chi_{tr.e.} = \arctan \left[\tan \chi_{l.e.} - \frac{4(\eta - 1)}{\lambda(\eta + 1)} \right]$$

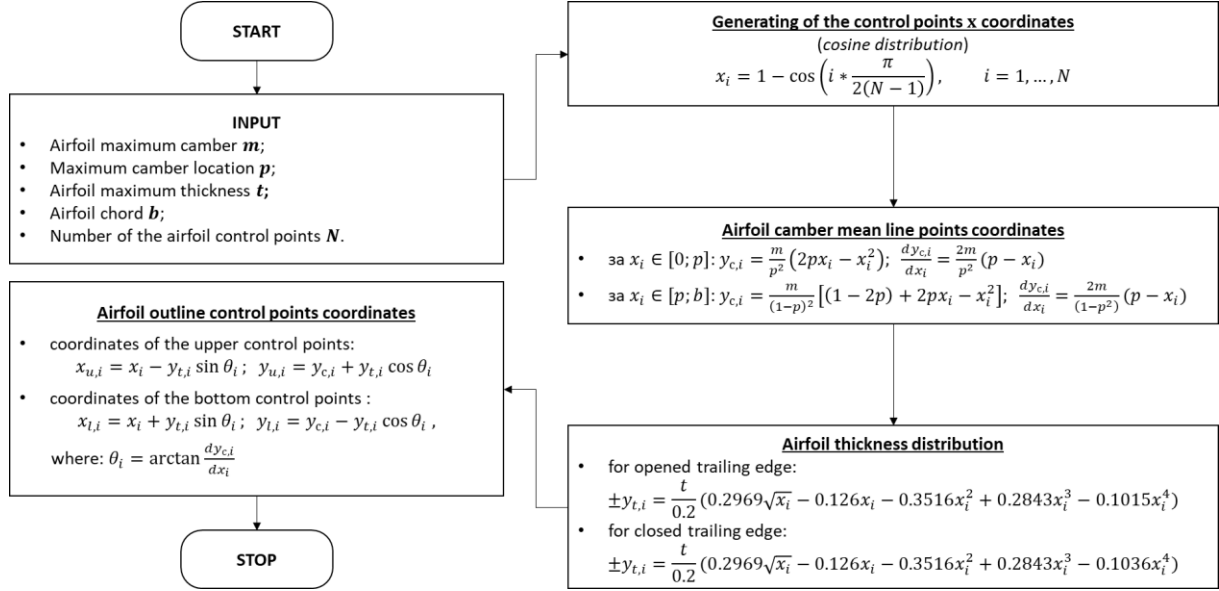


Figure 2. Flowchart of the NACA series airfoil generation algorithm.

The base and tip chords, the relative thicknesses of the individual sections of the wing, as well as their distances from the main chord, are calculated by linear interpolation (Fig. 3).

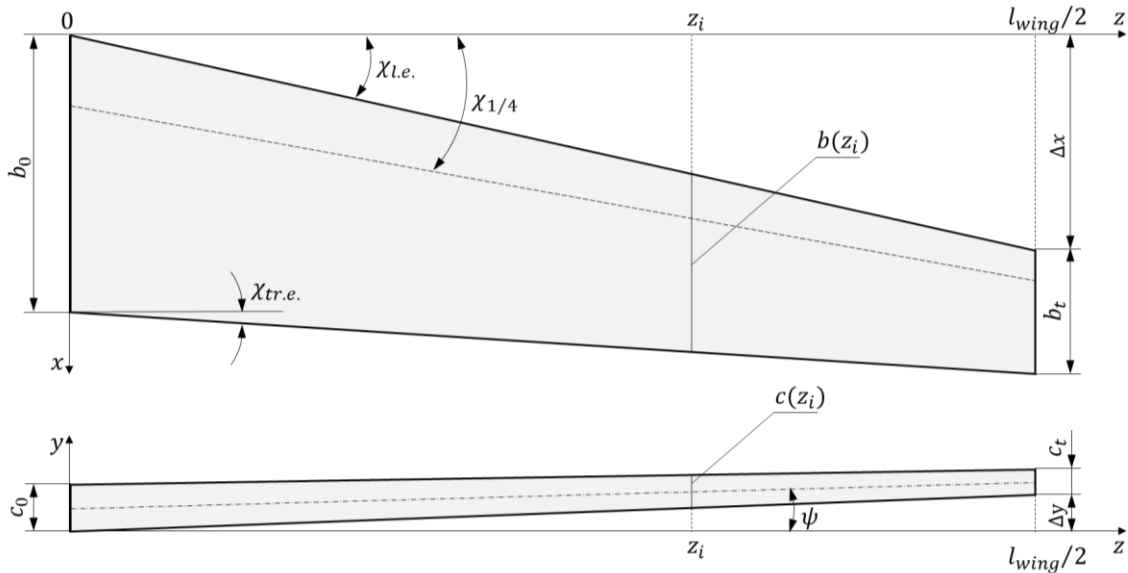


Figure 3. Basic parameters of the UAV fixed-wing design model

When the configuration of the stiffeners (*stringers*, *ribs*) is predefined, a computational model of the supporting structure can be constructed for the purposes of a topology optimization procedure. Such optimization procedure, for example, is the problem for the optimal topology of the longitudinal load-bearing structure (the spar structural topology) under the objective of maximum stiffness and minimum mass. The proposed UAV's fixed wing design model is composed of stiffened skin panels with smeared stringers, solid ribs and continuous isotropic infill in the spaces between the ribs and the skin. The

leading and trailing edges of the wing have been removed in order to reduce the level of discretization of the finite element model. For the same reason, the skin is modeled with uniform thickness by smearing the areas of the supporting stringers. At later stages of the detailed wing design the stringers are modeled explicitly with beam type finite elements. For the purpose of finite element analysis the skin is discretized with shell type finite elements while the ribs and the isotropic infill - with tetrahedral or hexahedral finite elements. The required level of discretization of the finite element model for achieving numerical validation of the obtained results is determined according to the procedure described in [3]. The boundary conditions for the fixed wing model are defined by fixing the nodes at the root of the wing and distributing the aerodynamic load for the particular flight load case according to an approximate law [8, 9, 14].

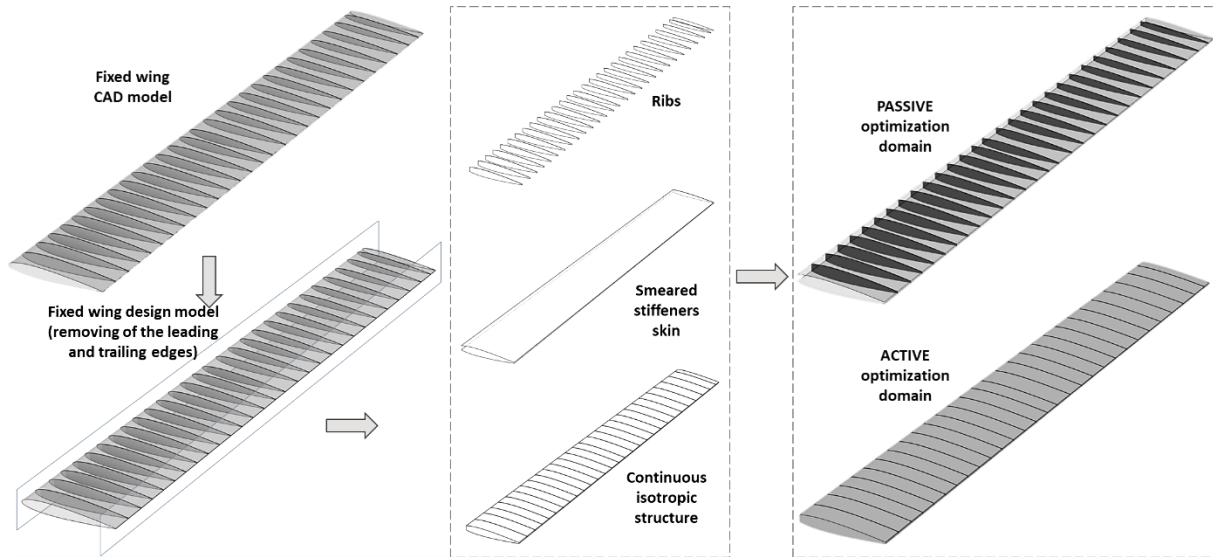


Figure 4. Sequence of operations on the synthesis of a computational design model for topology optimization of a fixed wing

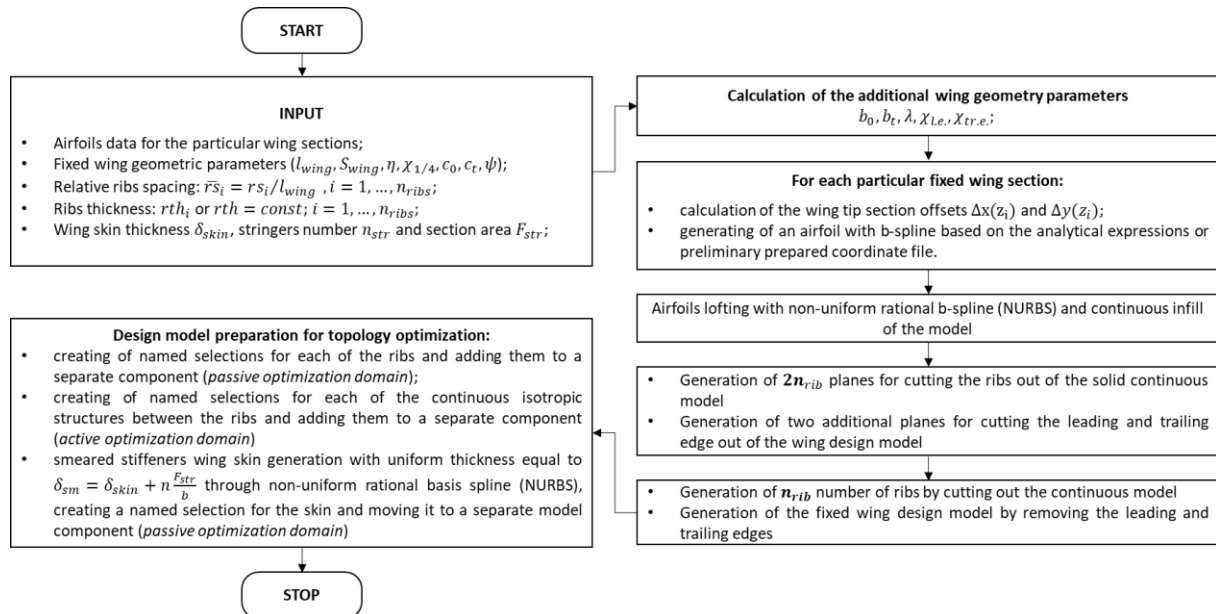


Figure 5. Flowchart of a numerical procedure for generation of a computational design model for topology optimization of a fixed wing

3. Topology optimization of a UAV fixed-wing design model

The displacements along the elemental nodes degrees of freedom are traditionally obtained as a result of preliminary finite element analysis of the discretized design model. The nodal displacements field represents an essential input data component for the topology optimization procedure. In turn the topology optimization provides an optimal distribution of the structural material in the active optimization domains of the model. The procedure is performed according to the SIMP method with penalization coefficient $p=3$ and an objective for minimum compliance of the final topology. To perform structural optimization by mass, a comparative study of the topologies obtained as a result of a parametric optimization procedure is required with variation of the relative volume f_0 of the structure.

Figure 6 shows the results from the topology optimization of the longitudinal load-bearing structure for the fixed wing of a medium altitude long endurance UAV (MALE UAV).

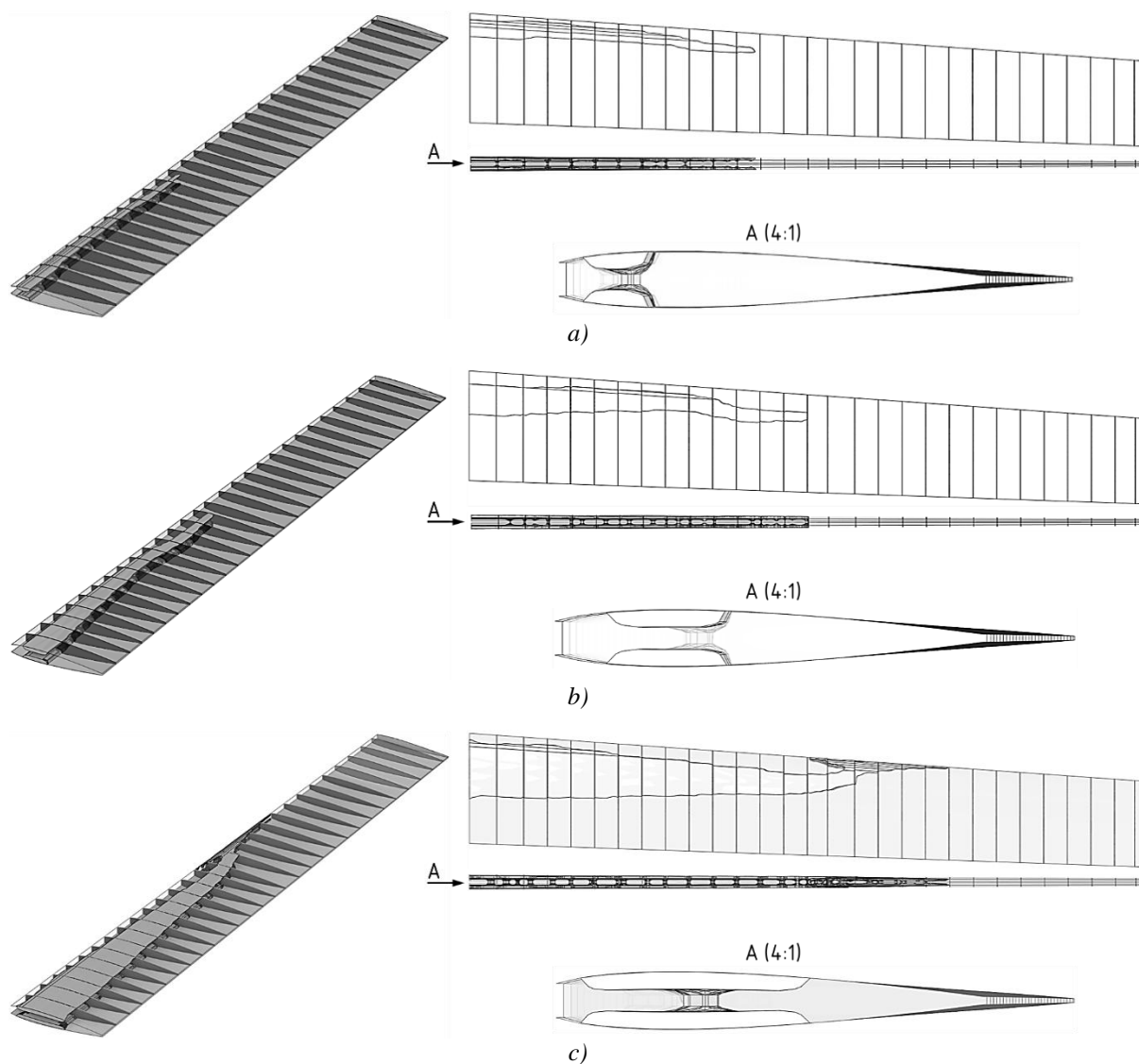


Figure 6. Optimal topology of the longitudinal load-bearing structure of a fixed wing with predefined configuration of the supporting members at relative volume:

a) $f_0=0.05$; b) $f_0=0.1$; c) $f_0=0.2$

It is important to clarify that the configuration of the supporting stiffeners (ribs and stringers) is predefined. The computational design model generation procedure is implemented using the Python programming language as an automated geometry building script for the graphical editor of a computer-aided design (CAD) system [17]. The topology optimization problem is solved for different values of the relative volume f_0 . Each of the obtained results is characterized by the presence of a single

longitudinal load-bearing structure resembling an I-beam with pronounced flanges and a web located in the zone of the applied aerodynamic load. The physical accuracy of the final optimal topology arises as a result of the proper definition of the synthesized design model.

The results from the finite element analysis of the topologically optimized wing reveal a uniform distribution of both the nodal displacements and the equivalent and normal stress (Fig. 7). The predefined configuration of the supporting members provides a minimum buckling load factor $\lambda_{min}=15.2$ for the intended safety factor of 1.5 and for the flight phase with the maximum operational load factor n_{max}^e according to the V-n diagram of the MALE UAV.

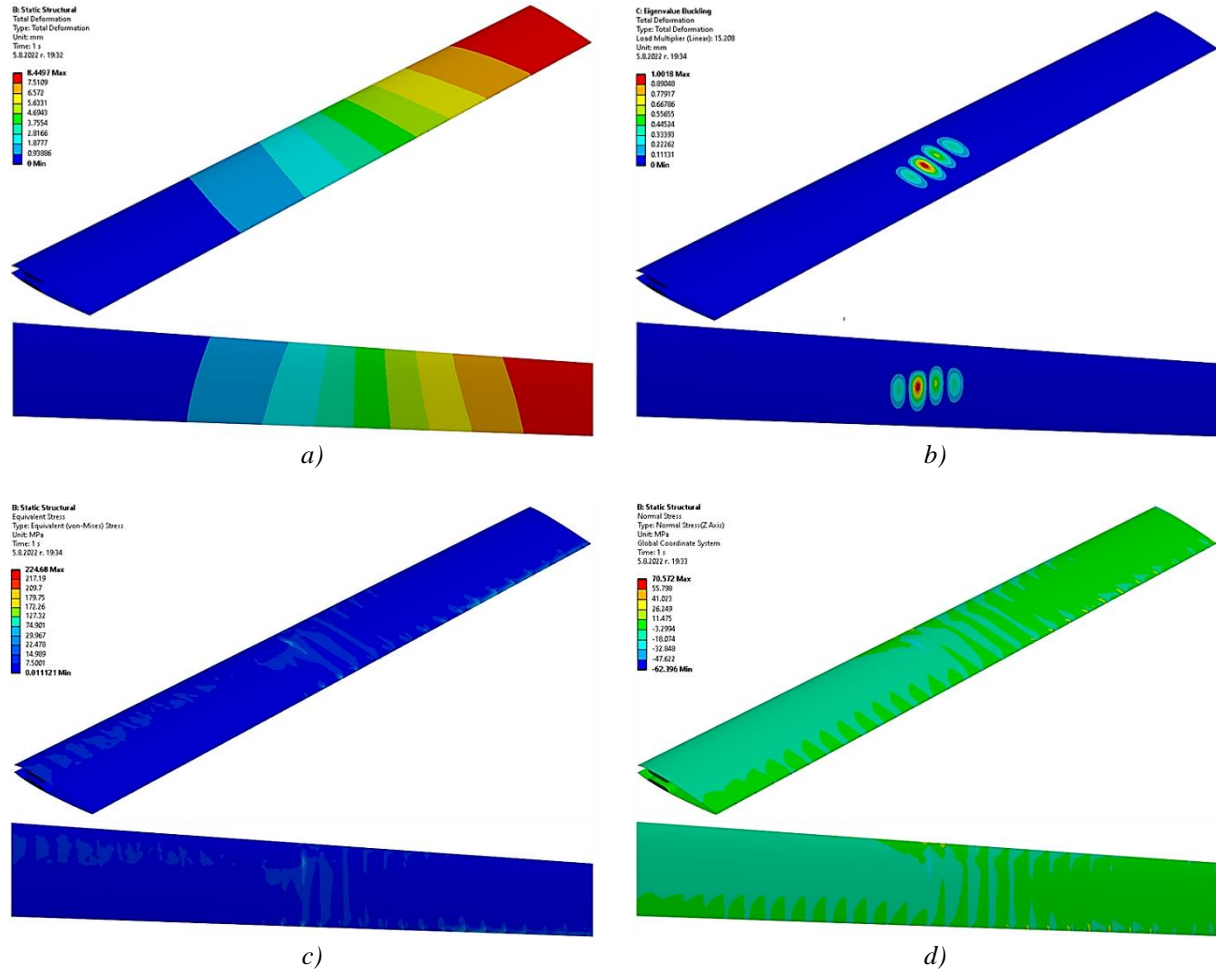


Figure 7. Results from the finite element analysis of the topology optimized fixed wing design model with relative volume $f_0=0.1$: a) nodal displacements distribution at the maximum load flight case; b) nodal displacements at critical buckling load with load factor $\lambda_{min}=15.2$; c) von Mises stress distribution; d) normal stress σ_z distribution.

4. Conclusion

In this work, a numerical procedure is proposed for generation of a computational design model of a UAV's fixed-wing for implementation in topology optimization problems. The state-of-art approaches for reducing the take-off mass of the UAV are presented as well as the most common approach for structural topology optimization in the context of the optimal design of thin-walled aircraft structures. A topology optimization problem is defined with objective for maximum stiffness of the computational design model discretized in finite elements with elemental stiffness approximated according to their relative densities.

The special features that must be taken into account when generating a computational model for topology optimization are identified. The most common approaches for parametrization of airfoils in the context of the fixed wing model generation are presented. A numerical procedure for the synthesis

of a computational design model for topology optimization of a fixed wing is proposed. The procedure is demonstrated by solving a topology optimization problem for the optimal design of the longitudinal load-bearing structure for the fixed wing of a MALE UAV under the objective of maximum structural stiffness. The obtained results prove the accuracy of the proposed design model.

The computational models generated according to the presented numerical procedure provide opportunities for:

- implementation of static structural, fluid, modal, etc. preliminary finite element analyses taking into account the specific operating conditions of the object;
- optimal design of a rational (practically optimal) load-bearing structure under the objectives of maximum stiffness and minimum mass using each of the currently developed topology optimization algorithms;
- accounting for an additional optimality criteria in the topology optimization problem, for example, for maximum stability against buckling, for minimum deflection of the supported panels, etc.
- accounting for various manufacturing constraints in the topology optimization problem, for example, related to the subtractive or additive manufacturing technologies;
- adding of passive optimization domains, defining cavities and compartments with special purpose, for example, fuel compartments, landing gear bays, equipment spaces, etc.

References

1. Aage N., E. Andreassen et al. Giga-voxel computational morphogenesis for structural design. *Nature*. 2017, Vol. 550, Issue: 7174, pp. 84-86, ISSN: 1476-4687. Retrieved from: doi:10.1038/nature23911.
2. Abbott I., A. Von Doenhoff. *Theory of wing sections: including a summary of airfoil data*. Dover Books on Aeronautical Engineering. 1959, Dover Publications, ISBN: 978-0486605869
3. ASME, *An Illustration of the Concepts of Verification and Validation in Computational Solid Mechanics*. ASME V&V 10.1-2012. 2012, New York, The American Society of Mechanical Engineers, ISBN: 9780791834152.
4. Bendsøe M. Optimal shape design as a material distribution problem. *Structural Optimization*. 1989, Vol. 1, Issue: 4, pp. 193-202, ISSN: 0934-4373. Retrieved from: doi: 10.1007/BF01650949.
5. Bendsoe M., O. Sigmund. *Topology optimization: theory, methods, and applications*. 2004, Heidelberg, Springer, ISBN: 9783662050866
6. Deaton J., R. Grandhi. A survey of structural and multidisciplinary continuum topology optimization: post 2000. *Structural and Multidisciplinary Optimization*. 2014, Vol. 49, Issue: 1, pp. 1-38, ISSN: 1615-1488. Retrieved from: doi: 10.1007/s00158-013-0956-z.
7. Georgiev Y. Battery energy storage technology for aviation - An overview. 2022, *Aeronautical Research and Development*, Vol. 1, Issue:1, pp. 36-42, ISSN 2815-2948.
8. Gundlach J. *Designing unmanned aircraft systems: a comprehensive approach*. 2012, American Institute of Aeronautics and Astronautics, ISBN (print): 978-1-60086-843-6
9. Keane A., A. Sóbester, J. Scanlan. *Small unmanned fixed-wing aircraft design: a practical approach*. Aerospace Series. 2017, John Wiley & Sons, ISBN: 978-1-119-40629-7.
10. Krog L., A. Tucker et al. Topology Optimization of Aircraft Wing Box Ribs. *Proceedings of 10th AIAA/ISSMO Multidisciplinary Analysis and Optimization Conference*: Albany, New York. 2004, American Institute of Aeronautics and Astronautics, ISBN: 978-1-62410-019-2
11. Kulfan B. Universal parametric geometry representation method. *Journal of aircraft*, 2008, Vol. 45, Issue: 1, pp. 142-158, ISSN: 1533-3868. Retrieved from: <https://doi.org/10.2514/1.29958>
12. Kulfan B., J. Bussoletti. Fundamental Parametric Geometry Representations for Aircraft Component Shapes. *Proceedings of 11th AIAA/ISSMO Multidisciplinary Analysis and Optimization conference*: Portsmouth, Virginia. 2006, American Institute of Aeronautics and Astronautics, ISBN: 978-1-62410-020-8. Retrieved from: <https://doi.org/10.2514/6.2006-6948>
13. Liu J., A. Gaynor et al. Current and future trends in topology optimization for additive manufacturing. *Structural and Multidisciplinary Optimization*. 2018, Vol. 57, Issue: 6, pp. 2457-2483, ISSN: 1615-1488. Retrieved from: doi: 10.1007/s00158-018-1994-3
14. Raymer D. *Aircraft design: a conceptual approach*. AIAA Education Series. 2018, American Institute of Aeronautics and Astronautics, Sixth edition, ISBN: 978-1624104909
15. Sóbester A., A. Forrester. *Aircraft aerodynamic design: geometry and optimization*. 2014, John Wiley & Sons, ISBN: 9780470662571
16. Sobieczky H. *Parametric Airfoils and Wings*. *Notes on Numerical Fluid Mechanics*. 1998, Vol. 68, pages 71–88, ISBN: 978-3-322-89952-1. Retrieved from: https://doi.org/10.1007/978-3-322-89952-1_4

- 17.SpaceClaim Developers Guide: API V22 Beta. 2022, ANSYS Inc.
- 18.Walker D., D. Liu. Topology optimization of an aircraft wing. Proceedings of 56th AIAA/ASCE/AHS/ASC Structures, Structural Dynamics, and Materials Conference: Kissimmee, Florida. 2015, ISBN: 978-1-62410-342-1. Retrieved from: <https://doi.org/10.2514/6.2015-0976>
- 19.Wang X., S. Zhang et al. Aeroelastic Topology Optimization of Wing Structure Based on Moving Boundary Meshfree Method. 2022, Symmetry, Vol. 14, Issue: 6, p. 1154. Retrieved from: <https://doi.org/10.3390/sym14061154>
- 20.Zhu J., W. Zhang, L. Xia. Topology optimization in aircraft and aerospace structures design. Archives of Computational Methods in Engineering. 2015, Vol. 23, Issue: 4, pp. 595-622, ISSN:1886-1784. Retrieved from:doi:10.1007/s11831-015-9151-2.
- 21.Badyagin A., S. Eger, V. Mishin i dr. Proektirovanie samoletov. 1972, Moskva, Mashinostroenie.

Analysis of possibilities for applicability of different types of unmanned aerial vehicles in the crisis management process - the signs and criteria for classifying of crises

Radoslav Chalakov, Stefan Biliderov

Rakovski National Defence College, Faculty "Command Staff", Sofia, Bulgaria, r.chalakov@rndc.bg
Air Force academy, "Aviation Faculty", Dolna Mitropolia, Bulgaria, biliderow_ss@yahoo.com,

Abstract: Uncertainty, unpredictability, dynamics and scope of crisis manifestations require the creation of a flexible national crisis management system. Emphasis is placed on prevention and early warning. Platforms built with unmanned aerial vehicles (UAV) are modern technical means and are particularly flexible and applicable to a wide range of activities, including crisis management. The same platform with minimal costs is retooled to perform radically different tasks. Their likely uses change depending on the specific task being solved at the moment, and unmanned platforms (UP) themselves are applicable for operating in both small and a sufficiently large areas.

Keywords: Unmanned aerial vehicles (UAV), Unmanned aerial platforms (UP), crisis management

Introduction to the problem

The skill and ability to manage crises is one of the main approaches to guaranteeing national security and international stability. The modern understanding of this process implies that the response to them should be carried out in an organized manner with mutual cooperation between the institutions and the competent authorities with appropriate use of national resources. All this needs to be organized in a unified national crisis management system [1].

The application of unmanned aerial vehicles (UAV) in security and defense has been increasing in recent years. They can identify security and defense challenges and identify vulnerable areas that are susceptible to various risks/crises. UAV are the modern tools that can improve crisis management capabilities. Traditional developments of unmanned systems (US) include the following areas of use:

- provision of information – information provision;
- supervision and observation – monitoring;
- intelligence;
- radio electronic warfare;
- communication links and retransmission of signals;
- detection and high-precision hitting of targets.

On the basis of the described capabilities, the main tasks of the UAV are also determined to achieve the requested goals in the interest of national security and defense. Such can be:

- reconnaissance tasks: reconnaissance of land, sea and air targets; reconnaissance of the area; airborne radiation and chemical reconnaissance; meteorological intelligence; radio and radio engineering intelligence; search and tracking of small mobile objects, etc.;
- strike tasks: hitting land and sea mobile targets; combating air targets, etc.;
- special tasks for combat support: radio-electronic warfare; fire control; adjusting artillery fire; relaying messages and data; transport tasks; aerial targets for training; security and surveillance of land and sea borders; search, locate and identify people and crews of means of transport suffering water shortage in a mountain-forest or desert area; combating the illegal trafficking of people, drugs and weapons, etc.

In addition to the applications of UAV listed here and the tasks related to them, an additional one is outlined in the following areas of application of Unmanned aerial platforms (UP):

- medical supply to people or animals in distress;
- border patrol with the ability to recognize risky situations and areas;

- control of maritime vessels for human trafficking and prohibited cargo;
- securing a large number of people in a crowd - tracking for signs of terrorist activity;
- finding and rescuing people in distress and those who have fallen into a difficult situation;
- environmental monitoring for the purpose of prevention.

The analysis carried out in this way makes it clear that the UAV is the tool that is able to provide the opportunity to solve a wide range of tasks with many nuances in the setting and with a constant readiness for a change in the situation. Expedient decisions and actions during crises in a given organization largely depend on the preliminary preparation of the system, the built structures, elements and functional connections. For this purpose, the types of crises and their signs will be analyzed.

Crises - types of crises

Regardless of the complex nature of the crises and their phenomenal essence, comprehensiveness and scope, there are conditional classifications of the crises themselves according to certain signs and criteria:

- the causes and nature of the controversies;
- manifestation in the sphere of public life;
- the manner of occurrence and their duration;
- the relevance of the crisis to the affected organization;
- the specifics of the military-political crisis;
- the social structure in which the parameters of the crisis are manifested;
- scope criterion;
- duration of action;
- institutional competence to implement the general coordination of forces and means in managing crisis situations.

The regulatory documents are also classified according to **9 (nine)** signs and criteria for defining crises. Where, depending on the causes and nature of the contradictions, crises can be reduced to **5 (five)** main types:

- military-political crisis – a state of the international relations of the countries, in which there is an immediate threat of the use of military force against the sovereignty, territorial integrity and independence of a given state;
- internal political crisis – a social phenomenon threatening the vital interests of the individual, society, stability and security of the state;
- as a result of terrorist actions and acts - surprising and unexpected, with great destruction, usually with many victims among civilians;
- humanitarian crises – caused as a result of natural disasters, industrial accidents, catastrophes, fires and others;
- diplomatic crises - when problems arise with citizens abroad or problems between states.

If the presented classifications are based on the sphere of public life in which the crises occur, a total of **9 (nine)** types of crises can be arranged:

- Military;
- Technological;
- Informational;
- Financial;
- Economical;
- Political;
- Social;
- Ecological;
- Cultural, etc.

Considering them depending on the way of occurrence and their duration, **3 (three)** types of crises can be distinguished:

- Sudden crises – they are caused by unexpected events and situations, in which the warning stage of the crisis process is negligibly small (strong or catastrophic earthquakes, large and complex fires, large floods, industrial accidents, catastrophes, terrorist acts);

➤ Crises occurring after a warning period – they can be predicted (ethnic conflicts; refugee flows; need for humanitarian assistance to large groups of people; cultural breakdowns; economic, social and religious problems; environmental catastrophes; viruses; computer terrorism; dissatisfaction of employees, low morale, sexual violence in the workplace, misuse of property, misuse of information, etc.);

➤ Periodically recurring – manifest themselves permanently despite all efforts (related to the change of "generations").

The classification criterion can be the relevance of the crisis to the affected organization and can be presented as **2 (two)** types manifested on this basis:

- internal to the social system;
- external to the social system.

Given the specifics of the military-political crisis, characterized by comprehensiveness, consumption of huge resources and caused in order to achieve strategic goals, the crises are divided into **2 (two)** types of manifestations on this basis:

- military character;
- non-military nature – earthquakes; floods and landslides; fires and drought; strong winds and tornado; heavy snowfalls, blizzards, icing and avalanches; extreme temperatures; hail; thunderstorms and lightning; chemical, radiation and biological risks; Global Warming; resource depletion, vessel accidents, road, rail and aviation accidents and unexploded ordnance, as well as terrorist acts and mass influx of persons seeking temporary protection into the country and other factors.

Depending on the social structure in which the parameters of the crisis are manifested, **5 (five)** types of manifestations can be defined on this basis:

- Municipal;
- Regional;
- National;
- Regional;
- International.

Given a criterion that is tied to the scope of the crisis itself, can be determined **5 (five)** types:

- Individual;
- Corporate or institutional;
- Branches;
- Local;
- Comprehensive.

According to the duration of the crises, they are divided into **3 (three)** types:

- Short term;
- Medium term;
- Continuous.

According to the criterion of institutional competence to implement the general coordination of forces and means in managing crisis situations, **4 (four)** levels of intervention can be defined:

- Actions to control crisis situations that arise as a result of disasters, accidents and catastrophes on the territory of a municipality;
- Actions to control crisis situations arising as a result of natural disasters, accidents and road transport accidents occurring on the territory of a region;
- In cases where the crisis develops on the territory of two or more areas, the interaction and coordination of the forces and means involved in managing the crisis is expedient;
- In cases where the crisis develops on the territory of the country.

From the analysis of the types of crises made in this way, 9 (nine) criteria by signs can be determined. The corresponding number of manifestations is indicated for each sign. Table 1 shows the signs and criteria for classifying crises (first row), and the second row shows the number of types of manifestations for each sign.

Table 1: Manifestations of crises

Criterion/Symptom (k)	1	2	3	4	5	6	7	8	9
Number of Manifestations (B)	5	9	3	2	2	5	5	3	4

Accordingly, the general population represents the set $n = \sum_1^n B = 38$, which means that $n = 38$ possible manifestations of the crisis. The sample size $k = 9$ criteria and signs of crisis classification. Then, each return unordered sample of volume k from the population of volume n represents the combination:

$$(1) \quad C_n^k = \frac{n!}{k!(n-k)!} = 163011640$$

or it is the number of different combinations of the manifestations of the crises under the listed criteria and signs in **table 1**.

An important condition for success in crisis management is its universality. So as to ensure an adequate response to all possible types of crises - military-political, foreign-political, internal-political, crises resulting from natural disasters and accidents resulting from human activity and others. Unforeseen consequences during a crisis change can be avoided by studying all the signs and their number of manifestations presented in formula 1.

Conclusion

The situation in the world continues to be complex, diverse, dynamic and unpredictable. Technological, ecological and demographic changes are taking place with unprecedented human consequences, previously unknown realities and alternatives are emerging, and **crisis** has become one of the most used words today, uttered by people with anxiety and uncertainty about the future

In order to successfully overcome crises, all people in the given structure must be familiar with the ways to overcome them. Every crisis, regardless of its nature, is characterized by time, opportunity for growth, element of surprise and corresponding signs. For this purpose, this article analyzes the types of crises and their signs. The combination of signs and classification criteria, as well as the corresponding number of manifestations attributed to each of the crises, was also calculated, which in turn provides opportunities for wider research. In the next article "Analysis of the possibilities for the applicability of different types of BLS in the crisis management process - building a functional framework for the application of different BLS" the framework for functional modeling of the decision-making process for the application of a specific BLS in an emerging crisis will be presented.

The research in this publication was carried out in fulfillment of Task 3.1.9. "Construction of a network of autonomous low-powered flying devices (quadcopters) for control of an urbanized area" by the National Scientific Program "Security and Defense", adopted by RMS No. 731 of 21.10.2021. and according to Agreement No. D01-74/19.05.2022.

Literature

1. Bakhchevanov, G., M. Manev, R. Ruseva. Crisis and conflict management. - Sofia: Softtrade , 2005
2. Crisis Management Law
3. Law on the management and functioning of the national security protection system